Leveraging Spatial Patterning for Optical Sensing

by

Elizabeth Strong

S.B., Harvard College, 2015
S.M., Massachusetts Institute of Technology, 2017

A thesis submitted to the
Faculty of the Graduate School of the
University of Colorado in partial fulfillment
of the requirements for the degree of
Doctor of Philosophy
Department of Mechanical Engineering
2022

Committee Members:
Gregory B. Rieker, Chair
Juliet T. Gopinath
Michael P. Brenner
Stephen Becker
Svenja Knappe
Peter E. Hamlington

Strong, Elizabeth (Ph.D., Mechanical Engineering)

Leveraging Spatial Patterning for Optical Sensing

Thesis directed by Prof. Gregory B. Rieker

The essence of active optical sensors can be distilled into three modules: the illumination, the system under study, and the detection. Just as constraints or requirements on one of these components can impose limitations on what can be sensed, enhancements to any of these modules can facilitate measurements which were previously challenging or impossible. In this thesis, we investigate how spatial patterns can be leveraged at each of the modules of an active optical sensor to simplify experiments and enable new measurements. We present three projects that enhance optical sensing capabilities via spatial patterning at one of the modules.

Each project corresponds to a chapter in this thesis. The first project patterns the illumination to develop a velocimeter for the study of fluid mechanics. Drawing from mature technologies which infer velocities from particle transits through linear interference fringes, we extend the capabilities of velocimeters by altering the shapes of the interference fringes and developing a supporting signal processing framework. We demonstrate the approach to perform direct angular velocity measurements. This approach represents an interesting new direction for fluid flow velocimetry which can be extended to sense other flow parameters by selecting different light structures.

The second project patterns the system under study. We present a strategy for aligning a beam of light to the axis of rotation of a spinning surface by patterning the surface and monitoring the scattered light as the surface rotates. This technique is simple and inexpensive, and can be implemented by adhering a strip of tape to the surface to achieve alignment accurate to within the uncertainty of the benchmark measurement, ±2.9% of the beam waist, limited by the size of the optical components used in the experiments.

The third project focuses on patterning the detection system. Working at the nexus of dual frequency comb spectroscopy and compressive sensing, we merge the capabilities of these tools

to perform the first hyperspectral dual-comb imaging. Programmable transmission masks imprint patterns on the light just before detection. Multiple measurements, each conducted with a different transmission mask, provide a means to reconstruct information encoded across the transverse extent of the beam.

For each project, complex alternatives exist to measure similar quantities. For example, the angular velocities of fluids can be deduced from linear velocity fields, alignment to spinning disks can be ensured by mounting diffraction gratings to their surfaces and studying the light diffracted from them, and hyperspectral images can be generated by scanning a dual-comb laser beam. Yet, we find that careful consideration of how information can be encoded in spatial patterns can not only readily yield these quantities of interest, but may do so more effectively than introducing more complicated experimental techniques.

Acknowledgements

Thank you to my family for your support through my PhD. Thank you to my mom, Laura, for always anticipating when I needed to meet up for dinner, and for letting me live with you for more than a year. Thank you to my dad, Lew, for asking me to ride or ski or climb with you every single day you weren't working, and for teaching me how to study and learn. Mom and Dad, I am for ever grateful for all the sacrifices you have made for me throughout my entire life. Thank you to my sister, Anne, for being my constant cheerleader and my closest friend. Thank you to my late partner, Mark Herzog, for encouraging me to leave Boston to start at the University of Colorado Boulder (CU), for modeling a life devoted to serving those who needed it the most, and for supporting me through some of the harder times of my PhD. It fills me with joy remembering the huge smile you always had while I'd tell you about the research I was excited about.

Thank you to my advisor Greg Rieker for mentoring me and never losing confidence in my work, even when I had. Thank you for giving me the time and space to process hard life events, and for helping me return to a more normal life when things started looking up. Thank you to Juliet Gopinath for letting me set up my experiments in your lab and for your constant encouragement. Thank you to Michael Brenner for your pep talks ever since you mentored me as an undergraduate student. And thank you for suggesting I move to Colorado. Leaving Boston to start at CU was one of the best decisions of my life.

Thank you to Alex Anderson for bringing me up to speed on working in an optics lab and for always being keen to talk about experiments. I was very lucky to learn from you and to work with you. Thank you to Emily Caldwell for helping me through optics classes and being the best office mate of all times. I will always cherish memories of the days which would start with a long morning chat, continue with lunch together, and end with dinner at your house. Thank you to Sean Coburn for helping me learn how to use the frequency combs, and for supporting me in the lab even while you and your family were en route to a Thanksgiving week away from home. Thank you to my lab mates for making the Precision Laser Diagnostic Laboratory an exciting and enjoyable place to work, and for letting me bring my dog to work every day.

Thank you to my Boston climbing partners and my Boulder biking buddies for keeping me outside on the weekends and on more week days than my advisor may have been aware of.

Thank you to my previous mentors Katia Bertoldi and Pedro Reis for sharing your enthusiasm and curiosity with me, for giving me the opportunities to work in your research groups, and for teaching me how to be a scientist.

Contents

Chapter

Appendix

Figures

Figure

Chapter 1

Introduction

When I started my PhD at the University of Colorado, my initial project was developing a noninvasive optical probe for fluid mechanics which would sense vorticity. The idea was that changes in the orbital angular momentum (OAM) of light scattered by small particles embedded in the flow could be directly related to vorticity of the flow. Measurements using Laguerre-Gauss (LG) beams had been demonstrated using two detection strategies [1, 2], and we wanted to build on these technologies to make direct vorticity measurements in turbulent systems and to bring such a sensor to practical application.

In particular, we were motivated to measure vorticity at small length and time scales in the hopes of learning about the unknown physical mechanisms which underpin energy transfer in turbulent flows. Unearthing such physical mechanisms has been of long interest. For nearly 100 years, we have known that a universal and self-similar energy transfer occurs between large and subsequently smaller sub-inertial length scales before energy is dissipated as heat [3]. Yet, visualizations of this process at fast enough time scales to observe this energy cascade are nascent [4].

Our objective was to make a sensor which could measure vorticity at these length small scales and short time scales to begin to develop an intuition for how this process occurs. In addition to our fundamental interest in studying turbulence, we were also interested in studying vorticity at these scales from an engineering perspective, since such measurements would enable experiment-based efficiency optimization for combustion systems. As we discuss in Appendix C, we learned that, while measuring vorticity using a strategy following Refs. [1, 2] would not be possible in generalized cases, we could measure angular velocities with this strategy. In particular, we came to understand that our patterned illumination sensor could be interpreted as an extension of laser Doppler velocimetry (LDV), a standard technique in experimental fluid mechanics labs. Yet, modifications and enhancements to the patterned illumination would result in a wide range of expected signals and therefore require a signal processing strategy different from that used in LDV. We developed a new signal processing means for the task which we anticipate is capable of predicting more than just components of the velocity vector. We expect that this new framework has the potential to measure other quantities such as flow rate. This signal processing strategy underpins the velocimeter which we developed and is the subject of Chap. 2.

This line of inquiry yielded several different projects seeking to understand the applications and limitations of the rotational Doppler effect (RDE). Because we expected that the RDE would be at the heart of our vorticity sensor, we needed to determine how to detect the RDE, using the fringe scheme of Ref. [1] or the heterodyne scheme of Ref. [2]. This work led to a second-author paper which compares the two possible detection schemes, finding that the heterodyne scheme is more appropriate for the class of measurement we would make in our vorticity sensor [5]. In another second-author paper, we found that the RDE can be measured using spatially incoherent light [6].

One key challenge we discovered while studying the fundamentals of the RDE was that the RDE is extremely sensitive to misalignment. Therefore, to claim that an effect arises due to the RDE, alignment between the rotor and the incident beam must be independently characterized. While alignment strategies had been previously discussed in the literature in the context of manufacturing, they involved mounting potentially bulky optical components to the spinning surface which could cause strain and induce vibrations. In Chap. 3, we present our alternative alignment strategy that functions by patterning the system under study, the rotating surface. By partitioning the reflectivity of the surface by adhering a strip of tape to it, we show that we can achieve alignment accurate to within the uncertainty of the benchmark measurement, ±2.9%. Using our technique, the inaccuracies associated with the benchmark measurement are eliminated. Also, since the detection scheme measures variations in intensity or power instead of imaging interference fringes, its use can be extended to incoherent light. Finally, and perhaps most importantly to the experimentalist, this strategy can be used in real time. Relative to other techniques proposed in the literature, we see the advantage of our technique to be its simplicity.

Having contributed an angular velocity sensor to the fluid mechanics community and several advances in our understanding of the RDE to the optical engineering community, my interest in turbulent flows remained. While characterizing flow kinematics is certainly a viable strategy for learning about turbulent flows, other quantities such as pressure, temperature, chemical species, and chemical concentration can also serve as proxy. The final contribution of this thesis is a hyperspectral imaging modality based on dual frequency comb spectroscopy and compressive sensing for capturing spatially resolved gas phase thermodynamic information. A single pixel camera architecture patterns the detection of this sensor, and thermodynamic quantities are recovered from the acquired broadband molecular absorption spectra via a smashed filter. We anticipate this will find application in studying turbulent flows by providing a means for characterizing parameters which are notoriously challenging to measure such as temperature gradients at flame edges. This sensor is the subject of Chap. 4.

In this thesis, we develop active optical sensors for fluid flow velocimetry, alignment of an optical beam to a rotating surface, and hyperspectral imaging. These projects leverage spatial patterning at the three modules of an active optical sensor, the illumination, the system under study, and the detection, respectively. Though the ultimate applications of each of these sensors are quite different, they are unified by the theme which runs throughout this thesis: Patterning modules of an active optical sensor can facilitate measurements which were previously tenuous or impossible, for patterning imparts structure through which observations can be understood.

The sensors we develop in this thesis each address different applications and draw from a variety of fields. Therefore, we have structured this thesis such that the beginnings of Chapters 2, 3, and 4 include the relevant introductory remarks specific to the respective sensor. We conclude in Chapter 5 by revisiting the central argument of this thesis, that tailoring the spatial patterning of an optical sensor can augment its capabilities and simplify its operation.

Chapter 2

Velocimetry

2.1 Introduction

Experimental techniques are critical for studying fluid flows, especially if the flows cannot be studied numerically due to physical restrictions or computational limitations. As such, velocity sensors are a primary class of diagnostic tool. Velocity sensors typically measure linear components of the velocity vector. Yet, many flows have important angular velocity components. In turbulent flows, for example, regions with elevated local angular velocities give rise to and mediate the most salient characteristics of the flow, including how and where energy is dissipated.

Traditionally, the mismatch between that which can be sensed (linear velocities) and that which is of interest (angular velocities) has been addressed by deriving the latter from the former. For example, metrics such as vorticity and circulation which characterize the local rotation of flows are calculated by numerically differentiating measured multi-component linear velocity fields. However, such strategies come at the cost of resolution, as the numerical differentiation inherently introduces spatial uncertainty. While increasing the density of the field samples can increase the spatial resolution, increasing the number of samples comes the cost of reduced temporal resolution. Thus, if a high degree of temporal resolution is required, poor spatial resolution may result. To refine the spatial and temporal resolutions of measurements which quantify rotation, we seek to

---

This chapter is adapted from E. F. Strong, et al. “Angular velocimetry for fluid flows: an optical sensor using structured light and machine learning,” Ref. [7]

measure a component of the angular velocity field without needing to first measure components of the linear velocity fields. This direct strategy will facilitate measurements with both short temporal and small spatial resolutions, positioning the measurements well for studying flows which change rapidly in both time and space.

Our sensor uses a strategy common in fluid velocity sensing: seeding the flow with small particles which scatter light. Assuming the particles are sized properly so they travel faithfully with the flow [8], their velocities are assumed to match the velocity of the flow around them. When these particles pass through an optical probe beam, the light they scatter is imaged or collected on a photodetector. Information regarding the size, surface properties, and kinematics of the reflector as well as characteristics of the probe beam such as its intensity are encoded in the scattered signal and can be extracted using appropriate signal processing techniques. Examples of existing techniques which calculate linear components of flow velocities from the light scattered by seeded particles include field sensors like particle image velocimetry (PIV) and point sensors like laser Doppler velocimetry (LDV). Other techniques, such as spatial filtering velocimetry, imprint temporal periodicity into the scattered light signal using spatially periodic masks [9], gratings [10], or optical fiber arrays [11]. These and related flow visualization techniques have been developed extensively, and are commonly used in research and development settings in contexts ranging from flume experiments to study coral reefs [12, 13] to blood flow [14] to combustion systems [15, 16].

In this chapter, we build on these earlier approaches that probe the fluid with structured light (light with engineered phase, polarization, and intensity profiles). In particular, we take advantage of structured light that is tailored to match particular properties we wish to measure (e.g. a radially symmetric pattern to measure angular velocity [17]), while allowing for resulting scattered light signals to be complicated with no simple relationship to the flow property (e.g. wavelength shift to velocity in LDV). In order to ascertain a correlation between these expected signals and the angular velocity, we train a modern machine learning regression model to interpret the signals. We demonstrate this approach by measuring angular velocity using the interference of two conjugate beams with orbital angular momentum (OAM). To the best of our knowledge, this is the first time that structured light and machine learning have been used together in a velocimetry application.

Our angular velocity sensor is closely related to LDV. The behavior of both our sensor and LDV can be described in the spatial domain. Interference fringes (intensity modulations) generated by superimposing two coherent beams of light comprise the probe beam. Particles traveling through these fringes scatter light proportionally to the local intensity. In one configuration of LDV [18], interfering plane waves give rise to sinusoidal fringes. As depicted in Fig. 2.1a and Fig. 2.1b, the distance between fringes multiplied by the frequency at which the scattered light is modulated yields the component of the velocity orthogonal to the fringes.

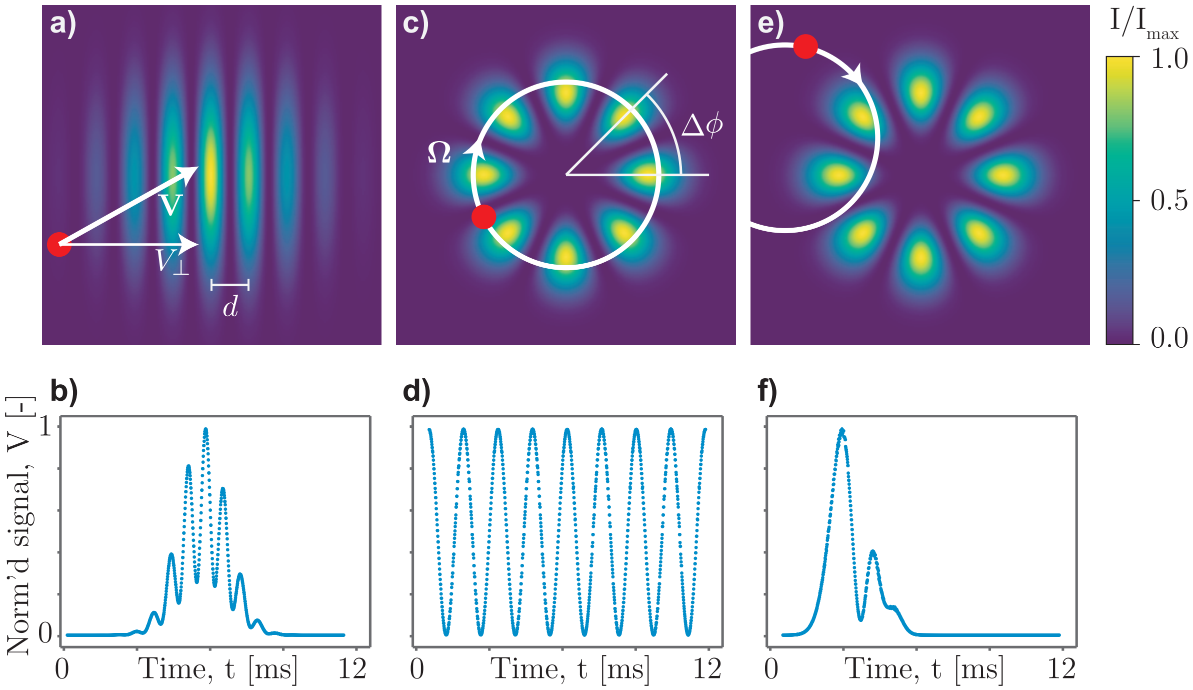

Figure 2.1: The light scattered by a particle traveling through interference fringes is encoded with information regarding the particle's kinematics. a, c, f) Simulated schematics of scattering particles (red dots, radii r) traveling on trajectories (indicated with the bold white line) which pass through spatially varying intensity fields created by a) interfering two plane waves with a relative angle of 5.73° or c, f) interfering conjugate Laguerre Gauss beams with $l = \pm 4$ and $p = 0$ modes. b, d, f) resulting normalized scattered light signals as a function of time. a, b) the fringe spacing d divided by the period of the normalized signal V yields the component of the velocity vector of the particle in the direction perpendicular to the interference fringes, $V_\perp$. c, d) the fringe spacing $\Delta\phi$ divided by the period of the normalized signal V yields the component of the velocity vector of the particle in the angular direction, Ω. e, f) if the particle orbit and the light are not concentric, interpreting the resulting normalized signal is not straightforward and requires an alternative approach.

Modifications to the structure of the probe beam can yield alternative interference patterns which can be used to sense different properties of the flow. For example, the fan-like fringes created by interfering light with cylindrical wavefronts can be used to infer velocity gradients close to a wall [19, 20, 21]. Likewise, radial interference fringes can be used to measure angular velocities [17, 1, 22, 23]. As shown in Fig. 2.1c and Fig. 2.1d, the angular velocity of a particle traveling on a circular trajectory concentric with radial interference fringes can be determined from the product of the radial fringe spacing and the intensity modulation frequency, $\Omega = \Delta\phi \times f_{mod}$ [1, 23]. In most fluid flows, however, particle orbits are not concentric with the probe beams, and orbit radii may be larger than the size of the beam. What results is a signal processing challenge: no one-to-one relationship between the angular velocity and the expected signal necessarily exists (compare the signals in Fig. 2.1d and Fig. 2.1f which correspond to the same angular velocity). These more complex scenarios therefore require an alternative strategy for signal analysis. The sensor concept that we develop in this chapter accommodates complicated signals with a machine learning-based signal processing scheme.

Previous direct attempts to measure rotation in fluids fall into two classes: scattering of unpatterned light by specially engineered particles [24], and scattering of patterned or structured light by the same particles used for PIV and LDV [2, 1]. In the first class, the vorticity (a measure of the local angular velocity) of small spherical particles with embedded planar mirrors are measured with a spatial grating system [24]. The spatial and temporal resolutions of this strategy are small (μm) and fast (ms). However, the environments in which measurements of this type can be conducted are limited, as matching the optical and physical properties of the seeding particles to those of the flow is required but can only be accomplished in specific cases. Moreover, fabricating the seeding particles is quite involved.

In the class of direct rotation sensors which illuminate readily available small particles with structured light, one approach calculates the fluid circulation by statistically analyzing the frequency shifts present in the scattered light when particles traverse a ring-shaped Laguerre-Gauss (LG) beam [2]. LG beams have phases which vary azimuthally as $\exp{(il\phi)}$, where i is the imaginary number, l is the azimuthal mode number, and ϕ is the azimuthal angle about the beam axis. LG beams also have radial modes indexed with p; here, all LG beams have $p = 0$. These beams possess $l\hbar$ of OAM. Because changes in phase give rise to changes in frequency, particles passing through such beams scatter frequency shifted light. The system of Ref. [2] was demonstrated using a flow field simulated on a digital micromirror device (DMD), and was found to estimate the vorticity with a spatial resolution of 0.1 cm. However, the statistical signal processing technique requires many particle transits through the probe beam, and this limits the temporal resolution of the sensor. In the simulations from Ref. [2], for example, the transits of 250 particles were assembled for each measurement. The experiments from Ref. [2] were conducted in a highly controlled environment that allowed for frequency shifts to be measured via optical heterodyne, interfering the scattered light with a reference beam on the photodetector. In such a configuration, the probe and reference beam travel separately to the photodetector, with the probe beam traveling through the fluid and the reference beam bypassing the fluid. Consequently, the beams experience different environments could induce phase noise and beam steering, complicating detection in actual fluid applications.

An alternative approach for characterizing fluid rotation by measuring vorticity also uses LG beams to probe a seeded flow, but bypasses the challenges associated with the detection scheme of Ref. [2] by combining the signal and the reference beams before they enter the flow [1]. As such, optical modes remain overlapped and maintain their mutual coherence, even if features of the environment distort the wavefronts. The resulting beam has a petal-shaped interference pattern with $2l$ lobes. As the angular analog to LDV, this technique relates the frequencies of the intensity modulated scattered light to the angular spacing of the petal fringes to determine the angular velocities of the particles. The working principle of this sensor is illustrated in Fig. 2.1c and Fig. 2.1d. However, two assumptions limit the applicability of this technique to more general flows. The first limiting assumption is that the particle orbits are concentric with the beam axis. This restricts where in the flow the sensor can function and makes the sensor sensitive to misalignment between the beam and rotating structures in the flow. The second limiting assumption is that the fluid moves obeying solid body rotation. The sensor always predicts the vorticity of the flow to be twice the angular velocity, even if the vorticity has contributions due to shear, meaning the flow behavior does not consist fully of the solid body rotation mode.

The sensor we present in this chapter builds on the above approach, adding a more complex signal processing scheme in order to remove the limitations on which flow configurations it can be used with. As before, this is an Eulerian sensor, meaning that it remains fixed in the lab frame and it monitors the flow as it passes by. In our approach, we measure the angular velocity instead of the vorticity because in general cases, the Biot-Savart Law indicates that the velocities in a flow are due in part to contributions from both local and nonlocal vorticities [25] (See more on angular velocity versus vorticity measurements in Appendix C). We measure the angular velocity of a single particle embedded in a 2-dimensional flow (no velocity components in the direction of the probe beam) as it travels on a curved pathline and passes through a probe beam. Specifically, we model the pathline of each particle to be a circular arc, and we predict the particle's steady state angular velocity Ω along that arc. Approximating particle trajectories as curved can be justified by noting that many other flow velocimetry techniques assume particles travel only in straight lines. As in LDV, we sense this motion using a probe beam with interference fringes whose geometries are well characterized, and like the sensor of Ref. [1], these interference fringes are formed by conjugate LG beams having azimuthal modes $\pm l$. Also like these sensors, we make no assumptions about the viscosity of the fluid. As we will explain below, while both LDV and Ref. [1] use frequency domain signal processing strategies, such an approach is not appropriate for the expected signals from this technique. The signal processing strategy which accompanies our angular velocity sensor requires characterizing each burst in the return signal resulting from the light scattered as a particle transits the probe beam and extracting a set of metrics with which we predict Ω. These predictions are conducted with a supervised machine learning regression model which is trained using experimentally validated simulated data. We expect that this sensor will function at short time scales defined by the duration of the particle transit as well as at short length scales set by the relative sizes of the particle and the transverse intensity profile of the probe beam. We anticipate that this sensor will find applications in systems which can accommodate only one optical access port, where imaging techniques might not be possible, and where pathlines through probe beams cannot be approximated as linear.

The structure of the chapter is as follows. In Sec. 2.1.1, we provide a brief overview of orbital angular momentum (OAM), the class of structured light we use to demonstrate our angular velocity sensor. In Sec. 2.1.2, we discuss the frequency shifts one would expect to measure in the backscattered light from a particle illuminated with light with OAM. In Sec. 2.2 we formalize the sensor, presenting the mathematical model we implement to simulate expected experimental signals. Experimental validation of these simulated signals is described in Sec. 2.3. With the simulated signals experimentally validated, we consider signals collected via simulations and experiments as interchangeable, and therefore are able to more flexibly and efficiently formulate and evaluate the signal processing strategy associated with the sensor using simulated results. The signal processing technique is discussed in Sec. 2.4. First, we describe the signal conditioning steps of the technique in Sec. 2.4.1. Then, in Sec. 2.4.2, we present the machine learning regression model at the heart of the sensor that predicts the angular velocity and orbit radius of particles. The results are discussed in Sec. 2.5. Sensor limitations are outlined in Sec. 2.6, where we pay special attention to the parameters which set the resolution of the sensor. Finally, we close with a discussion in Sec. 2.7, where we explain strategies extending the capabilities of the sensor to more complex fluid flows.

2.1.1 Sensing rotation using structured light with Orbital Angular Momentum

In 1992, Allen and coworkers discovered that beams of light can possess orbital angular momentum (OAM) in unbounded quantized units of $l\hbar$ [26]. Though the existence of OAM had been theorized by Darwin [27] in the context of higher-order atomic/molecular transitions requiring the conservation of angular momentum in units of $\hbar$ greater than 1 (as limited by the spin angular momentum associated with circular polarization), observations of OAM were thought to be rare [28]. However, beams with azimuthal phase distributions according to $\exp(il\phi)$ are now understood to possess $l\hbar$ of OAM [26]. Such beams are commonly decomposed in the Laguerre Gauss (LG) basis since LG modes are solutions of the paraxial Helmholtz equation in cylindrical coordinates [29].

LG beams have helical wavefronts whose amplitudes are expressed as

$$E(r) \sim r^l \exp\left(-\frac{r^2}{w^2}\right) L_p^l\left(\frac{2r^2}{w^2}\right), \tag{2.1}$$

where r is the radial coordinate, l is the azimuthal mode number, w is the beam waist, p is the radial mode number L_p^l is the generalized Laguerre polynomial function [30]. Owing to the dependance of the amplitude on the radial coordinate, LG beams are circularly symmetric. The phases of LG beams are given by

$$\Phi(r, \phi, z) = kz - \frac{kr^2}{2R(z)} - l\phi - \psi(z) - \tan^{-1}\left(\frac{z}{z_0}\right)(l + 2p + 1), \tag{2.2}$$

where k is the wave number, R is the radius of curvature, ψ is the Gouy phase, and z_0 is the Rayleigh range [30]. When $l = p = 0$, the beam is Gaussian. When $l \neq 0$, these beams have p concentric ring-shaped intensities and helical phases. Due to the helical phase, the skew angle between the direction of propagation and the Poynting vector scales as $\beta = \sin^{-1}(l/kr)$ [31, 32].

The helical wavefronts of OAM beams endow them with a unique capability to sense the rotational Doppler shift (RDS). Doppler shifts can be equivalently understood as arising as a consequence of the conservation of momentum when photons and moving surfaces [29] or phonons [33]. The transfer of momentum corresponds to a frequency shift in the light according to

$$\Delta\omega = \Delta\vec{k} \cdot \vec{v}, \tag{2.3}$$

where $\vec{k}$ is the wave vector of the light and $\vec{v}$ is the relative velocity of the moving object and the observer. If the light has no OAM meaning that its momentum is entirely in the direction of the Poynting vector, Doppler frequency shifts are detected only if the directions of light propagation and object motion are not orthogonal. But in the case that the directions of light propagation and object motion are orthogonal *and* the light has OAM, a Doppler frequency shift can now be detected, since the Poynting vector has a component in the direction of the moving object [34, 35, 36, 37]. The physical phenomena underpinning this frequency shift are discussed in Sec. 2.1.2. Here, review several measurements of this frequency modulation, which we call the rotational Doppler effect (RDE).

To demonstrate the RDE, a host of experiments which we refer to as the class of rotating disk experiments have been conducted in which a structured illumination source is incident on a scattering surface rotating at a known frequency. Two detection strategies exist: fringe and heterodyne. These are illustrated in Fig. 2.2. In the fringe detection scheme (see Fig. 2.2a), two beams with different (typically conjugate) l are combined before they come in contact with the rotating surface. In the heterodyne detection scheme (see Fig. 2.2b), a probe beam consisting of a single l scatters from the rotating surface and is then mixed with a reference beam of a different (unshifted) l at the detector. As we discuss in Ref. [6], the heterodyne detection is sensitive to phase while the fringe detection scheme is not. A strategy for choosing one detection scheme other the other is considering the density of scattering centers; whereas the signal-to-noise ratio (SNR) of the heterodyne method increases proportionally to the number of scattering centers, the SNR of the fringe method is highest when only a single scattering center contributes to the signal [6]. Anecdotally, we have also found that experimental alignment constraints are eased when we use the fringe method instead of the heterodyne method, since the mutual coherence of the beams is preserved as the combined beams travel through the experiment, enduring phase aberrations and other disturbances simultaneously.

When the probe and the reference beams are conjugates meaning they have l of equal magnitude but opposite direction, the frequency modulations associated with the RDE occur at harmonics of

$$\Delta f = \frac{\alpha l \Omega}{2\pi}, \tag{2.4}$$

where α takes a value of 1 in the heterodyne scheme and 2 in the fringe scheme, the illuminating beam has OAM of $l\hbar$, and Ω is the rotational frequency of the disk. Rotating disk experiments typically plot $\Delta f(\Omega|_l)$ and $\Delta f(l|_\Omega)$.

Commonly, the rotating disk experiments use an optical chopper as the scattering surface since Ω is easily controlled and typically independently measured. The first demonstration of the RDE in this class of experiments performed by Lavery and coworkers showed that such mea-

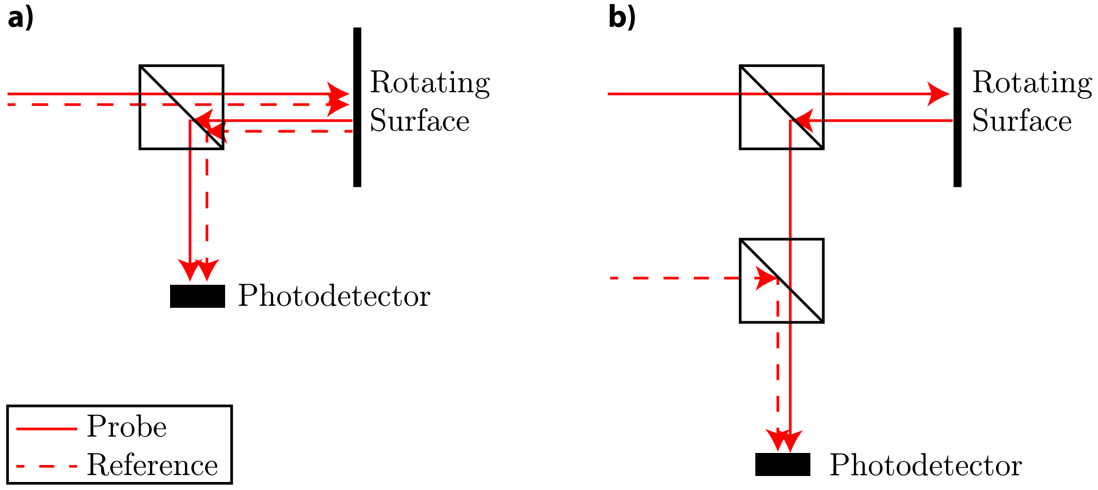

Figure 2.2: Measurement schemes for the rotational Doppler effect. a) Fringe mode. Conjugate $\pm l$ beams are combined before they scatter from the rotating surface. b) Heterodyne mode. A probe beam with OAM mode l $(-l)$ scatters from the rotating surface. The scattered light is then combined with the reference beam with OAM mode $-l$ (l)

surements were possible [22]. Subsequent work has shown that the RDE can be observed with temporally incoherent light [38] as well as with spatially incoherent light [6] (I contributed to this spatially incoherent light paper as second author). Extensions of this RDE work have investigated its sensitivity to alignment, finding that a broadened signal results but in some cases can still be interpreted [39]. Others have shown that the RDE can be measured in concert with the longitudinal (canonical) Doppler shift, showing promise for measuring helical motion [40]. If the angular velocity of a rotator can be measured, changes in the angular velocity over time estimate the angular acceleration. Ref. [41] uses short-time-Fourier transforms to generate spectograms which characterize this change in angular velocity as a function of time to measure angular velocities. The RDE can also be measured using a low density of photons [42], an encouraging finding for long range remote detection applications.

Though much work has been done studying the RDE in the context of scattering light from a monolithic rotating surface, probably because such experiments are readily built and easily controlled, the rotating object needs not be a disk. In Ref. [23], LG beams are used to measure the angular velocities of microparticles in spinning in an optical trap. The RDE has also been observed spectroscopically in the work of Ref. [43], where the Doppler line broadening of rubidium atoms was found to increase with increasing l, matching theoretical predictions closely. The rates of rotation of various optical components including cylindrical lenses [44] and rotating dove prisms [45] have also been measured from the RDE. Particularly intriguing in the context of this chapter are the other fluid velocimetry applications, such as those from Refs. [1, 2], described above in Sec. 2.1.

While the LG modes serve as a convenient basis for characterizing OAM beams, the measured OAM is only $l\hbar$ if the detector is perpendicular to the beam and centered along the axis of propagation [46]. This is because the OAM in a beam depends on the axis about which it is measured [47, 48]. The implication is that if experiments require measuring the OAM of the light, alignment is critical. In Chapter 3 of thesis, we contribute a strategy for aligning beams to the axis of rotation using a strategy which does not depend on the spatially dependent OAM spectrum of the incident beam.

Beams with OAM have been of great interest in optical communications applications because of the possibility of mode division multiplexing (MDM): encoding information on each of the unbounded and mutually orthogonal l modes [49]. In contrast to other forms of multiplexing using wavelength-division or polarization-division, the amount of information which can be simultaneously transmitted is theoretically unbounded since l is unbounded. MDM using beams with OAM has been demonstrated both in free space [50, 51] and in fiber [52]. Yet, many challenges remain before MDM using beams with OAM can become widespread. In particular, because OAM modes cannot be readily transmitted through inexpensive fiber, they propagate through free space [49]. One of the challenges associated with these modes traveling through free space is crosstalk due to atmospheric turbulence which leads to variations in the refractive index along the transverse extent of the beam [53, 54].

OAM beams can be generated in many ways which fall into two classes: shaping the laser cavity to support and emit OAM modes [55, 56], or shaping an emitted Gaussian mode into an OAM mode outside of the laser cavity. Outside of the laser cavity, Gaussian modes can be converted to OAM modes using a wide variety of optical elements, with q-plates [57], diffractive phase holograms [58, 59] displayed as computer generated holograms (CGHs) on DMDs [60] or LCOS-SLMs [61], and spiral phase plates [62] being the most common. In this thesis, we use the strategies presented in Ref. [61] to display CGHs on LCOS-SLMs.

2.1.2 Frequency shifts

The classical (non-relativistic) Doppler shift occurs when the apparent frequency of the wave to a detector differs from the emanated frequency from an emitter due to relative motion between the emitter and the detector. For example, light scattered back towards its source by a particle moving with velocity $\vec{v}$ has a Doppler shift given by $\Delta f = 2\vec{k} \cdot \vec{v}$, where $\vec{k}$ is the wave vector of the light ($|\vec{k}| = \frac{2\pi}{\lambda}$) [63]. This frequency shift depends on the angle between the velocity and the scattered light direction; only motion in the direction of the detector contributes to the frequency shift.

However, this concept of a Doppler frequency shift can be generalized to allow for frequency shifts due to motion in the plane transverse to the detector by considering that the mechanism which gives rise to the frequency shift is the linkage between phase and frequency, namely that changes in phase give rise to changes in frequency [64]:

$$\Delta f = \frac{1}{2\pi}\frac{\partial \Phi}{\partial t}. \tag{2.5}$$

Consider a backscattered beam whose phase depends on the longitudinal z coordinate as $\Phi(z) = -2kz$. For this beam, $\Delta f = \partial\Phi/\partial t = -2k\partial z/\partial t = -2kv_z$, where v_z is the component of $\vec{v}$ in the direction of the detector. This is consistent with the standard interpretation of the Doppler shift discussed above.

Now if we consider a backscattered beam whose phase depends not only on the longitudinal coordinate z but also on the coordinates of the plane transverse to the beam (r, ϕ), the expression in Eq. 2.5 may also have some dependence on these transverse coordinates. This contribution to the frequency shift from the transverse phase can be written as [64]

$$\Delta f_{\perp} = \frac{1}{2\pi}\nabla_{\perp}\Phi \cdot \vec{v}_{\perp}, \tag{2.6}$$

where $\nabla_\perp \Phi \cdot \vec{v}_\perp$ represents the transverse gradient of the projection of the phase onto the transverse velocity. For example, the frequency shift of a beam with a phase $\Phi(r, z) = 2kz + l\phi$ is given by $\Delta f = 2kv_z + 1/(2\pi) l \nabla_\perp \phi \cdot \vec{v}_\perp = l\hat{\phi}/r \cdot \vec{v}_\perp$. Since the angular velocity $\Omega = v_\perp/r$, $\Delta f = 2kv_z + l\Omega/(2\pi)$.

2.2 Sensor overview and simulations

In the case of LDV, the velocity component orthogonal to the interference fringes is given simply by the product of the distance d [L] between the fringes and the frequency at which the intensity of the scattered light varies [T^{-1}] (Fig. 2.1a, b). In the case of angular velocity sensing with conjugate LG beams, the distance from the LDV argument is replaced with the angular spacing $\Delta\phi$ [rad] [1] (Fig. 2.1c, d). However, if misalignment between the probe beam and the particle axis of rotation exists, as depicted in Fig. 2.1e, the particle no longer traverses interference fringes spaced equally in angle, and the resulting time series no longer possesses a single temporal frequency that can be used in such an analysis. In fact, as shown in Fig. 2.3, particles can travel on orbits with the same radius and at the same angular velocity but yield very different time series if these orbits are centered at even slightly different locations. Thus, a more sophisticated signal processing scheme is required to predict the angular velocity Ω of the particle under the many possible combinations of orbit radii, centers of rotation, and angular velocities.

To train and validate our machine learning regression model for predicting the angular velocity and orbit radius of scattering particles traversing our probe beam, we numerically simulate the expected backscattered light that forms our data. In these simulations, we artificially sample an intensity petal pattern formed by interfering two LG beams with azimuthal modes $l = \pm 4$, radial modes $p = 0$, and a beam waist $w(z)$ with a minimum of $w_0(z) = 93.84$ pixels on a 986×616 pixel grid. These values were set to match the experiment that we use to validate the simulated signals, which is discussed in Sec. 2.3. Positions on the grid are referenced to its center using a radial coordinate system, $(\mathcal{R}, \phi)$.

The expected signal is modeled to be proportional to the scattered light from a particle. For simplicity, we model the scattering particle as a mirror oriented towards the detector, assuming that

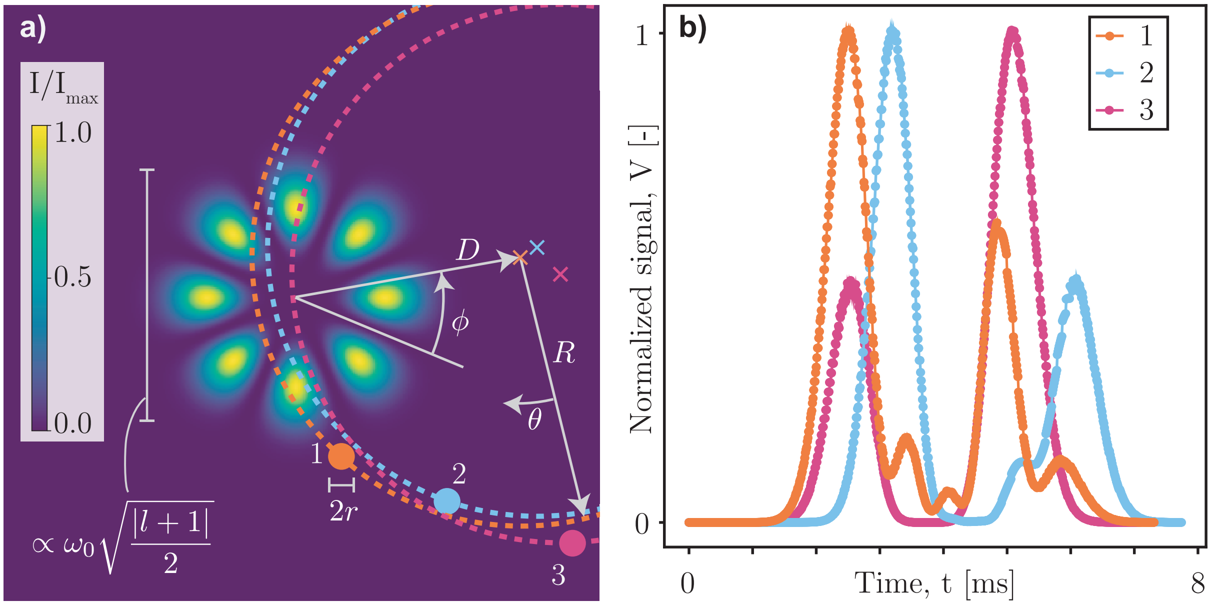

Figure 2.3: Particle transit parameter space. A particle radius r travels on an arc radius R (broken lines) at an angular velocity $\Omega = d\theta/dt$. This orbit is centered at position (D, ϕ) (orbit centers marked with crosses) relative to the center of the interference pattern (normalized beam intensity simulated in background). As the particle passes through the interference pattern, it scatters light proportional to the intensity of light within the area of the particle. The size of the interference pattern is set by the beam waist, w_0, and the azimuthal index of the light, l. Three particles are shown as orange, blue, and gray circles. Each particle travels on an orbit of the same R at the same Ω , but the positions (D, ϕ) of these trajectories are slightly different. b) simulated time series for the particles shown in a), each normalized by its maximum value. Although the particles can all be considered to obey the same physics, the resulting signals are dissimilar due to where they cross the interference pattern. This illustrates the fundamental problem this sensor addresses, that particles which travel obeying the same physics, but which are probed at slightly different positions yield time series may not resemble each other. Parameters for particles 1, 2, and 3): $w_0 = 93.84$ pixels, $l = \pm 4$, $r = 20$ pixels, $R = 400$ pixels, $D = [340.3,\ 367.7,\ 396.6]$ pixels, respectively, $\phi = [-0.178, -0.205,\ -0.88]$ rad, respectively, and $\Omega = 250$ rad/sec.

the particles have the same size, shape, and reflectivity so that the intensity of the light incident on the detector depends only on the intensity field at the particle location. Such assumptions are employed in the analogous technique of LDV [8] and are valid when the ratio of the spatial extent of the intensity pattern to the distance between the detector and the particle is small. Further, the simulated particles have identical radii of $r = 20$ pixels. Homogeneous seeding particles are readily available for fluid sensors due to advances in particle fabrication techniques [8]. In what follows, the size of the particle and the ratio r/w_0 remains unchanged and therefore is not necessarily optimized.

The simulated time series consists of signals from many particles passing through the petaled beam in series, with no more than one particle traversing the beam at a time. These passes are spaced in time to reflect a low density of seeding particles such that the time between transits is at least as long as half the average time of a transit. As we will see in the signal conditioning step described in Sec. 2.4.1, spacing of approximately this time or longer is necessary for identifying the salient features of the signals.

The relevant particle transit parameters to this problem are illustrated in Fig. 2.3a. We model the motion of each particle to have a constant angular velocity along a circular trajectory. The backscatter signal which results from a particle traversing the interference pattern is

$$\underbrace{V(t)}_{signal} \propto [\underbrace{g(\mathcal{R},\phi)}_{particle} * \underbrace{I(\mathcal{R},\phi)}_{intensity}] \times \underbrace{X(\mathcal{R},\phi,t)}_{trajectory} + \underbrace{n(t)}_{noise}, \tag{2.7}$$

where the particle is considered to be a perfect mirror using a *tophat* function $g(\mathcal{R},\phi)$ equal to 1 within radius r and 0 otherwise. The particle functions as the kernel of a round blurring function which operates on the calculated intensity field of the interference pattern, $I(\mathcal{R},\phi)$. The particle trajectory $X(\mathcal{R},\phi,t)$ is centered at (D,ϕ) relative to the beam center. The blurred intensity is sampled as a function of time t along the trajectory of the particle at a sample rate of 100 kHz. We add white noise to the time series to generate the expected detector signal V.

The parameter space consists of 7 variables, $\{w_0,\ l,\ r,\ R,\ \phi,\ D,\ \Omega\}$, and is illustrated in Fig. 2.3a. We reduce the dimensionality of the parameter space by fixing the characteristics of the light (w_0, l) as well as the particle radius (r). Additionally, we leverage the radial symmetry of the light to restrict ϕ, limiting the orbit center positions relative to the beam axis to angles $\pi/(2l) \le \phi < 3\pi/(2l)$. At each (D,ϕ), where D is the distance between the orbit center and the beam axis, the orbit radius R is limited to values that allow the particle to pass through the petals of the interference fringes. Noting that the beam width at full width half maximum intensity scales by $r_p \sim w_0 \left(\frac{|l+1|}{2}\right)^{1/2}$ [65], this limitation constrains R to $D - r_p - r < R < D + r_p + r$. Any particle radius r on an orbit with radius R centered at (D,ϕ) relative to the beam axis, then, will travel through the interference fringes.

In Fig. 2.3 we plot the simulated signals corresponding to three particles traveling on orbits with the same radii at the same angular velocities, but with slightly offset orbit centers. Though the particles in each of these simulations move according to the same physics, the resulting time series appear to have no similarities. These traces emphasize the signal processing challenge of this sensor, which is to create a model which relates a set of metrics from these dissimilar signals to predict the same Ω.

In this section, we have presented LDV in its fringe configuration, but we note that LDV can also be operated in a heterodyne configuration, wherein the flow is illuminated with only one beam (no interference fringes) [66]. In this alternative setup, particles in the flow backscatter Doppler shifted light which interferes with a second (local oscillator) beam on the detector, and the velocity of the particles is related to the measured frequency shift. Likewise, the rotation measurements we present here could also operate in this alternative heterodyne configuration in which the flow would be illuminated with a single LG beam and then the backscattered light would interfere with a conjugate LG (local oscillator) beam on the detector. While the fringe and heterodyne optical arrangements are mostly equivalent [67, 5], the fringe method that we detail in the chapter provides an increased tolerance to scattering, as phase aberrations do not affect the overlap of the beams. The fringe method also eases the alignment constraints in the detection system. In our experience working with LG beams in the lab, we have found that obtaining sufficient modal overlap can be challenging. Knowing that passing only one of the two beams through a fluid environment would probably aberrate its wavefront, we have opted to mimic the fringe strategy.

Because simulations provide a more controllable environment than experiments, we use the simulations detailed in this section to develop and evaluate our sensor. We proceed by first ensuring that the simulations capture the important experimental features by comparing them to experimental results. This validation process is described in the following section. The code for the simulations detailed in this section and the analysis which follows are publicly available [68].

2.3 Experimentally validating the backscattered light simulations

To experimentally validate our simulations, we conduct highly controlled experiments and compare the results to our simulations with a cross correlation. While we have designed our sensor to be used in fluid flows, the proof-of-concept experiments we present here follow the strategy of Ref. [2] and replaces the fluid system with a digital micromirror device (DMD). This gives us precise control of the dynamics of the 'flow' and allows consistent repetition of a particular condition. Ultimately, this allows us to verify that, up to the assumptions outlined in Sec. 2.2, our simulations match our experiments. In the first subsection below, we present our experiment and discuss the experimental data acquisition process. In the second subsection, we describe the experimental validation strategy which we use to justify replacing experiments with simulations in developing the sensor.

2.3.1 Experimental Setup

In Fig. 2.4a we present a schematic of our experiment. Using a HeNe (Thorlabs, HNL050LB) as our light source, we prepared a Laguerre-Gauss beam of light with $l = \pm 4$ using a liquid crystal on silica spatial light modulator (LCOS-SLM, Cambridge Correlators, SDE 1024). The LCOS-SLM was programmed to display a computer-generated hologram consisting of a forked grating and a mask that selects only the $\mathrm{LG}^{p=0}$ radial orders in each of the diffracted beams [61]. The first diffracted order was then isolated from the others with a spatial filter and directed towards a digital micromirror device (DMD, Texas Instruments, DLP4500). The DMD displayed a video of a small circle (radius 0.15 mm) traveling on a circular trajectory. These videos were designed so that no more than one particle passed through the light at a time. The video framerate was fixed at $f_{dmd} = 0.225$ Hz. The light sampled by this moving group of mirrors was collected on a photodetector (Thorlabs, Det36a). The resulting time series was low pass filtered (Mini-Circuits BLP-1.9+, 1.9 MHz cutoff frequency lumped LC low-pass filter) and then digitized with a data acquisition system (DAQ, National Instruments, USB6215) with a sampling rate of $f_s = 100$ kHz.

Though the cutoff frequency of the low pass filter was greater than half the sampling rate of the DAQ meaning that aliasing could have occurred, the dynamics of the experiment (0.225 Hz) were far slower than either the cutoff frequency (1.9 MHz) or the sampling rate (100 kHz), so this was not a concern, and any data that was aliased was interpreted as noise.

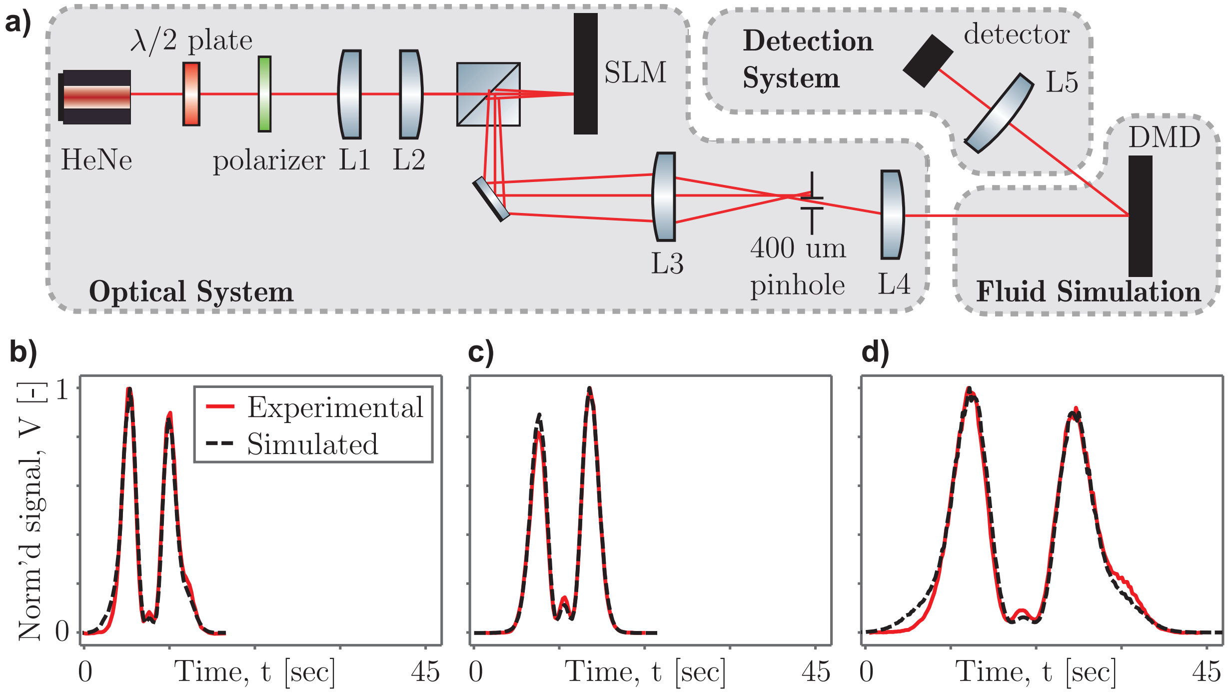

Figure 2.4: a) Experimental setup. The optical system prepares the probe beam to be directed to the fluid simulation module by converting the Gaussian laser beam from the HeNe laser to a superposition of conjugate $\pm l = 4$ Laguerre Gaussian beams. The fluid simulation is conducted on a digital micromirror device (DMD). Simulated scatterers reflect light to the detection system, which digitizes the intensity of the light impinging on a detector, yielding the signal we analyze. $\lambda/2$: half wave plate, L1-5: lenses, SLM: liquid crystal on silica spatial light modulator b-d) experimental (red solid lines) and simulated (black broken lines) normalized signals as a function of time. Parameters for simulations and experiments shown in b-d: $w_0 = 93.84$ pixels, $l = \pm 4$, $r = 20$ pixels, $R = 1200$ pixels, $D = [1250, 1265,\ 1250]$ pixels, respectively, $\phi = 0$ rad, and $\Omega = [654,\ 548,\ 223]$ rad/sec, respectively.

In principle, we could have run our experiments at a rate set by the ultimate speed of the DMD, 4225 Hz. However, because the objective of these experiments was to generate data with which to validate our simulations, we opted to operate at a fraction of this speed so that we could average the signal at each frame to improve its signal to noise ratio (SNR). Each video frame played for $f_{dmd}^{-1} = 4.44$ seconds, and the voltage corresponding to the intensity of the light impinging on the photodetector for that frame was calculated using the signal from the middle 4 seconds of data. Prior to averaging, we applied a numerical Butterworth filter (5th order, cutoff frequency 50 Hz) to the signal for smoothing. These steps increased the SNR by reducing the effects of noise arising from the influence of the multimodal nature of the laser as well as the noise induced by circuitry implemented to support the DAQ. The SNR, calculated as the ratio of the mean and the standard deviation of the numerically smoothed signals, was found to be, on average, 42.

We designed the DMD videos so that the averaged signal would correspond to the motion of a particle traveling on an arc with a specific angular velocity, sampled at f_s. The particle position was calculated such that it moved along its arc by an angular spacing $\Delta\phi = f_s/\Omega$. Because f_s was fixed, we varied the angular velocity of the experiments by changing the angular spacing between the frames.

2.3.2 Comparing signals from simulations and experiments

We conducted 47 experiments to validate our simulations varying D and Ω ($1150 \leq D$ [pixels, 10 values] ≤ 1305, and $223 \leq \Omega$ [rad/sec, 7 values] ≤ 655) while fixing the remaining parameters at the following values: $w_0 = 93.85$ pixels, $l = \pm 4$, $r = 20$ pixels, $R = 1200$ pixels, $\phi = 0.0 \pm 0.01$ rad. A description of our methodology for determining w_0 to match in the simulations and experiments is in Appendices D and E. Examples of the experimental results compared to their simulated counterparts are shown in Fig. 2.4b-d. To assess the similarity of the experimental and simulated signals, we calculated the maximum cross correlation, normalizing it by the autocorrelation of each of the signals at zero lag: $\max(\hat{R}_{xy}) = \max\left((R_{xx}R_{yy})^{-\frac{1}{2}} R_{xy}\right)$, where

$$R_{xy}(m) = \begin{cases} \sum_{n=0}^{N-m-1} x_{n+m} y_n^*, & m \geq 0 \\ R_{yx}^*(-m), & m < 0 \end{cases} \tag{2.8}$$

for $-\infty < n < \infty$, $m > 0$, N being the length of the longer signal x or y, and where * represents the complex conjugate. We find high correlations between the simulated and experimentally collected signals, with the mean and the standard deviations of the correlations of each of the 47 experiments with its corresponding simulation being 0.96 and 0.03, respectively.

As discussed above, our simulations were constructed with a discretization selected to match the pixilation of the DMD, with pixels in both cases being square having widths $s = 7.637\ \mu$m [69]. Projecting the radial pattern on the square grid created the possibility that the pixel orientations were rotated relative to each other, and this could have an influence on the calculated and measured intensities. However, because the particle is large relative to the pixels ($r/\ s = 20$) and blurs the intensities from every pixel within it, we found this effect to be negligible. As seen in Fig. 2.4b and Fig. 2.4d, the agreement between the simulation and the experiment appears to break down when the particle starts and finishes its transit through the light. We believe this is due to imperfections in our beam. The holograms displayed on the LCOS-SLM were generated assuming the incident beam was Gaussian in intensity, but a beam profiling system (WinCamD LCM, DataRay) indicated that a Gaussian fit to the intensity of the beam at its centroid by iteratively adjusting its height and width deviated in its integrated area from that of the beam by approximately 7%. Such deviations in the incident beam would propagate through the hologram and manifest as unexpected intensity variations in the LG beam. This could be related to the same features which led to the discrepancy between the experimental and simulated intensities shown in Fig. 2.4b and Fig. 2.4d. Noting that these discrepancies were small and anticipating such variations between experiment and simulations due to the complexities associated with directing light into a fluid, we decided that because the maximum cross correlation between the experimental and simulated signals was higher than a threshold we set of 0.90, that we would proceed with the sensor demonstration.

2.4 Signal Processing

The signal processing algorithm consists of two modules: signal conditioning and angular velocity prediction. The conditioning step begins by first identifying which portions of the signal contain information from a particle transiting the interference pattern. Only small portions of the signal which we call *bursts* contain information. These bursts correspond to the transit of a particle through the probe beam. In our signal processing scheme, we first isolate these bursts and then parameterize them by fitting with multiple Gaussian functions. The resulting parameters are used as the inputs for the machine learning (ML) model, which predicts the angular velocities and orbit radii of the trajectories of the particles. This ML model is pre-trained using data generated via the simulations described in Sec. 2.2.

In the present section, we outline the signal conditioning we apply to the all of the data, first discussing the details of the burst detection scheme and then moving on to describe multi-Gaussian fit step. We note that all data, be it experimental or simulated, for model development or evaluation, is processed identically following the steps outlined here. We close this section with a discussion of the architecture of the machine learning model.

2.4.1 Signal Conditioning

The time series data associated with these experiments is both intermittent and aperiodic because particles transit the beam unpredictably while the data acquisition system runs continuously. The challenge is to first determine which portions of the time series correspond to bursts, transits of scattering particles through the beam, and then to extract information from these bursts by parameterizing them.

2.4.1.1 Burst Detection

A particle passing through the interference fringes scatters light proportionally to the intensity of the light incident on the particle. When the particle is positioned within a null of the interference pattern, no light is scattered at all. Therefore, a burst may contain valleys of only noise between high intensity regions. Consequently, bursts cannot be detected directly with a zero-crossing algorithm, as this may errantly split a single burst into many. Instead, we smooth the signal by convolving it with a *rect* function whose width is greater than the expected duration of the longest null. We then use a crossing algorithm to determine when a burst starts and finishes by comparing this smoothed copy of the signal to a threshold set by the convolution of the *rect* with a portion of the signal which consists of only noise. To ensure we select the entirety of the burst without clipping any information, buffering regions which we call *tails* are added to the beginning and end of each burst. Though these tails contain little or no information about particle movements, they can have an influence on the burst parameterization. To prevent artifacts from the burst detection scheme in later stages of the analysis, the tail durations of each burst are selected at random within a range that keeps the tail small relative to the total burst duration.

2.4.1.2 Multi-Gaussian Fits

Once we identify the bursts, we parameterize them to summarize their dominant features for use as inputs to the machine learning (ML) model. In principle, the time series of the burst itself could be directly input to the ML model, but we found that this approach was highly sensitive to the length of the tails of the burst which contain little or no information. Therefore, we used a curve fitting scheme to parametrize and extract the features from the burst.

One parameterization strategy that is commonly used by optical sensors involves using a Fourier decomposition. However, such an approach proved futile here because the bursts have relatively little periodic behavior. Moreover, sinusoidal basis functions are continuous in time, whereas the bursts are discrete and localized in time. Due to the periodic nature of Fourier decompositions, such a parameterization would have a strong dependency on the length of the tails of the bursts. Therefore, we opted for an alternative parameterization technique which incorporated basis functions which trend to zero away from their maxima, more closely resemble the bursts, and deemphasize the lengths of the burst tails.

In this chapter, we parameterize the bursts with a sum of multiple Gaussian functions and a small vertical offset which allows for noise. Noting that a burst corresponding to a single pass of a particle through the interference pattern should contain no more peaks than petals in the interference pattern, we sum up to $2l$ (here, $2l = 8$) of these Gaussian functions as follows:

$$y = h + \sum_{n=1}^{2l} A_n \exp\left[\frac{(\mu_n - t)^2}{\sigma_n^2}\right]. \tag{2.9}$$

In this sum of Gaussian functions, A, μ, and σ are the amplitude, temporal offset, and width of the Gaussian functions, respectively, and h is a vertical offset. Examples of bursts fit in this way are shown in Fig. 2.5. We note that alternative orthogonal decompositions with compact support like wavelet transforms might also provide a means for this processing step.

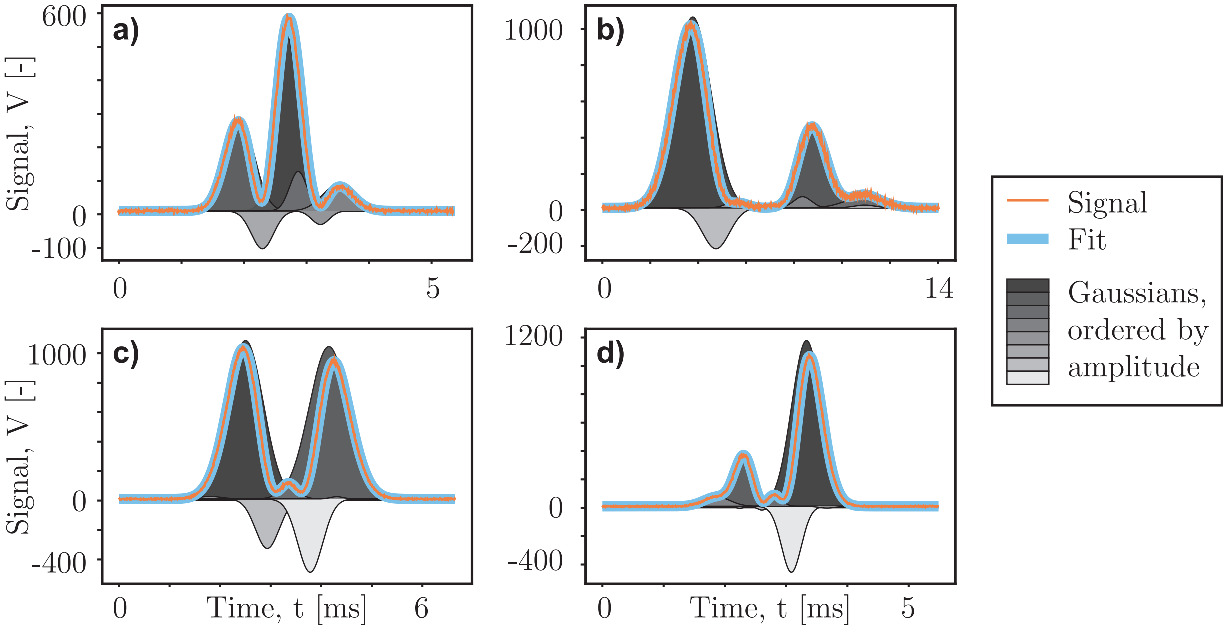

Figure 2.5: Bursts parameterized by fitting Eq 2.9 to them. Each of the fitted Gaussians is shaded with a color corresponding to its amplitude. Parameters for bursts in a, b, c, and d: $\Omega = 284.4,\ 100.4,\ 346.3,\ 268.5$ rad/sec, $R = 535.9,\ 435.9,\ 312.1,\ 608.2$ pixels, $D = 362.5,\ 391.0,\ 379.7,\ 670.9$ pixels, and $\phi = 0.64,\ 0.51,\ 0.76,\ 0.94$ rad. In all cases, $r = 20$ pixels and $l = \pm 4$.

Gaussian functions do not form an orthogonal basis, so a great deal of care was taken to ensure that the parameterizations converged to realistic and physical solutions. Curve fits were performed sequentially on each burst. The vertical offset was initialized as the noise level of the signal. Initially, a peak finding algorithm identified the number and locations of the local maxima of the burst. If there were fewer than $2l$ peaks, the first fit was conducted with Gaussian functions positioned at each maxima. These Gaussian functions each had an amplitude A equal to the difference of the burst value at that position and the noise level, and widths σ calculated to be 1/10 the rect effective width of the signal, calculated by numerically integrating the difference between the signal and the noise level, then dividing this quantity by the maximum amplitude of the difference between the signal and the noise level. Fits were weighted with smoothed copies of the bursts to emphasize the portions corresponding to the signal while simultaneously deemphasizing the tails. If the residuals between the resulting fit and the signal were greater than a threshold set by 110% of the noise level, a new fit was conducted, this time with a new Gaussian function at the position of the residual with the largest magnitude. As before, the previously placed Gaussian functions were located at the peak positions with parameters set by the peak at that location. The newest Gaussian function was now permitted to have a negative amplitude. We iterate this process until either the magnitude of the residuals was smaller than the noise floor, or until more than $2l$ Gaussian functions were necessary. Though in some cases the Gaussian functions were found to have significant overlap to characterize a single peak in the burst, we set the threshold to be equal to the number of petals in the interference pattern ($2l$, which is 8 here) based on the intuition that the signal would not have more peaks than petals. If more than 8 Gaussian functions were needed to parameterize the signal, or if the fits failed to converge at any step, the burst was eliminated. Approximately 80% of our bursts had fits which converged with 8 or fewer Gaussian functions in the parameterization. The remaining 20% of the bursts which appeared to have no common features with each other were discarded.

2.4.2 Predicting angular velocity and orbit radius with a machine learning model

A machine learning regression algorithm allows us to discern correlations between the angular velocities of the rotating particles and parameterizations of their resulting bursts. The machine learning model used in this chapter is built using APIs from the open source software libraries Keras [70] and TensorFlow [71]. The model is a sequential model with two densely connected layers which use the rectified linear unit (ReLU) nonlinearity and an output layer which returns two continuous values, Ω and R. The predictions of R have large uncertainties so we do not consider them to be a part of our sensor, but we include them in the quantities the model predicts because they improve the fidelity of predictions of Ω. As an input, the model takes the parameters of the bursts described above, as well as several additional parameters characterizing the duration of the burst and the quality of the fit. The amplitudes A_n of each burst are normalized to the largest A_n of the burst. This also serves to permit fluctuations in the intensity of the probe beam on time scales longer than the duration of the burst. In order to remove the influence of the tail length, the temporal offsets μ_n are referenced to the earliest μ_n parameterizing the burst. To ensure all parameters are equally represented in the model and to stabilize the training, each variable is independently scaled to approximately the same range ([0,100]) based on the minimum and maximum expected values based on the properties of the experiment and the flow. Identical normalizing factors were used in model training and evaluation. The model has 6,210 trainable parameters which are trained by minimizing the mean square error using the RMSprop optimizer. To avoid overfitting, the model is trained with an EarlyStopping [71] callback that halts the training when little improvement is seen in the validation error. Training data is also augmented by fitting up to three copies of each burst, each padded with tails of different length. In total, 83,885 parameterizations of 51,182 bursts are used to train the model. These bursts correspond to simulations conducted with the following parameters: $300 \leq D$ [pixels]≤ 700, $100 \leq R$ [pixels]≤ 920, $50 \leq \Omega$ [rad/sec]≤ 1040, $\pi/8 \leq \phi$ [rad]$\leq 3\pi/8$.

2.5 Results and Discussion

Once the machine learning model was trained, it was evaluated with a second set of parameterizations of 2,948 bursts selected independently and at random within the same parameter range as the train set. The results are shown in Fig. 2.6, where we plot the predicted angular velocity, Ω_P, as a function of the actual angular velocity, Ω_A. The results are binned into 25 angular velocity partitions of width 39.5 rad/sec.

This sensor has a dynamic range of $50 \leq \Omega_A$ [rad/sec] $\leq\approx 800$, wherein Ω_P scales linearly with Ω_A.The limit of linearity of the sensor beyond which this sensor no longer provides useful predictions of Ω_A is $\Omega_A \approx 800$ rad/sec. Though we found that the limit of linearity was always smaller than the ultimate angular velocity used to train the model, we were unable to attribute

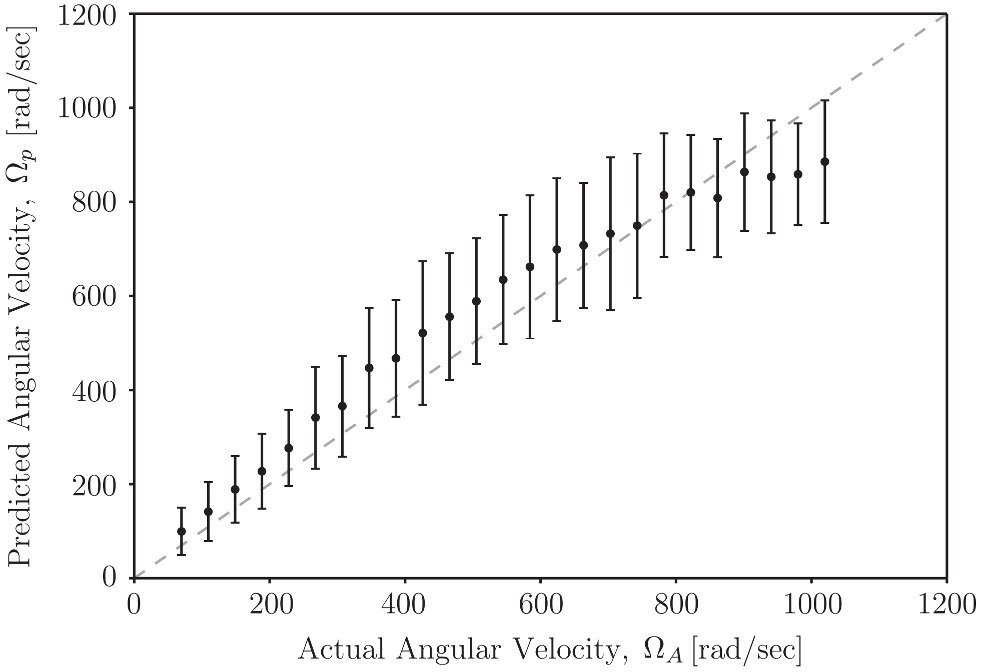

Figure 2.6: Predicted angular velocity as a function of actual angular velocity. 2,948 bursts with varying R, ϕ, D, and Ω sampled in the ranges described in the text are used to evaluate the machine learning model. The mean (closed circles) and standard deviation (uncertainty bars) of predicted angular velocities are plotted for each of the 25 partitions of width of 39.5 rad/sec of the sampled angular velocity range. Each partition contains predictions for more than 70 bursts.

this observation to physical characteristics underlying the simulations. Therefore, we recommend training the model with simulations which have angular velocities larger than those expected in the experiment.

Within the dynamic range of the sensor, the mean measured Ω_P is biased and systematically over predicts Ω_A; however, this effect could be calibrated by subtracting the average bias from the prediction since the model is evaluated with "known" simulated reference standards. In this demonstration, we forgo such a calibration step in an effort to emphasize the ML component of the signal processing algorithm. After such a calibration step, the resulting predictions would still retain the dispersion shown in Fig. 2.6 but with no bias. We define the measurement uncertainty as the standard deviation of the angular velocity predictions within each angular velocity prediction since this dispersion relates directly to the quality of the measurement. As indicated with uncertainty bars in Fig. 2.6, the measurement uncertainty is a function of Ω_A, but is no more than 162 rad/sec for $\Omega_A \leq 800$ rad/sec. The uncertainties are, on average, ±14% for each burst.

We expect that the uncertainty discussed above has two dominant sources, (1) the geometry of the sensor, and (2) burst parameterizations. In the first case, the radial symmetry of the probe beam and the circular trajectories of the scattering particles can conspire to generate very similar bursts with multiple parameter combinations. An example of this situation is illustrated in Fig. 2.7, where the simulated trajectories of particles with different orbit centers, orbit radii, and angular velocities are shown to yield almost identical bursts. Given the parameterization of one such burst, the model may ascribe an incorrect angular velocity to the burst is not uniquely generated by one set of values of the underlying parameters. The other dominant source of uncertainty arises as a consequence of the non-orthogonal basis functions used to fit the burst: many parameterizations of the same burst exist.

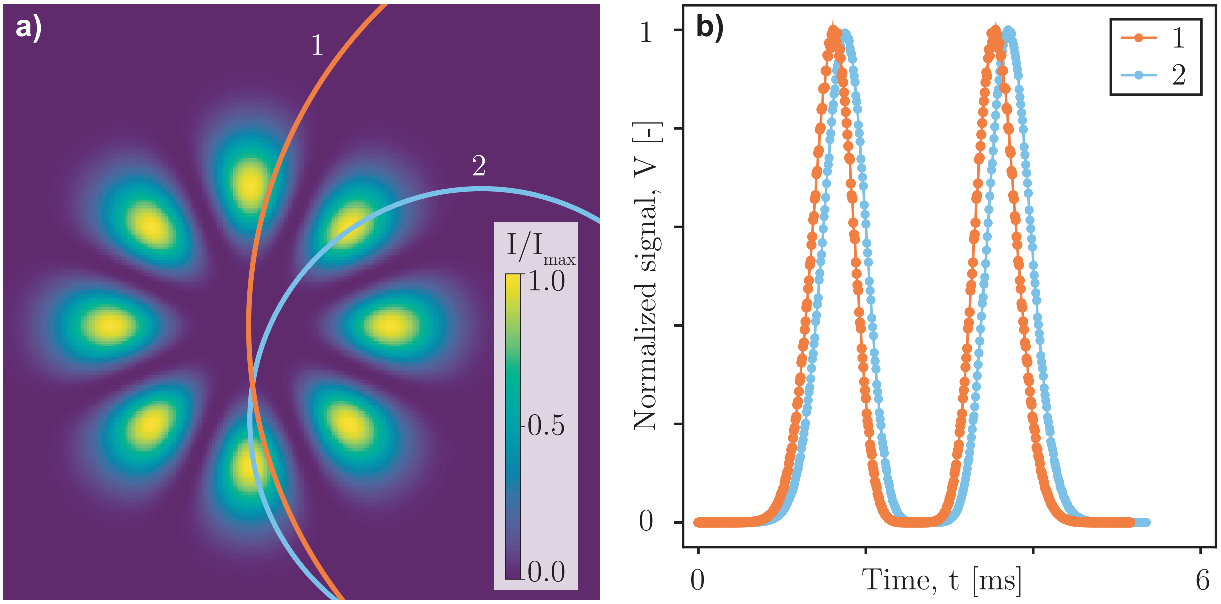

Figure 2.7: Particles traveling with different angular velocities on orbits of different sizes can generate similar signals. a) particle trajectories with 1: $\Omega = 600$ rad/sec and $R = 426$ pixels and 2: $\Omega = 312.5$ rad/sec and $R = 220$ pixels. b) simulated time series for particle trajectories shown in a), each normalized by its maximum value. Traces offset by 0.12 ms for clarity. Parameters for trajectories 1, 2: $D = 425,\ 238$ pixels and $\phi = 0.393,\ -0.005$ rad. In both cases, $r = 20$ pixels and $l = \pm 4$.

In this proof-of-concept demonstration, we have chosen to sacrifice uncertainty for simplicity. Nonetheless, we have identified several ways to reduce the uncertainty of the measurements. We expect that the contribution to the uncertainty from the non-orthogonal basis functions can be refined by training, evaluating, and using the model with multiple parameterizations of each burst. One approach to improve the uncertainty of the sensor due to the geometry is to first determine which bursts can be generated by more than one set of orbit centers, orbit radii, and angular velocities, and then to exclude these bursts from analysis by preventing their use in training the model and by rejecting them from being evaluated by the model. An alternate approach is to limit the parameter range used to train the model to a narrow window centered about the expected flow conditions.

A different strategy to improve the uncertainty of these measurements is to modify the illumination beam, optimizing it so that non-unique signals are not generated in the first place. Building on the previous work of Refs. [1, 2], we developed and tested this signal processing toolbox using a probe beam consisting of conjugate LG beams which formed a petaled pattern. However, we expect that better spatially structured beams could be optimized to augment angular velocity predictions. For example, an asymmetric pattern could be used to reduce the set of possible parameter combinations that can generate any given signal and to disambiguate direction. Further direction disambiguation could be accomplished by structuring the polarization field[72].

In this study, we have fixed the size of the scattering particle with a radius $r = 20$ pixels. Recalling that the scattering particle acts as a blurring filter, changing its size to smooth different amounts of the beam may serve as a means for tuning the uncertainties discussed above. Likewise, increasing l might reduce the number of non-unique bursts.

When using this sensor in a flow which evolves more slowly than the time it takes to conduct multiple measurements, the uncertainty of the angular velocity could be further refined with a statistical treatment of the predicted angular velocities using a Student's t-test since the distributions of Ω_p about Ω_A are well approximated with normal distributions.

In this demonstration, we extended the traditional capabilities of laser Doppler velocimetry by developing a signal processing toolbox which predicts the angular velocity of a particle traveling on a circular orbit using a machine learning approach to develop a model to relate parameterizations of a signal to the angular velocity. This strategy was shown to be particularly effective in predicting the angular velocities of small particles traveling on circular orbits, where no one-to-one relationship existed between characteristics of the scattered light signal and the spatial pattern of the illuminating beam. We also point to the possibility of predicting related or different kinematic quantities such as the location of the orbit center or accelerations with a similar machine learning-based signal processing scheme.

2.6 Current sensor limitations

As with any sensor, we expect this angular velocity sensor to function only within a certain parameter range. In this section, we first discuss why this sensor is capable of measuring the angular velocities of particles moving only along arcs with radii below a critical radius set by the size of the interference patterns. Next, we discuss the minimum and maximum angular velocities we expect the sensor to be able to resolve. Additionally, we describe the spatial and temporal resolutions of the sensor. Then, we touch on the physical limitations which set the beam size and the particle size. Finally, we discuss how this measurement has no depth resolution.

2.6.1 Orbits require curvature through interference fringes

As the orbit radius R grows large relative to the interference fringes, $R \gg w_0\sqrt{|l+1|/2}$, the particle trajectory becomes increasingly well approximated using the first order, straight line tangent to the arc. We call this trajectory R_∞. This concept is illustrated in Fig. 2.8a, where we show particle trajectories of several radii, all passing through the same point with the same tangent velocity, $V = 2\pi R\Omega$. As R grows, much of the particle trajectory through the interference fringes mimics that of the tangent, and only as the particle first enters and finally exits the interference fringes do deviations of the trajectory from that of the tangent appear. In the inset of Fig. 2.8b we plot the time series which correspond to the trajectories plotted in Fig. 2.8a. We see that as the orbit radius approaches the tangent line ($R \to \infty$), the signals begin to resemble each other.

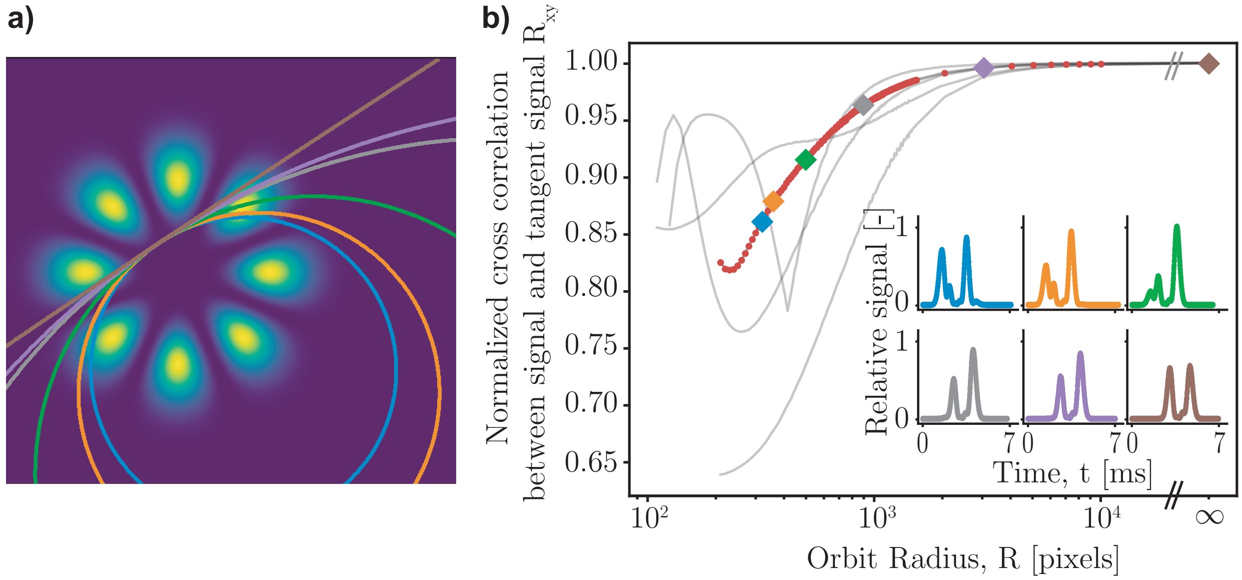

Figure 2.8: a) As the orbit radius R grows, the trajectory of a particle moving through the interference fringes approaches that of the tangent to the arc. Colors of trajectories match those in panel b) and correspond to orbit radii $R = [200, 260, 400, 900, 1210, \infty]$. All arcs pass through $(50, 5\pi/16)$, and all arcs share the tangent shown in brown. b) Normalized cross correlation R_{xy} between each signal and its corresponding tangent. Each gray line corresponds to R_{xy} for sets of arcs passing through several randomly chosen different common points. The gray line with red circles corresponds to the common point illustrated in panel a). Inset: signals corresponding to those in panel a) and indicated with colored diamonds in panel b).

When $R > R_c$, where R_c is the critical orbit radius above which curvature in the trajectory is negligible, the values of R and Ω become ambiguous. That is, the tangent velocity could be the product of any $R > R_c$ with a compensating angular velocity Ω to yield V. Therefore, we expect our sensor to function only for $R < R_c$.

The specific value of R_c is a function of $r,\ l,\ w_0,\ D$, and ϕ. Instead of calculating R_c we use the normalized cross correlation R_{xy} defined in Eq. 2.8 to compare bursts from a set of simulated particle trajectories which pass through the same point within the interference pattern but have orbits with different R to the burst corresponding to the tangent trajectory through the common point. In this normalized cross correlation, x and y represent time series corresponding to the trajectories with orbit radius R and R_∞, respectively. To facilitate this comparison, all particles pass through the common point with the same tangent velocity V calculated as $V = \Omega / (2\pi R)$ for $R \neq R_\infty$. Because the orbit curvature of particles on transits with $R > R_c$ is negligible through the interference pattern, the normalized cross correlation of bursts corresponding to these conditions with the burst of the tangent case is close to 1. The influence of nonnegligible orbit curvature manifests as a difference in the beginnings and ends of a burst and results in a normalized cross correlation less than 1. The results of this comparison are shown in Fig. 2.8b as a function of R. To emphasize the strong dependence of this function on D and ϕ, R_{xy} is plotted for several different common points with different tangent angles. We define R_c as the radius at which R_{xy} is greater than 0.98. In the case of the data shown in Fig. 2.8, $R_c \approx 1000$ pixels.

In principle, the angular velocity of a measurement which predicts $R > R_c$ should not be accepted because of the ambiguity between $R > R_c$ and Ω discussed above. To avoid needing to reject measurements in our proof-of-concept sensor demonstration, we estimate that $R_c \approx 1000$ pixels at every point, and we use only $R < 1000$ pixels in both the training and test data to eliminate any trajectories which might resemble the tangent trajectory.

2.6.2 Sensor resolution

As the angular velocity increases, the number of sampled points per burst decreases for a fixed sampling rate. With fewer data points, the number of degrees of freedom in the burst parameterization fits decreases. As the number of degrees of freedom decreases, so too does the quality of the fit. At a minimum, these fits require the same number of points as there are parameters, which here is $3 \times 2l + 1 = 25$. However, we found that when bursts had fewer than approximately 50 points, the fitting scheme was sensitive to noise in the burst. Therefore, we established a criteria for selecting fits for use in training or testing the machine learning model which controlled the quality of the fit, accepting fits only if their coefficient of determination $r^2 > 0.9$, meaning that the model explained more than 90% of the variation in the burst. For a given trajectory, increasing the sampling frequency increases the number of points in the burst, so the angular velocity range can be tuned by modifying the sampling frequency.

The temporal resolution of each measurement is given by the duration of the burst: $\delta t = t_{burst}$. An upper limit of the time resolution can be estimated from the time it takes a particle orbiting with the smallest angular velocity along the smallest orbit to traverse the widest portion of the beam, $\delta t_{max} \approx 2r_p/(R\Omega)$. Figs. 2.1, 2.3, 2.5, 2.7, and 2.8 have t_{burst} on the order of 10 ms. Increasing the angular velocity refines the temporal resolution.

We define the spatial resolution of the sensor δx to be the distance between the probe beam and the center of orbit of the particle. Given a particular center of orbit (D, ϕ), δx is limited by $D - r_p - r < \delta x < D + r_p + r$ since only orbits which transit the beam are measurable. The upper limit of the spatial resolution is approximated by $\delta x_{max} \approx D_{max} + r_p + r$, where D_{max} denotes the furthest center of orbit from the beam of light about which particles traverse the beam on trajectories with $R < R_c$. The spatial resolutions of the bursts described above are approximately $\delta x_{max} \approx 1500$ pixels = 1.45 cm.

2.6.3 Physical limitations to probe size

In this demonstration, we have fixed the sizes of both the particle and the interference pattern while we have varied the other parameters with the goal of predicting the angular velocity and the orbit radius of a particle embedded in the flow. However, both the particle size and the interference pattern size can be changed.

As in other velocimetry sensors which use scattering particles, particle radii r should be set by the parameters of the flow such that the particles are neither too small to have motion dominated by Brownian motion nor too large to carry enough inertia to travel along paths which are not fluid pathlines [8].

The scattered light must have ample power to be distinguished from noise by the detector. This power is limited by the intensity of the incident beam, which, given a laser source can be limited by two factors, the efficiency of reshaping the Gaussian intensity profile from the laser to the requisite LG modes, and the ultimate size of the beam. When an LG beam is generated from a beam with a Gaussian intensity profile and a fixed beam waist w_0 using an LCOS-SLM as was done in this project, the efficiency of the diffraction gratings decreases as l increases due to the decreasing spatial overlap between the input and desired mode [65]. The transverse spatial extent of the generated LG beam can be altered using a telescope setup after the LCOS-SLM. As the size of the beam increases, its total power remains constant, so the power incident on the scattering particle diminishes.

We expect that the smallest beam size possible is limited by the visibility of the fringes, the ratio of the intensities of the radial peaks and nulls. As the beam size decreases past approximately the wavelength of the light, this visibility decreases, and the fringes appear to bleed into one another [73]. Though we did not study its effect in this chapter, we expect this decreased visibility to directly impact the sensor resolution by decreasing the sizes of the features in the bursts.

The ratio of the particle to interference pattern sizes is very important to the behavior of this sensor. Recall that the particle acts as a blurring function on the interference fringes. If the size of the particle is such that it occupies one fringe and one null of the interference pattern, one can imagine how moving the particle through an intensity peak, into an intensity null, and back through a different intensity peak would decrease the contribution to the blurred intensity from the waning edge while symmetrically increasing the contribution to the blurred intensity from the waxing edge, resulting in little signal modulation. In the case of laser Doppler velocimetry, the problem of selecting relative interference fringe and particle sizes to maximize the signal to noise ratio has been studied extensively [8]. While we did not study the effect of relative sizes in this chapter, we do expect this to be an important parameter for designing specific implementations of this sensor.

2.6.4 Depth of measurement

The sensor we have demonstrated has no longitudinal sensitivity. That is, the scattered light we measure contains no information regarding the depth of the particle. We expect that in future iterations of this sensor, this limitation could be lifted by incorporating a confocal sectioning geometry into the probe beam, by relating the absolute scattered intensity to the absorption of the fluid which scales linearly with depth according to Beer's Law, or by selectively seeding the flow.

2.7 Chapter Conclusion and Future Work

In this chapter, we have developed a sensor which uses structured light and machine learning to predict flow properties. Specifically, we have demonstrated that we can calculate the angular velocity of particles traveling in a 2D flow along circular arcs by analyzing the intensity of the light they scatter. In laser Doppler velocimetry, the analogous technique used to sense linear components of the velocity vector, these components are directly related to the spatial and temporal frequencies of the illuminating interference fringes and the scattered light. In contrast, no simple mapping from the spatial pattern of the light and characteristics of the signal exists for predicting the angular velocity with this sensor. However, a machine learning regression model trained on simulations of the expected scattered light was shown to be capable of predicting the angular velocities of scattering particles to within uncertainties of, on average, ±14%. While many possible probe beam conformations exist, we have explored just one geometry. We suspect that other flow properties can be inferred using different probe beams with a similar signal processing scheme to the one presented here.

In Sec. 2.2 we presented mathematical model we implemented to simulate the expected signals. In Sec. 2.3, we described idealized experiments to validate the simulations. In Sec. 2.4, we detailed our signal parameterization approach, noting that because the Gaussian basis functions we used were not orthogonal, the resulting parameters had strong dependencies on how our fits were initialized. Consequently, the ML model was trained using particular instances of many possible parameters. Because the ML model was able to handle this variability, we suspect that our sensor would still function in more complex experimental environments which may induce random intensity fluctuations in the resulting signals. Such effects might mirror the effect of the non-orthogonal basis functions, both inducing a degree of variability on the output parameters. Here, by using non-orthogonal basis functions, we artificially introduce variability into the ML model, and we suspect that this facilitates studying noisier signals.

There remain ample opportunities for refining this sensor. We attempted to adapt the ML model to simultaneously predict combinations of variables in addition to the angular velocity, but we found that these predictions were poor. One interesting direction is to design the ML model to return a probability distribution of the possible angular velocities instead of a single value. Because the uncertainties associated with non-unique bursts arising from the multiple parameter configurations like that illustrated in Fig. 2.7 are restricted to quantized values, the outputs of such a model could be compared to physical intuition or multiple measurements to refine the selected angular velocity.

We expect that with a different structured light pattern, predicting such quantities as the direction in which the particle orbit is centered might be possible. Also, probing the flow with multiple, potentially multiplexed, light patterns could provide additional information to improve precision and accuracy or open up a broader range of parameter prediction. This could be done either simultaneously by multiplexing several patterns on beams with different polarizations or wavelengths, or by changing the patterns as a function of time.

The sensor we developed predicts the angular velocities of particles traveling on circular orbits in a plane orthogonal to the probe beam but in its current implementation does not allow for this plane to be positioned at a different angle relative to the beam. If the beam and the plane of orbit were not orthogonal, the particle would no longer appear to travel with a circular orbit and would instead take an elliptical trajectory through the beam. To extend our sensor to 3D, we anticipate that the longitudinal Doppler shift of the scattered light [40] could be incorporated into the ML model.

In its current form, the sensor we present in this chapter measures angular velocities. Measurements of angular accelerations may also be of interest. Such measurements could be possible if the particle accelerated on, or faster than, a time scale set by the residence time (the time the particle is in the probe volume), $\tau \approx 2r_p/U_\perp$, where $U_\perp = \Omega R$. While the rotational Doppler shift has been used to measure angular accelerations by creating spectrograms which monitor the frequency shift as a function of time [41], we expect that adapting such a paradigm to this problem would be challenging due to the short expected residence times. Expanding the parameter space of the machine learning model to include accelerating particle trajectories might be a more viable strategy.

In cases of simple motion like particles moving in straight lines or particle orbiting about a known point on circular trajectories, structured probe beams can be engineered which yield readily interpretable signals [17]. Here, we have attempted to address the question of what are we to do when the motion we expect is more complicated? In particular, we have studied particles which orbit according to circular trajectories, but these orbits are not concentric with the probe beam. The sensor we have developed measures the angular velocities of particles obeying such circular trajectories offset from the probe beam axis. We have accomplished this by developing a more sophisticated signal processing strategy. We have shown that, even if the motion and the structure of the light no longer match, a history of the particle's kinematic information can be revealed from the information encoded in the signal. However, we have found that a new form of uncertainty which previously did not exist is present in this more general case because signals may no longer uniquely correspond to the parameters of interest.

As we noted above, this uncertainty can be overcome by excluding signals like those shown in Fig. 2.7 known to have multiple possible origins, by refining the machine learning model, or by illuminating the flow with multiple, potentially multiplexed, light patterns. However, we must ask, if there does not exist a single pattern of structured light which can provide signals which are easy to interpret, does there exist some optimal probe beam structure? To begin to offer an answer to this question, we draw an analogy to the field of compressive sensing. A major finding which has propelled the field of compressive sensing in recent years is that samples of sparse signals collected as the inner product of random vectors with the signal can, with high probability, reconstruct the signal nearly perfectly [74]. This is because sampling randomly in this way spreads the information contained in the signal efficiently across many of the measurements. Likewise, we expect that illuminating the fluid with a known but random structure of light could encode bursts with more information by which to identify the parameters which generated them. Ultimately, combining such an illumination pattern with a machine learning-based signal processing scheme might facilitate more precise measurements.

Chapter 3

Aligning a beam to a rotating surface

3.1 Introduction

In applications ranging from manufacturing to physics experiments, it can be necessary to center a beam of light to the axis of rotation of a rotating surface. For example, fabricating high precision components like diffractive optical elements (DOEs) may require aligning a beam of light to the axis of rotation of a spindle[76, 77, 78, 79]. Misalignment in these manufacturing processes limits the quality of the DOEs that can be produced[79]. One common alignment strategy used in these industrial applications involves focusing light onto a grating affixed to the rotating surface and imaging the interference fringes formed by the overlapping +1st and zeroth orders and the overlapping −1st and zeroth orders[80]. A beam not centered on the axis of rotation translates over many grating lines as the grating rotates, causing relative movement of the interference fringes. As the alignment between the beam and the axis of rotation improves, this fringe movement decreases, eventually ceasing with perfect alignment. Yet, aligning a beam to a surface in this way can introduce technically demanding limitations into the entire optical system. For example, wavefront aberrations of the light incident on the grating must be minimal, as these can give rise to both changing numbers of fringes and distorted shapes which complicate the analysis[80]. An alternative alignment strategy designed with applications in microfabrication in mind can be used to position

---

This chapter is adapted from E. F. Strong, et al. “Centering a beam of light to the axis of rotation of a planar object,” Ref. [75].

a beam perpendicular to a spinning surface at a fixed offset from the axis of rotation[81]. This technique entails mounting a specially designed mirrored beam splitter to the rotating surface and monitoring the reflected beams with quadrant photodetectors[81]. Yet, like the alignment technique from Ref. [80], this technique from Ref. [81] requires mounting bulk optics to the rotating surface, which may be difficult in fragile or compact systems. Doing so could strain the mechanical system, shifting the position of the axis of rotation found in the alignment process from that in the intended application.

In the research lab, a high degree of alignment to a rotating surface is required for studying the rotational Doppler effect (RDE). The prototypical RDE experiment involves measuring the angular frequency of a surface rotating at a prescribed frequency Ω using changes in the orbital angular momentum (OAM) between the incident and scattered light[22, 38]. Typically, the illuminating light comprises two OAM modes, $\pm l\hbar$. In this case, the change in OAM between the incident and scattered light is detected as an intensity modulation, and is expected to occur with a frequency $f_{mod} = \Delta l \Omega/(2\pi)$, where $\Delta l = 2|l|$. In practice, however, intensity modulations may also be detected in the harmonics of $f = \Omega/(2\pi)$[82]. This can occur if the OAM of the light differs from the anticipated $\pm l$. Such discrepancies between the expected and the actual OAM modal spectra can be caused by misalignment between the axis of rotation of the spinning surface and the direction of propagation of the beam, angularly, translationally, or in both degrees of freedom[46, 83, 84, 85]. For example, a Laguerre Gauss (LG) beam comprising the $\mathrm{LG}_{l=1}^{p=0}$ mode displaced laterally by a fraction of a beam waist, $0.8w$, retains less than 40% of its energy in the intended LG_1^0 mode, with energy distributed in the beam's surrounding l modes[46]. This is because the OAM modal spectrum can have an extrinsic contribution, meaning its modal spectrum depends on the frame of reference in which it is measured[46, 85]. Therefore, if the beam is mispositioned, laterally displaced from the axis of rotation, the actual OAM of the light incident on the rotating surface might not necessarily be the intended $\pm l$. A broadened spectrum can lead to errant heterodyne beat notes in the acquired signal which can complicate analysis and create ambiguities. Drawing fundamental conclusions from RDE experiments, then, requires that the incident OAM modal spectrum be well characterized. This, in turn, implies that the light must be well aligned to the spinning system.

While aligning the beam to the spinning surface angularly can be accomplished by retracing back reflections from the surface back through the system, ensuring the beam is translationally aligned to the axis of rotation of the surface is more challenging. One possible strategy for translational alignment is to use the RDE, the very effect the experiments of Refs.[22, 38, 83, 84] seek to characterize, and to maximize the power in the expected frequency f_{mod}. If Ω is not known *a priori* but the spacing between the harmonics of f can be resolved, the spacing between these harmonics can be used to determine Ω. Then, the power in the harmonic at f_{mod} can be maximized. However, if the OAM modal spectrum decomposed about the axis of rotation of the rotating system differs from the intended $\pm l$ due to the compounded effects of poor angular and translational alignment[85] or imperfect OAM generation, this strategy can result in unintended misalignment. Therefore, an alignment strategy distinct from the RDE measurement is necessary.

Here, we present a simple, translational alignment technique which positions the beam centroid on the axis of rotation of the rotating surface with an estimated error of $\pm 1\%$ of the beam waist. This technique provides a low-profile and simple alternative to other alignment techniques for applications which cannot tolerate the weight or space of bulk optics mounted on the rotor or for applications which involve incoherent light which would preclude monitoring interference fringes. This alignment technique involves segmenting a rotating surface into two portions, one with a detectibly higher reflectivity than the other, with their interface passing through or close to the axis of rotation. This can be accomplished by, for example, adhering a strip of retro-reflective tape to the surface, positioning its edge close to the axis of rotation of the surface. As this bireflective surface rotates, the light scattered from it is detected and analyzed. Whereas the scattered intensity from a well-centered beam has little dependence on the orientation of the rotating surface, that from a misaligned beam peaks when the beam primarily illuminates the more reflective side and dips when it illuminates the less reflected side. Our alignment technique involves minimizing the variation in the intensity of light scattered from the rotating surface. We conduct experiments to benchmark the performance of this centering technique, using the beam centroid coordinates on a digital micromirror device (DMD) determined using a knife-edge test as the true position of the axis of rotation. We conduct experiments with a Gaussian beam, but we note that this technique could be feasible using any beam such as an LG beam. The structure of this chapter is as follows. In Sec. 3.2 we describe the technique. Next, in Sec. 3.3 we experimentally demonstrate the technique. In Sec. 3.4, we detail the simulations used to estimate the uncertainty of the technique. Finally, in Sec. 3.5, we conclude.

3.2 Description

It is well known that the intensity of scattered light from a diffuse surface is a function of the surface reflectivity. If a surface is engineered to have a known spatially varying reflectivity, the relative intensities of light scattered from different regions of the surface can be used to determine position of the beam incident on the surface.

Consider a target comprising two surfaces with different reflectivities which meet at a linear interface. When this target moves through the beam, the intensity-weighted fraction of the beam scattered by each surface changes at a rate given by the velocity of the interface and the intensity profile of the beam. For example, in the case of such a reflector translating through a Gaussian beam, the intensity of the light scattered from the leading surface diminishes as the intensity of the light scattered from the trailing surface grows. The total light scattered from this reflector is the sum of the intensity-weighted fraction of the beam scattered from each material. Encoded in the intensity of the scattered light is information about the size and position of the incident beam. In the same way that knife-edge profilometry uses intensity or power measurements of various masked portions of a beam to determine the transverse profile of the beam[86, 87, 88], light scattered from these surfaces can also be used to construct a beam profile. Importantly, however, if we know or make assumptions about the beam profile a priori, we can also locate the beam relative to the interface of the two materials.

To begin, we assume that the beam incident on the spinning surface is axisymmetric, noting that if the beam is not axisymmetric, this method will align its centroid, which may differ from its center, to the axis of rotation. We make one portion of the rotating surface detectably more reflective than the other by, for example, covering one side of the surface with a strip of reflective tape that scatters more light than the surface itself does. The positioning of the tape is not critical, as will be discussed below, though the shortest distance between its edge and the axis of rotation ϵ should be roughly less than a beam waist w. When the surface spins, variations in the scattered intensity are periodic with the angular frequency of the surface, Ω. This concept is illustrated in Fig. 3.1, where we show how the scattered intensity fluctuates when a beam is off center from the axis of rotation by a distance δ, but remains relatively constant when a beam is coaligned with the axis of rotation.

Whereas a beam offset from the axis of rotation by a distance δ alternately scatters high and low intensities as the surface rotates, the intensity variations of the scattered light of a centered beam are small and are limited by the quality of the incident beam. This is because, in perfect alignment, the intensity-weighted fraction of the beam reflecting from each of the two surfaces is invariant under rotation. In contrast, if δ is nonzero (misalignment exists), the intensity-weighted fractions of the beam scattering from the two surfaces depends on the rotated surface angle ϕ. Translating the beam across the rotating surface towards the axis of rotation decreases the peak-to-peak variation of the intensity or the power of the scattered light as the surface rotates. Therefore, minimizing this peak-to-peak variation by adjusting the relative positions of the rotating surface and the incident beam serves as a viable strategy for centering the beam on the rotating surface.

3.3 Experimental Demonstration

To demonstrate our alignment technique, we experimentally replicate a spinning surface using a digital micromirror device (DMD, Texas Instruments DLP4500) so that we can verify the positioning of our beam relative to the location that will serve as the axis of rotation with a second, independent measurement: a knife-edge test. This allows us to perform highly controlled experiments in which we translate the spinning structure relative to the incident beam of light by playing a different video on the DMD, rather than physically moving it or the spinning surface.

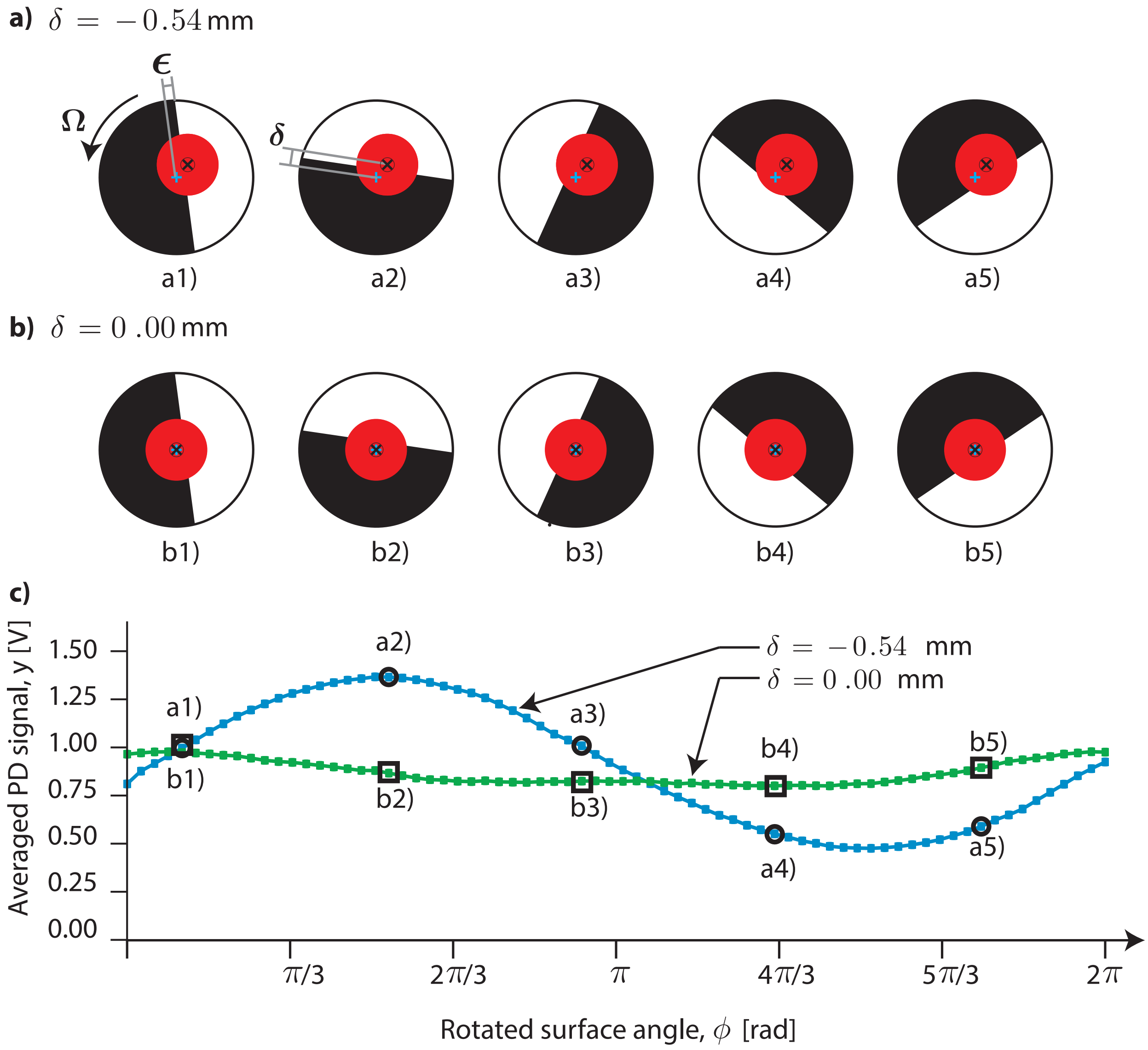

Figure 3.1: A surface rotates with an angular frequency Ω. A Gaussian beam (red) is (a) misaligned and (b) aligned to the axis of rotation of the spinning surface, offset from it by a distance δ. More light scatters from the more reflective surface (white) than from the less reflective surface (black).The interface between these two surfaces lies at the shortest distance ϵ from the axis of rotation. (c) Experimental data corresponding to the configurations in (a) and (b). Fluctuations in the averaged photodetector signal arise due to variations in the amount of the Gaussian beam sampled by the reflective surface. These fluctuations depend on the relative orientation of the surface and the beam. $\epsilon = 0.51$ mm, $w = 1.05 \pm 0.03$ mm. δ, indicated in the figure, is referenced to the centroid of the beam found using the knife-edge test.

Our experimental setup, shown in Fig. 3.2, is based on those from Refs. [22, 38, 83, 84], but we have replaced the spinning disk from these experiments with a DMD. Typically, RDE experiments display computer generated holograms (CGH) on a liquid crystal on silica spatial light modulator (LCOS-SLM) to generate light with OAM. Here, we use our LCOS-SLM (Cambridge Correlators, SDK1024) to direct a Gaussian beam into the same angle OAM beams generated for RDE experiments would diffract. We note that the LCOS-SLM is not necessary and is only included here for completeness, as it was used in our experiments. After the LCOS-SLM, we spatially separate the diffracted orders and isolate the first diffracted order with a spatial filter. The light from this order is then directed to the DMD. A video playing on the DMD effectively samples the incident beam. The sampled portions of the beam impinge on a photodetector (Thorlabs, DET36A). In these experiments, we average 0.3 seconds of data collected at 100 kHz for each video frame. The uncertainty of each data point is calculated as the standard deviation of the signal over the averaging time.

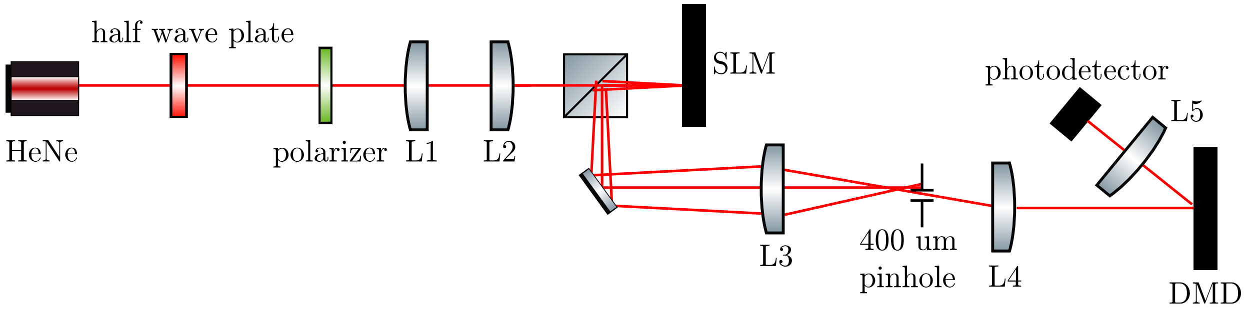

Figure 3.2: Experimental setup. The size and polarization of a beam from HeNe are prepared and directed to a spatial light modulator (SLM), which displays a computer generated hologram (CGH). Light diffracts from the CGH into many orders, but we select only the first order with a spatial filter. This order is then sent to the digital micromirror device (DMD), which replicates a spinning surface. Light sampled by the DMD is collected on the photodetector. L#: lenses.

Prior to determining the translational position of the beam to the surface of the DMD, we confirm the beam is normally incident on the flat mirrors of the DMD to within approximately 1.15° by ensuring its backreflection from the DMD is centered on the 400 μm diameter pinhole of the spatial filter after being focused by lens L4 (focal length 100 mm). If the reflected light traveled at an angle different than that of the incident light, the reflected spot was visible on the housing of the pinhole. Iteratively rotating the DMD to narrow in on the angle which the spot appeared on opposite sides of the pinhole, we were able to set the angle so the reflected beam passed through the hole. Accordingly, the perpendicularity is calculated as the ratio of twice the beam waist to the focal length of the lens. Next, we identify the position of the beam centroid as well as the beam size with a knife edge test replicated on the DMD in two orthogonal directions. Note here that, while it is known that skew can affect some results of the knife edge test, skew has no impact on determining the position of the centroid of a Gaussian beam. Later, in Sec. 3.4, we will find that simulations which the beam waist extracted here agree quite well with our experimental data, suggesting the influence of any remaining skew on the beam waist is minimal. In our knife edge test, we program the DMD to sample light from the incident beam in the same way that a knife moving through the beam does, sending samples of the beam to the photodetector. Fitting an error function to the averaged data plotted as a function of the position relative to the lower left corner of the DMD, we find that the beam is located at $(6.39 \pm 0.03$ mm, 5.54 ± 0.03 mm) and has a $1/e^2$ beam waist $w = 1.05 \pm 0.03$ mm. The uncertainties in these measurements arise due to the discretized nature of this knife edge test and correspond to the distance between successive samples.

Now that we know the location of the beam's centroid, we test the proposed alignment technique. We program the DMD to play a video replicating the spinning disk described above in Sec. 3.3. We vary the center of rotation along (6.35 mm, $5.54 + \delta$ mm), where $-0.44 \leq \delta$ [mm]$\leq$ 0.49 for 4 values of ϵ, where $0.04 \leq \epsilon$ [mm]$\leq$ 0.72. We show representative samples of the resulting averaged signal from the photodetector, y, as a function of the rotated surface angle ϕ for $\epsilon = 0.29$ in Fig. 3.3a. From these and similar traces, we extract the peak-to-peak voltages V_{pp}, the difference between the maximum and minimum y of the trace. The uncertainty of V_{pp} is calculated as the uncertainties of the maximum and minimum of y added in quadrature. V_{pp} for all experiments is shown in Fig. 3.3b. Note that effects leading to a bias in the background signal on the photodetector (e.g. ambient light) are eliminated when we calculate V_{pp}.

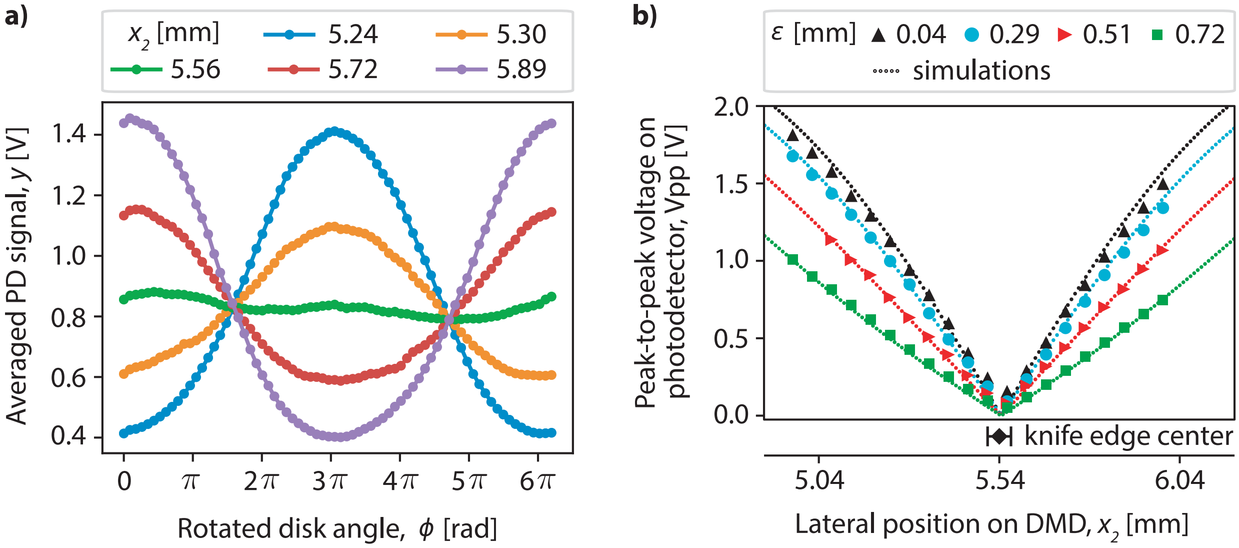

Figure 3.3: (a) Representative averaged signals from the photodetector y as a function of the rotated disk angle ϕ for various lateral positions of the axis of rotation on the DMD, x_2. Recall that the centroid found by the knife-edge test is 5.54 ± 0.03 mm. Uncertainty bars, which correspond to the standard deviation of the averaged signal for each frame, are smaller than each point. $\epsilon = 0.29$ mm. (b) Peak-to-peak voltage on the photodetector, V_{pp}, as a function of the lateral position of the axis of rotation on the DMD, x_2, for various ϵ. Experimental and simulated data are indicated with the symbols and the dotted lines, respectively. Uncertainty bars corresponding to the uncertainties of the minima and maxima of y used in generating V_{pp} added in quadrature are smaller than the data points. Also indicated is the centroid as measured by the knife-edge test (black diamond). In contrast to the other data points, the uncertainty in the position of this knife-edge centroid is much larger than the data point and is indicated with the horizontal error bars.

As discussed previously, if the center of rotation was perfectly aligned with the beam, we would expect no modulation ($V_{pp} = 0$) in the signal as a function of the rotated surface angle ϕ because at every angle, the sampled intensity-weighted fraction of the beam would remain constant. For nonzero δ, however, this sampled portion of the beam varies as the reflective surface sweeps through changing fractions of the beam with ϕ, so $V_{pp} > 0$. This increasing dependence of y on ϕ as δ increases can be seen in the traces in Fig. 3.3a. Minimizing V_{pp} sets the x_2 position of the beam centroid. To completely center the beam, this procedure should be repeated in the x_1 direction. We note that this technique can be implemented in real time, monitoring V_{pp} with an oscilloscope.

3.4 Simulations

In the experiments, the centroid position found using the knife edge test has a relatively large uncertainty. We anticipate the uncertainty of the centering technique discussed in this chapter is much smaller, and thus the knife edge test does not provide an accurate enough "truth" to assess the uncertainty. To estimate the uncertainty of our centering technique, we turn to simulations.

In simulating our centering technique, we calculate the spatial intensity of a Gaussian beam with the same beam waist as the experiments, $w = 1.05$ mm. Then, for each ϵ, we calculate V_{pp} as the difference between the summed intensity of the beam with a) $x_2 < \delta + \epsilon$ and b) $x_2 \geq \delta - \epsilon$. These sampling positions capture the minimum and maximum expected intensities sampled by the spinning surface, respectively. To match these simulations to our experiments, we assume that the only light that scatters from the rotating surface is that which is incident on the more reflective of the two surfaces. We model this reflective surface as a perfect mirror (reflectance=100%), and we assume that the reflected intensity corresponds linearly to the anticipated signal on the photodetector. To superimpose the simulated data on our experimental data, we calculate a scaling parameter by dividing the summed intensity of the entire simulated Gaussian beam by the maximum averaged signal on the photodetector, y, found in the knife edge test when the entire beam is directed to the photodetector. The same value of this scaling parameter is used in each of our simulations for $\epsilon = \{0.04,\ 0.29,\ 0.51,\ 0.72\}$ mm.

As shown in Fig. 3.3b, we see good qualitative agreement between our simulations and our experiments. These simulations suggest that the uncertainty in the technique is less than 0.01 mm (1% of the beam waist), the smallest possible uncertainty permissible in these experiments due to the size of the individual mirrors of the DMD. Note that these simulations assume the maximum difference in reflectivity between the two surfaces. We anticipate that outside of this limit, if the surfaces had more similar reflectivities, this could increase the magnitude of the uncertainty.

3.5 Discussion

As misalignment between the beam centroid and the axis of rotation δ tends to 0, the variation of the intensity as measured by the photodetector output, V_{pp}, decreases. Therefore, translating the axis of rotation through the light, or vice versa, and finding the location which minimizes V_{pp} can be used to align the axis of rotation to the beam centroid. As shown in Fig. 3.3b, the minima of V_{pp} for each transit of a spinning structure through the beam corresponds well with the known centroid position to within the uncertainty of the centroid position, where $\delta = 0 \pm 0.03$. Our simulations, which show good qualitative agreement to the data, suggest that the uncertainty of this centering technique demonstrated in these experiments is on the same order as the size of the individual mirrors of the DMD, ±0.01 mm. We expect that the uncertainty of our centering technique is limited by pixilation from the mirrors, and thus better performance would be possible with a device with smaller mirrors or by making the entire rotating structure monolithic. Indeed, knife edge profilometry techniques have been demonstrated in non-discretized systems to have a precision of approximately $1/8\lambda$ [89]. We find that this alignment technique is insensitive to the position of the interface between the two reflective portions of the surface when ϵ, the shortest distance between the interface and the axis of rotation is smaller than the beam waist w, $\epsilon < w$. As long as the scattering surface is segmented within approximately the beam waist of the axis of rotation, the strategy proposed here can be used. The implication of this is that with just a strip of reflective tape crudely placed such that its edge passes close to but not necessarily through the axis of rotation, quick and easy centering can be performed. Here, we have experimentally demonstrated how minimizing V_{pp} can be used to radially align a beam to the rotation axis of a planar object. We identified the centroid of a beam using a standard knife edge approach, and then we used our V_{pp} minimization technique to find the same centroid by scanning the axis of rotation of a spinning structure. While we only minimized V_{pp} along one direction, we note that this technique can be used to minimize δ along a different subsequent direction. We have demonstrated this alignment technique using a Gaussian beam, but we expect that the same strategy could be developed for any beam, like an LG beam. While this alignment technique was developed with RDE experiments in mind, we anticipate that it could be useful in other applications where radial alignment is critical, as in precision manufacturing. The simplicity of this alignment technique makes it a good candidate for systems which cannot tolerate mounting additional optics to the rotor. Because variations in the intensity (or power) underlie the technique and imaging interference fringes is not necessary, this strategy can be implemented for beams which may have aberrations, and it can be used with incoherent light.

Chapter 4

Hyperspectral imaging using dual frequency comb spectroscopy and compressive sensing

In this chapter, we develop a hyperspectral imaging modality which uses dual frequency comb spectroscopy (DCS) and compressive sensing. In particular, we develop and demonstrate a means for refining the transverse spatial resolution of spectroscopic measurements conducted with dual frequency combs using a single pixel camera experimental architecture. Hyperspectral imaging is a technique which captures spectrally- and spatially-resolved images [90]. DCS is a powerful technique for high resolution spectroscopy and has been shown to be an excellent tool for studying the thermodynamic conditions of harsh, gaseous environments due to its high spectral resolution, large bandwidth, and speed [91, 92]. Yet, DCS requires a fast detector that cannot be arrayed. Therefore, DCS measurements with sub-beam-width spatial resolution have not been demonstrated, and generating spectroscopic images would require scanning the probe beam. Implementing such scanning systems with moving hardware is technically challenging, and generating the image pixel by pixel may be slow. Therefore, in cases where such resolution is critical, as in measuring temperature profiles at flame edges, an alternative strategy is required.

Here, we develop a compressive sensing-based strategy which shifts the experimental burden of imaging to the computational domain. In particular, we use a high-speed single pixel detector in conjunction with a digital micromirror device (DMD) to give our spectroscopic measurements spatial resolution across the transverse extent of the beam. As a demonstration, we measure the concentration of methane across the beam path. We implement a smashed filter which reconstructs the path length of methane across the beam. This concept is illustrated in Fig. 4.1. Such measurements which pair DCS with structured detection are, to the best of our knowledge, the first of their kind. We expect that this imaging modality will find use in thermography and gas imaging, since spatially resolved, high fidelity gas temperature and concentration measurements are currently challenging to conduct.

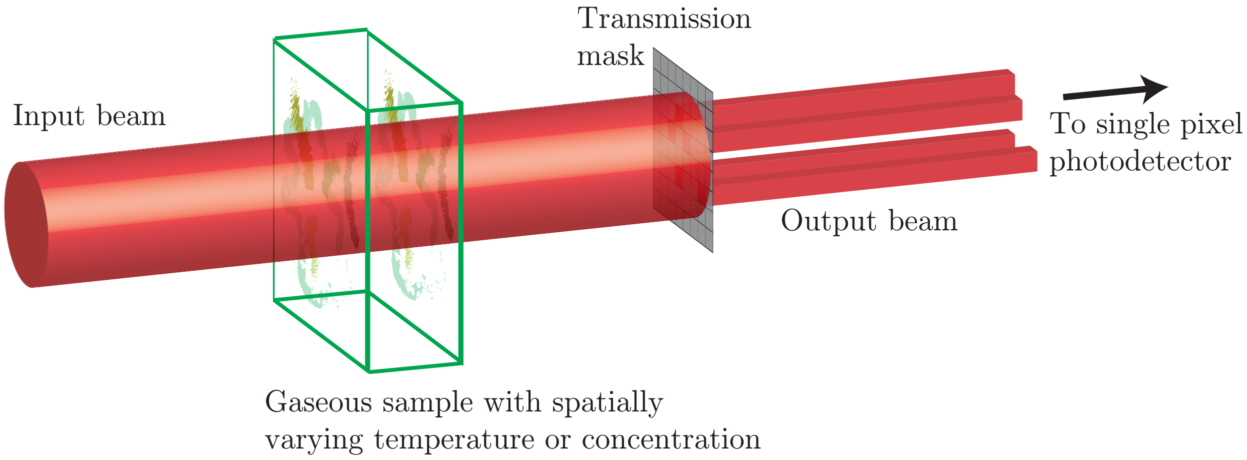

Figure 4.1: Experiment concept. A probe beam travels through a gas with a spatially varying temperature or concentration. Light from this scene is spatially filtered with a number of transmission masks. A measurement is conducted for each transmission mask. The thermodynamic properties of the gas across the transverse extent of the beam are reconstructed using a smashed filter.

4.1 Background

4.1.1 Molecular absorption spectroscopy

Molecules can absorb light at specific frequencies that are resonant with electronic, rotational, and vibrational quantum state transitions. These quantum state transitions are quantized and occur at different but known frequencies for different molecules. Thus, measurements of this absorbed light as a function of frequency are well positioned for molecular identification. Indeed, the applications of molecular absorption spectroscopy are widespread in fields ranging from pharmaceuticals to polymers to planetary sciences [93].

While light from much of the electromagnetic spectrum can be used for spectroscopy, light from the near infrared (NIR) is convenient for many reasons. Organic compounds including alkanes, alcohols, fatty acids, and important climate change compounds (CH_4, CO_2, etc.) have many distinct absorption features or “molecular fingerprints” in this wavelength range [94]. NIR spectroscopy benefits from inexpensive optical components including fibers, lenses, detectors, and more that were developed for the telecommunication industry [95].

Molecular absorption is described by the Beer-Lambert law which states that the amount of light transmitted through a sample is exponentially attenuated according to

$$I(\nu) = I_0(\nu)\exp(-\alpha(\nu)), \tag{4.1}$$

where I is the transmitted intensity, I_0 is the baseline intensity (the intensity of the light before it travels through an absorbing medium), and α is the absorbance. The absorbance is calculated as

$$\alpha(\nu) = -k_\nu L, \tag{4.2}$$

where k_ν is the absorption coefficient and L is the pathlength over which the light excites quantum transitions in the absorbing molecules. For an absorbing species, k_ν has a complicated dependence on temperature, pressure, and mole fraction. The absorption coefficient is calculated as

$$k_\nu = \sum_j \sigma_j(\nu, T, P, \chi) N_j(P, \chi), \tag{4.3}$$

where j represents each of the absorbers, σ_j is the frequency, temperature, pressure, and concentration dependent absorption cross section, and N_j is the pressure and concentration dependent number density of absorbers. Experimentally and theoretically determined values of the components of the absorption cross section for different molecules under varying thermodynamic conditions are stored in databases such as HITRAN 2020 [96] in the form of

$$\sigma_k = \sum_n S_n(T)\phi_n(\nu, T, P, \chi), \tag{4.4}$$

where n represents each of the absorption lines, S_n is the temperature dependent line strength, and ϕ_n is the frequency-, temperature-, pressure-, and mole fraction-dependent, area-normalized line shape function.

Due to the complex dependence of molecular absorption profiles on the mixture and the thermodynamic conditions under which the spectrum is measured, both molecular species and thermodynamic conditions can be quantified by comparing measured spectra to reference spectra. Though such comparisons can be conducted by studying the transmission of several different wavelengths from continuous-wave (CW) lasers through a gas, broadband sources enable simultaneous measurements of several chemical species [97]. This is particularly useful for detecting multiple species, or for measuring absorption from spectra with unexpected features [97]. Multiple broadband sources exist, including: incoherent sources such as lamps, LEDs, and globars; supercontinuum sources; and optical frequency combs (OFCs) [97]. In this thesis, we use a dual frequency comb spectrometer based on OFCs. Compared to the alternative broadband sources, OFCs have low noise and stable spectra [97].

4.1.2 Dual frequency comb spectroscopy

Optical frequency combs (OFCs) were developed to enhance the precision of atomic clocks to enable experiments in fundamental physics [98]. This required measuring atomic transitions at optical frequencies; yet, optical frequencies are a factor of 10^5 faster than the fastest radio or microwave frequencies that are readily countable [98, 99]. Therefore, a stable connection between the radio and microwave domains which could link frequencies between both domains was required [98]. OFCs were developed to fill this role.

OFCs are mode-locked lasers consisting of a regularly spaced comb of optical frequencies which can be referenced to a radio frequency [98]. The frequencies of an OFC are given by the comb equation [100]:

$$f_n = nf_{rep} + f_0, \qquad n = 1, ..., \mathcal{O}(200,000) \tag{4.5}$$

where n is an integer representing the optical longitudinal mode number, f_{rep} is the pulse envelope repetition rate (typically MHz), and f_0 is the carrier-envelop offset frequency given by $f_0 = f_{rep}\Delta\phi/(2\pi)$ for a phase shift $\Delta\phi$. The phase shift $\Delta\phi$ is a consequence of dispersion in the cavity. An OFC can also be understood in the time domain. Pulses are emitted every $1/f_{rep}$

seconds, where $f_{rep} = v_g/L$ for the group velocity of the light v_g and the laser cavity length L [100]. f_{rep} is tunable and is typically sets the spectral resolution of the measurements [100]. Since OFCs are stable, broadband sources with light at many frequencies, they have found applications in many realms of science including spectroscopy.

A challenge with frequency comb spectroscopy is that while individual comb teeth may be attenuated due to absorption of the absorbing species, no detector has a high enough bandwidth to differentiate each comb tooth or the amount of light absorbed at each individual comb tooth. Instead of attempting to measure the comb teeth directly, the comb teeth can be measured against a coherent local oscillator (LO), a second frequency comb whose repetition rate is different than that of the initial frequency comb by Δf_{rep} [101, 102, 103, 104]. This technique, aptly called dual comb spectroscopy, is accomplished using a process called linear optical sampling. In the time domain, linear optical sampling can be understood by considering the pulses emitted from two lasers in the time frame of the LO. In this reference frame, the LO pulse remains stationary but the position of the probe pulse shifts with each pulse since $\Delta f_{rep\neq 0}$. The intensity of this overlap is sampled at each pulse, generating an interferogram, the time domain interference signal. As we will see below, the interferogram is related to the transmission via the magnitude of its inverse Fourier transform. Linear optical sampling can also be understood in the frequency domain as a multiheterodyne sampling technique, where the slight offsets between the comb teeth of the LO and the probe beam induce radio frequency (RF) heterodyne beats. These heterodyne beats are orders of magnitude slower than the optical frequencies and are thus measurable. Taking care to remain within a Nyquist sampling window, the frequencies of these heterodyne beams can be mapped back to optical wavelengths. The amplitudes of a heterodyne beat represent the average amplitude of the two interfering comb teeth, which may differ from the incident amplitudes according to Eq. 4.1 if absorbing molecules are present.

4.1.2.1 Processing the interferograms from dual frequency comb spectroscopy

Commonly, the objective of a gas phase spectroscopic investigation is to identify the chemical mixture and to determine its temperature and pressure. Because changes in these conditions translates to variations in the absorption spectra, this can be accomplished by comparing the spectral features in the measurement to those calculated from a spectral database and then ascribing the conditions associated with the database to the experiment. This process is illustrated schematically in Fig. 4.2.

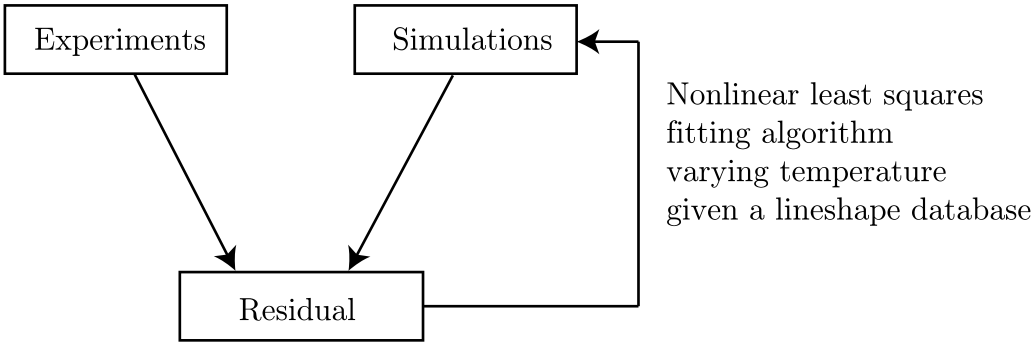

Figure 4.2: The thermodynamic conditions of a system probed with dual comb spectroscopy are determined by comparing experimental results to simulation results using a nonlinear least squares fitting algorithm which calculates absorption spectra from a lineshape database, varying the parameters of interest while fixing the known parameters.

Following the Beer-Lambert Law (Eq. 4.1), molecular absorbance attenuates the transmitted intensity relative to the baseline intensity by a factor of $I/I_0 = \exp(-\alpha(\nu))$. Given the transmission $I(\nu)$ and the baseline $I_0(\nu)$, α can be deduced. Here, we match our experimentally determined $\alpha(\nu)$ to $\alpha(\nu)$ calculated from the reference HITRAN 2008 database [105]. This database is a compilation of theoretically calculated and experimentally gathered molecular absorption features which vary as functions of the molecule type and the thermodynamic conditions. The 2008 version of the database has been shown to deliver accurate results for methane in the 1.6 micron region where the demonstration measurements are performed [106]. We use an optimizer to simulate spectra from this database at specified conditions, iterating until a good match between the experiment and simulation are found. We refer to this process as spectral fitting.

The spectral fitting code uses the lmfit [107] implementation of the Levenberg-Marquardt algorithm to solve a nonlinear least squares minimization problem, minimizing the sum of the squared residual, the difference between the measured and reference spectra. The reference spectra is generated using a simulation code written using HAPI, the HITRAN application programming interface [108]. This simulation code is also used independently in the preliminary numerical investigations to generate spectra which mimic those we would expect to observe in experiments.

To experimentally determine $\alpha(\nu)$, we begin by calculating the transmission, $I(\nu)$, from the magnitude of the inverse Fourier transform of the interferogram IG:

$$I(\nu) = |\mathcal{F}^{-1}\{IG\}|, \tag{4.6}$$

where $\mathcal{F}$ indicates the Fourier transform.

The absorption, a quantity which is closely related to the transmission, is calculated as

$$A(\nu) = -\ln(I(\nu)) = \alpha(\nu) - \ln(I_0). \tag{4.7}$$

The data processing challenge which arises at this step is evident: The precision of our measurement of the baseline I_0 is directly related to the precision of $\alpha(\nu)$ since fluctuations in I could result from either a variation in I_0 or $\alpha(\nu)$. Hence, when comparing $\alpha(\nu)$ from experiments to that from the database, we must remove the effect of the baseline.

To distinguish the absorbance from the baseline, we convert the absorption from the frequency domain to the time domain, calculating the modified free induction decay (m-FID) signal according to [109]

$$a(t) = \mathcal{F}^{-1}\{A(\nu)\} = \underbrace{\mathcal{F}^{-1}\{\alpha(\nu)\}}_{\text{molecular response}} + \underbrace{\mathcal{F}^{-1}\{-\ln(I_0(\nu))\}}_{\text{baseline}}. \tag{4.8}$$

Whereas the contribution to the m-FID signal due to the molecular response spans much of the signal, the contribution to the m-FID signal due to the baseline is localized and prominent at early times. In our fitting scheme, we weight the residuals such that the weight is 0 during the portions of the m-FID signal where both the molecular response and the baseline contribute to the signal and 1 otherwise. In this way, we are able to separate the absorbance trace from the baseline trace. More details on the m-FID signal are provided in Sec. 4.1.2.2.

4.1.2.2 Baseline removal

One challenge which arises when comparing the measured and the reference spectra is that variations in the intensities of the frequency comb lasers known as the baseline translate to dips in the absorption spectra which must be distinguished from absorption features. While software packages like LAB Fit [110] typically use Chebyshev polynomials to estimate the baseline and then subtract it from the transmission spectrum, such strategies require both user input and expertise. Here, we use an alternate technique called time-domain molecular free induction decay (m-FID) fitting to isolate the effect of the baseline from the absorption features [109].

m-FID fitting is based in cepstral analysis [111], a signal processing deconvolution and demultiplication technique which leverages a homomorphic mapping of a convolution to an addition [112]:

$$f * g \mapsto f' + g'. \tag{4.9}$$

In this technique, a convolution is first mapped to a multiplication technique using the Fourier transform convolution theorem, which states that the convolution of two functions in time (frequency) is equivalent to the multiplication of the Fourier transforms of each of the functions in frequency (time) [113]. That is, for functions $a(t)$ and $b(t)$ whose Fourier transforms are given by $\mathcal{F}(a(t)) = A(f)$ and $\mathcal{F}(b(t)) = B(f)$, then $a * b = \mathcal{F}^{-1}\{AB\}$, where $*$ indicates a convolution. Next, the product rule of logarithms is used to map the product of functions within a logarithm to the sum of the logarithm of these functions. The product rule states that $\log_b(MN) = \log_b(M) + \log_b(N)$ for any log base b of functions M and N [114].

The cepstrum (a term coined by Ref. [111] to discriminate the cepstrum from the spectrum) of a signal $f(t)$ is given as [112]

$$C(t) = \mathcal{F}^{-1}\{\ln(\mathcal{F}\{f(t)\})\}. \tag{4.10}$$

If the argument of the natural logarithm is an exponential, multiplicative relationships become additive. Since the Fourier transform is a linear operator, taking the Fourier transform of the sum of these functions is equivalent to summing the Fourier transforms of each of these functions. Cepstral analysis is a natural framework for absorption spectroscopy problems since $\ln[I/I_0] = \ln[\exp(-\alpha(\nu))] = -\alpha(\nu)$.

The m-FID signal is the modified cepstrum of the interferogram:

$$a(t) = \mathcal{F}^{-1}\{-\ln(|\mathcal{F}^{-1}\{IG\}|\}, \tag{4.11}$$

where IG represents the interferogram.

4.1.3 Spatial resolution of absorption spectroscopy

Typically, the lateral spatial resolution of absorption spectroscopy measurements is given by the extent of the probe beam. Moreover, measurements usually lack longitudinal spatial resolution. Consequently, such measurements are commonly referred to as “line-of-sight averaged quantities.” Recent work from our research group has shown how longitudinal temperature distributions can be resolved by solving an inversion problem using a truncated singular value decomposition (TSVD) framework [115, 116]. In this chapter, we develop and demonstrate a means for refining the transverse spatial resolution of spectroscopic measurements conducted with dual frequency combs using a single pixel camera-inspired compressive sensing strategy.

4.1.4 Imaging with optical frequency combs

Since the interferograms measured in DCS are time series of intensity measurements, a camera can serve as a detector. However, as discussed in Sec. 4.1.2, DCS experiments typically use high speed detectors since the OFCs are usually tuned to emit pulses rapidly, and DCS experiments typically wish to measure the interference arising from every set of overlapping pulses. Refs. [117, 118, 119] offer complimentary strategies for bypassing this usual detector requirement, using InGAs or mid-IR cameras with frame rates orders of magnitude slower than detectors to measure interferograms at every pixel: undersampling the interferogram [117, 118], and slowing the pulse rate [119]. In the work of Ref. [117], interferograms generated every second are imaged on 327,680 individual pixels at a rate of 24 Hz. Since the camera operates more slowly than the frequency at which pulses overlap, aliasing results, signifying that spectral features may be corrupted. However, it is still possible to resolve 5 comb teeth in the middle of the spectrum from which the spectral transmittance can be calculated. This imaging system can be tuned to probe a molecular resonance. An analogous technique is adopted by Ref. [118]. Currently, these techniques do not harness the broadband advantages of DCS. In Ref. [119], higher camera frame rates (18,000 frames per second) come at the cost of lower spatial resolution (64 pixels). However, since the lasers are tuned to emit pulses slowly enough for the camera to fully resolve the interferogram, a standard DCS analysis can be conducted. Currently, this strategy does not result in rapid measurements.

Like the works discussed above, the work of Ref. [120] uses a detector array to simultaneously acquire DCS interferograms in a spectroscopy experiment. Fully sampled interferograms are collected and then spectroscopically analyzed. While these interferograms could be processed according to Sec. 4.1.2.1, a convolutional neural network (CNN) is trained to operate directly on the interferogram to reduce the computation time.

An alternative imaging strategy replaces a camera with a single pixel detector, and garners spatial resolution in other ways. One common approach is to perform raster scans: to move the probe beam relative to the sample (or to move the sample relative to the probe beam) to measure subsequent pixels. This is used in a DCS experiment in the THz [121], as well as in a coherent anti-Stokes Raman spectroscopy (CARS) experiment using NIR light [122]. In principle, this raster scanning approach could be adapted to other spectroscopic methods including the absorption spectroscopy discussed in this thesis; yet, gaseous imaging may require translating the optical beam through the sample instead of moving the sample through the beam, a potentially time consuming and nontrivial task.

Since OFCs have thousands of modes (frequency comb teeth), spatially separating these modes can serve as a means for a scanless 2D mapping. This strategy is used in Ref. [123], Mizuno *et al.*, where a virtually imaged phase array (VIPA) [124] generates a mapping between spatial position and OFC modes. At the Fourier plane, this results in a 2D spectrograph which has consists of 14,8000 different illuminated points. A 1-to-1 relationship exists between the spatial position of these points and the OFC modes, so the amplitude and phase modulations encoded at each point are encoded on the corresponding OFC modes. These modulations can be deduced by interfering the probe beam with a reference beam on a single pixel detector and studying the Fourier transform of the resulting interferogram. This technique has facilitated scanless confocal laser microscopy measurements with depth resolution of 14 nm [125] as well as fluoresence lifetime imaging microscopy measurements [126]. Yet, such measurements lose the broadband advantages of DCS, since only several wavelengths probe each pixel.

In an alternate scanless amplitude and phase retrieval scheme, Ref. [127] uses a single pixel sensing experimental configuration to sample the light scattered from a USAF test target for profilometry. This experiment entails passing the probe and local OFCs through a Hadamard transmission mask. The resulting interferograms encode the amplitude and the phase of each spectral component. The amplitudes and phases of certain optical frequencies are reconstructed from the interferograms via Hadamard transform. Though this was demonstrated in the context of profilometry, it could also potentially useful for imaging index of refraction and permitivity without having to invoke the Kramers-Kronig relations.

Our work extends the sensing concepts of these papers, generating spectroscopic images like those from Refs. [117, 118, 119, 121] using scanless techniques inspired by those from Refs. [127]. In particular, we capture and resolve a broadband spectrum using compressive sensing techniques. Compressive sensing techniques enable hyperspectral images which, unlike those from Ref. [120] benefit from an improved signal-to-noise ratio arising from observing the effect of a single pixel in multiple measurements. Though the time resolution and the computation time of these measurements may be slower than that in other works, we anticipate that this advantage will be balanced by the spectral resolution of the technique.

4.1.5 Introduction to compressive sensing

Compressed sensing was introduced in the early 2000s by Candès, Romberg, and Tao[128] and Donoho [129]. The field seeks to solve the following problem: Given fewer measurements than components of a signal, how can the signal be optimally approximated? Mathematically, this question can be expressed as a matrix problem,

$$y = Ax + e, \tag{4.12}$$

where measurements $y \in \mathbb{R}^m$ of a signal $x \in \mathbb{R}^n$ are acquired according to a measurement matrix $A \in \mathbb{R}^{m \times n}$ in the presence of noise, $e \in \mathbb{R}^m$. In the absence of noise and in the case that A is invertible ($\text{rank}(A) = m = n$), this problem can be solved trivially by multiplying y by the inverse of A to determine x. However, such a scenario is rare. More likely is the case where A underdetermined ($\text{rank}(A) < n$) and noise exists. Though x cannot be reconstructed exactly, x can be approximated. A common strategy for approximating x is to use the pseudoinverse of A, $A^+ = (A^T A)^{-1} A^T$, to compute the least squares solution $\hat{x} = A^+ y$ which minimizes the l^2-norm of the residuals. However, applying such a reconstruction strategy to images has been shown to yield poor reconstructions riddled with artifacts [128].

As an alternative strategy for reconstructing the signal x from possibly fewer measurements than elements in x, if we can impose assumptions about the structure of the signal to be recovered on both the measurement and reconstruction processes, then we can enhance the quality of the approximated signal. In particular, if it can be assumed that x is K-sparse (only K of the elements of x are equal to 0) or compressible (only the amplitudes of a few components of x are large relative to the others) in some sparsifying basis ψ, we can measure ensembles of x and then seek sparse solutions for x, those which minimize the l^1-norm of the residuals. In this paradigm, the measurement matrix in Eq. 4.12 is given by $A = \Phi\psi$, where Φ is the projection basis [130, 131]. This underlies compressed sensing. When we solve this problem, we wish to minimize the number of nonzero entries in the reconstructed signal. A natural strategy to consider for performing this optimization would be to minimize the combinatorial l^0 norm (the number of nonzero entries).

However, this strategy is typically not used because the l^0 norm problem is nonconvex and can instead be recast as an l^1 problem and solved using a linear program [130, 132].

Sampling according to a compressed sensing framework is a dimensionality reduction process. For this process to be stable, meaning that the $\mathbb{R}^n$ signal can be recovered from the $\mathbb{R}^m$ measurements, several requirements must be met. Measurements of any pair of signals must be distinct: $Ax_1 \neq Ax_2$ [133]. If x_1 and x_2 are far apart in $\mathbb{R}^n$, then Ax_1 and Ax_2 must also far apart in $\mathbb{R}^m$ [134]. In particular,

$$(1-\delta_k)||x_1 - x_2||_2^2 \leq ||Ax_1 - Ax_2||_2^2 \leq (1+\delta_k)||x_1 - x_2||_2^2, \tag{4.13}$$

where the constant $\delta_k \in (0,1)$ [134]. Known as the restricted isometry property (RIP), this ensures that the measurement matrix preserves distances between all pairs of x [131]. The constant δ_k is calculated as

$$\delta_k = (K-1)\mu, \tag{4.14}$$

where K is the signal sparsity and μ is the mutual coherence of the projection basis Φ and the sparsifying basis ψ [131, 135]. A small μ ensures that each measurement y is influenced by multiple elements of the signal x, and that each element of x contributes to multiple components of y (see Fig. 4.3). In other words, rows (columns) of ϕ cannot be sparsely represented by columns (rows) of ψ [136, 137, 138]. These requirements constrain the possible forms of A.

Two questions which follow are: 1) which measurement matrices are stable, and 2) how large must they be (how many measurements are required)? A finding which has propelled the field of compressive sensing is that, with high probability, only on the order of $M = \mathcal{O}(K\log(N/K))$ [134] measurements of the signal are required if the MN elements of Φ, where $A = \Phi\psi$ are drawn randomly from an independent identically distributed Gaussian probability distribution [134]. A consequence of this finding is that measurements are nonadaptive, meaning that they require no prior knowledge of the signal other than that it can be represented sparsely [136]. Another implication of this finding that a specific knowledge of the sparsifying basis ψ is not required for this type of random compressive sampling–knowledge of the basis only helps calculate the number of

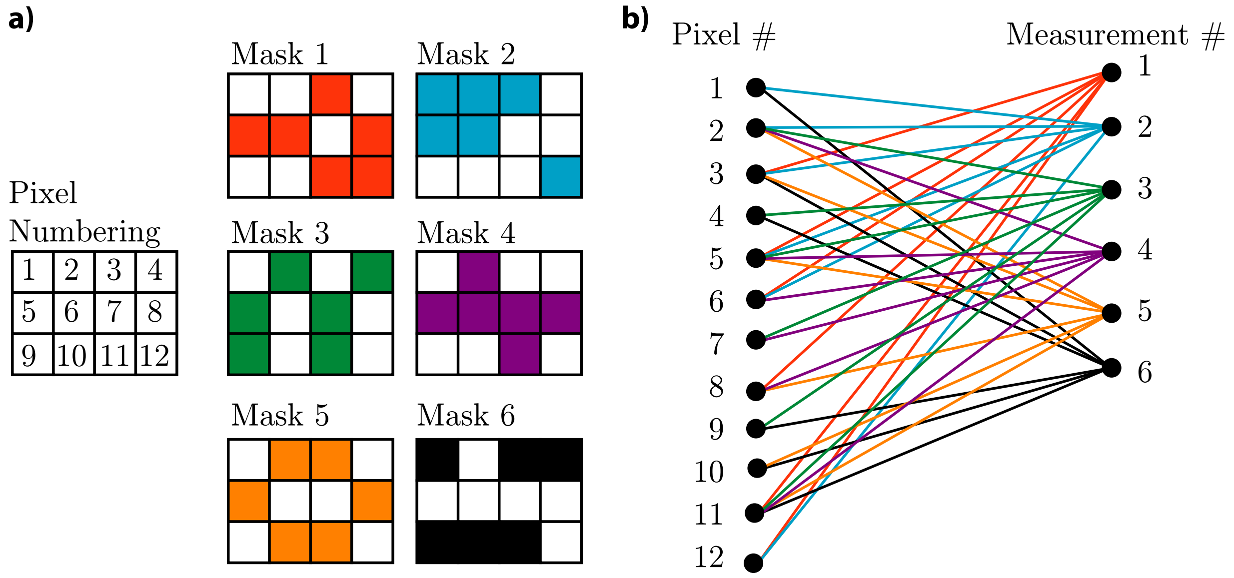

Figure 4.3: Schematic illustrating compressive sensing. a) pixels, numbered according to legend, are sampled with 6 transmission masks, shown at left. For each mask, colored pixels are simultaneously sampled. b) Each pixel contributes to multiple measurements, and each measurement consists of contributions from multiple pixels. The mapping drawn here corresponds to the pixel numbers and the transmission masks in a) and colors correspond to these transmission masks.

required measurements by giving K [139].

4.1.5.1 Comparing sampling rules

Compressed sensing can be interpreted as an alternative sampling rule to the canonical Shannon-Nyquist theorem [140, 141]. The Shannon-Nyquist theorem tells us that to perfectly reconstruct a band-limited, continuous-time signal from its samples, the signal must be sampled at or faster than the Nyquist frequency, $f_s \geq f_{Nyquist} = 2f_{max}$, which is twice the maximum expected frequency of the signal. If a signal is sampled at a slower rate than the Nyquist frequency, aliasing can occur. Aliasing can be readily understood from its description in the frequency domain.

In the frequency domain, "spectral islands" containing the entire spectral content of the signal are repeated at comb teeth whose spacing is set by the inverse of the sampling rate, $\Delta = 1/f_s$ [113]. Because the spectral content is replicated at each of the comb teeth, the information in the vicinity of any comb tooth can be used to reconstruct the signal via inverse Fourier transform. Formally, a bandpass filter with a bandwidth of Δ can be centered on a comb tooth to isolate the spectral information imprinted around the comb tooth, extracting the frequency content closest to that comb tooth. If the comb teeth are spaced far enough apart that this bandpass filter extracts the entirety of the spectral island located on a single comb tooth and no information from any other spectral islands ($\Delta \geq f_{Nyquist}$), then the signal can be perfectly reconstructed. However, if the comb teeth are too close together meaning that the signal was sampled at a rate $2f_s < f_{Nyquist}$, spectral islands might overlap. In this case, the bandpass filter could possibly extract the high frequencies of a neighboring comb spectral island and interpret them as low frequencies. Likewise, low frequencies from a different spectral island might be interpreted as high frequencies. This is known as aliasing [113].

To avoid aliasing, signals must be sampled faster than the Nyquist frequency. This can be both expensive and technically challenging, especially with optical frequencies. For example, as discussed in Sec. 4.1.2, even detectors of the highest quality operate orders of magnitude too slowly to resolve optical frequencies. To bypass this technological constraint in our optical frequency comb-based spectroscopy, we employ an elegant linear optical sampling detection scheme which maps optical frequencies to measurable radio frequencies [101].

If a signal is to be resolved spatially instead of (or as well as) temporally, the Nyquist-Shannon sampling theorem tells us that its spatial frequencies must also be sampled at frequencies larger than twice the maximum spatial frequency. In the context of photography, this dictates the pixel size. If we wish to acquire an image of a fixed size but require small pixels to achieve the intended resolution, an array with millions of detectors and analog-to-digital converters could be required. Though cameras commonly have such detector arrays, fabricating such arrays can become prohibitively expensive if time resolution is important or for wavelengths different from the visible wavelengths. As an example, each detector we use in this chapter (Thorlabs, PDA10cf) costs approximately \$500, and the supporting data acquisition systems for each detector cost on the order of \$10,000. Particularly in R&D settings where funding can be limited, increasing the number of detectors to gain spatial resolution may not be feasible. In such applications, single pixel-based compressive sensing techniques are an inexpensive alternative [142].

4.1.6 Single pixel camera

The single pixel camera was introduced by researchers at Rice University in 2006 [143]. As its name implies, this imaging modality replaces an array of detectors with a sole detector. To generate images with spatial resolution, programmable transmission mask are placed between the scene to be imaged and the detector. Intensity measurements are recorded for each transmission mask. Then, an l^1 optimization scheme is used to reconstruct the image from the measurements and the transmission mask. Formally, each measurement corresponds to the inner product of the vectorized image and a row of the measurement matrix. With an ample number of measurements and under the assumptions that the scene can be represented sparsely in some basis incoherent with the projection basis as discussed above, the image can be reconstructed. Note that single pixel imaging is closely related to ghost imaging, a technique wherein a scene is imaged with structured light instead of structured detection [144, 145].

Even in such cases as visible wavelength photography where detector arrays are available and affordable, using such arrays to sample scenes at the Nyquist-Shannon limit may not be necessary and may generate more information than is strictly necessary to represent the scene. For example, photographs recorded by typical cameras consist of pixel-by-pixel measurements, but these images can be compressed using methods based on the discrete cosine transform or wavelet transform according to the JPEG standard to 2%-10% of their original size without compromising their apparent quality [146]. To the human eye, a JPEG image may have a strong resemblance to the uncompressed image, but it can be stored with far less data. A compressed sensing approach to photography bypasses the initial stage which acquires information for each pixel, and instead collects data in the sparse basis. In doing so, little redundant information is collected just to be discarded during compression.

Though the single pixel camera was first demonstrated in photography [143], the principle has been adapted in many applications requiring spatial resolution. For example, single pixel imaging finds uses in scenarios where detector arrays are unavailable, as in experiments with THz beams [147]. In other regions of the electromagnetic spectrum, detector arrays may exist, but using them to image a scene can be challenging due to the small power incident on each detector, as this can lead to nonlinear detector behaviors and result in measurements with low signal to noise ratios. Single pixel imaging resolves this problem because the transmission masks used in single pixel imaging allow for light from many pixels to be simultaneously incident on the detector for any given measurement. This efficiency advantage is harnessed in applications ranging from imaging neutron beams [148] to microscopy [149]. Single pixel imaging techniques are also commonly used in time of flight (ToF) measurements where detector arrays exist, but only with limited numbers of pixels [150].

Single pixel imaging is commonly advertised to have three benefits relative to other techniques which yield spatially resolved images such as rastering: its measurements are 1) universal, 2) progressive, and 3) democratic [151]. Universality refers to the quality that the measurements do not depend on the basis in which the image is compressible, ψ, since Φ is random. The consequence of universality is that measurements require no assumptions about the signal being observed, other than that it can be represented sparsely in some basis. This is to say, measurements in this framework are nonadaptive and can be collected with no prior information about the signal [129, 130]. The progressive nature of measurements in this framework describes how adding subsequent measurements yields improved signal reconstructions [151]. The democratic quality is closely related: since every measurement is equally weighted, eliminating any single measurement from the reconstruction process has the same effect on the reconstructed signal [151].

As we will see in this Chapter, the single pixel framework can be applied to measurements which normally have no spatial resolution across the transverse extent of the probe beam. Introducing the programmable transmission mask enables measurements with spatial resolution set by the transmission mask pixel size.

4.1.7 Smashed Filter

In many cases, compressive measurements are reconstructed to infer qualities of the scene. The smashed filter provides a conceptual framework for operating directly on compressed images for such inference problems including classification, recognition, detection, filtering, and estimation problems without first reconstructing the scene [139, 151]. The elegance of using a smashed filter approach for such problems is that because no superfluous scene reconstruction is necessary, the approach is streamlined. Compressive sampling moves the imaging burden from the experiments to the computation. Simplifying the computation, then, results in highly efficient imaging processes.

The smashed filter is a generalization of a matched filter to the compressed measurement basis [151]–a dimensionally reduced matched filter. To describe the smashed filter, we begin by discussing the matched filter. Then, we translate the matched filter to the compressed measurement basis. Matched filters operate by comparing a signal to a bank of test signals which are different versions of time-reversed complex conjugates of template signals [152]. The matched filter is the optimal maximum likelihood classifier when the observed signal belongs to a known set that may have a shift [151]:

$$y(t;\theta) = s_i(t-\theta), \tag{4.15}$$

where s_i is one of the possible signals and θ is a K-dimensional parameter. Consequently, the matched filter is commonly used in radar applications to detect if an object is present, and if so, to determine its distance from the emitter/detector node as well as its relative speed to the emitter/detector node [152]. If no reflecting object is present, the detected signal is merely noise. However, if an object reflects the emitted waveform, the duration between when the pulse was emitted and when its reflection is received encodes the positioning of the object. The dilation of the reflected waveform corresponds to the Doppler shift it may have undergone and can reveal the relative velocity between the emitter/detector node and the reflecting object. The matched filter performs these operations by comparing the time varying signal from the detector to a bank of filters, each taking the form of the time reversed complex conjugate of a dilated copy of the initial waveform. Hypothesis testing is then used to "match" the filter which best overlaps with the reflected waveform, ascribing the qualities of the filter to the qualities of the reflected signal to classify the position and speed of the reflecting object [152]. In the smashed filter, this filtering process occurs in the compressed measurement basis [151].

The smashed filter is a nearest-neighbor classification problem. The problem formulation we present here closely follows that from Ref. [151]. To begin, we rewrite Eq. 4.12 so that the measurement matrix acts on the noise as

$$y = A(x + w), \tag{4.16}$$

such that $Aw = e$. We assume that w is additive white Gaussian noise (AWGN) with variance σ. Further, we assume that x belongs to one of the P classes of signals $\mathcal{C}_i$, $i = 1, ..., P$. This means that x can be written $x = f_i(\theta_i)$, where f_i is a function which maps its parameters $\theta_i \in \Theta$ to $\mathbb{R}^N$. For each class $\mathcal{C}_i$ we write a hypothesis $\mathcal{H}_i$ that x belongs to $\mathcal{C}_i$. Then, we write the likelihood that y belongs to each $\mathcal{H}_i$ under the parameters θ as

$$p(y|\theta, \mathcal{H}_i) = \frac{1}{(2\pi\sigma)^{M/2}} \exp\left[-\frac{1}{2\sigma}||y - Af(\theta)||_2^2\right]. \tag{4.17}$$

Given this likelihood function, the maximum likelihood estimate (MLE) of $\hat{\theta}_i$ is given by

$$\hat{\theta}_i = \underset{\theta \in \Theta_i}{\operatorname{argmin}} \; ||y - Af(\theta)||_2^2. \tag{4.18}$$

Solving this least squares problem presented in the compressed measurement basis constitutes the smashed filter.

The smashed filter approach can be used if the signal is sensed according to the RIP, adhering to Eq. 4.13 [153, 151]. This is because the RIP ensures that the underlying structure of the data is preserved, meaning that projecting the signal into onto the sensing basis does not dilate or shrink the relative distances between any pair of signal elements. If the structure of the data is not corrupted by the sensing process, its characteristics can be deduced–even if the data is not readily interpretable in this sensing basis.

Compressive sensing modalities are attractive because they simplify the burden of the experiments. This comes at the cost of added computation for reconstructing the signal from the measurements. But if reconstruction is not required and a smashed filter approach can be adopted, both the experiments and the computation can be simplified. This is particularly useful for applications such as analyzing video surveillance footage, where rapid analysis of high resolution footage can be required [154, 155]. In this example, an additional benefit associated with the smashed filter is that privacy can be maintained when visually unrecognizable image samples are collected and image reconstruction is not required [156].

The smashed filter finds uses in many other applications in which large streams of data require interpretation. For example, the smashed filter facilitates monitoring distributed sensor networks, like those used to detect damage in structures [157]. Such sensors measure the acceleration of structures at different locations in response to excitement at a single frequency. Reconstruction of data collected using compressive sensing can be conducted to recreate these acceleration signals, but this is not required, as damage can be detected from the compressed measurements themselves using a smashed filter [157].

4.1.8 Compressive sensing and absorption spectroscopy

As discussed in Sec. 4.1.5, compressive sensing techniques can be used when the signal being sampled can be represented sparsely in some basis. Absorption spectroscopy measurements lend themselves well to compressive sensing since absorption features, particularly when measured at atmospheric pressures, are quantized as well as narrow and sparse in frequency relative to broadband source frequency ranges. Yet, laser sources which emit light spanning these sparse spectra are somewhat limited. This is particularly problematic for making absorption cross section databases from which systems at high temperatures and pressures like planetary atmospheres [158, 159] and combustion systems [160] can be studied. At high pressures, absorption features are broadened by pressure induced collisional broadening and line mixing effects [161, 162], and the sizes (the frequencies spanned) of absorption features grow with increased temperature and pressure relative to the fixed spectral window of the measurement. Therefore, if a compressive sensing approach is to be adopted under these relevant thermodynamic conditions, the source must be broadband.

In their 2018 paper, Amiot *et al.* propose and demonstrate a compressive sensing framework for spectroscopic measurements of methane which harnesses the random spectral intensity variability arising from an optical instability of a broadband random light source, a supercontinuum laser [163]. Light from this source is split into two branches, a reference arm with a spectrometer, and a test arm with the gas sample. Using a numerical differential detection scheme which resembles balanced detection, Amiot *et al.* piece together the absorption spectrum of the gas across a spectral region spanning from 1610 nm to 1670 nm with subnanometer resolution. The spectrum of the incident light fluctuates on a time scale faster than the inverse of the measurement rate, 100kHz. With 0.2 seconds of data (20,000 measurements), the absorption spectrum of methane can be resolved to within the precision at which the reference arm measures the incident spectrum. This technique offers a means for using broadband random sources for spectroscopic measurements.

If, instead of possessing a sparse spectrum a scene has a sparse distribution of molecules which can be spectroscopically identified, a single pixel imaging strategy can be employed. For example, Graham *et al.* sense methane by comparing absorption at lines which are and are not sensitive to methane [164]. In this strategy, a diode laser tuned to a methane absorption line at 1651 nm is used to illuminate a scene with methane captured at several different concentrations in sample cells. The light is then imaged onto a DMD which is programed to display a series of transmission masks. Light which passes through these transmission masks is collected on a photodetector. Variations in the intensity of the light transmitted through a mask compared to the light transmitted through the negative of the mask are used to reconstruct the image. While this enables methane detection, spectroscopic measurements at a single wavelength are insufficient for quantifying the thermodynamic qualities of the gas. Inspired by this demonstration, we seek to develop a spectroscopic compressive sensing strategy which can accommodate incident light at more frequencies.

In this chapter, we use compressive sensing to yield spatial resolution across the transverse extent of a probe beam, adding resolution across a typically neglected dimension. This is enabled by our broadband ($\approx$600 cm^{-1}), high resolution (0.0066 cm^{-1}) dual frequency comb spectrometer.

4.1.9 Applications of the smashed filter in absorption spectroscopy

Traditional spectrometers employ a dispersive element which maps different wavelengths to different and known locations in space. A single dispersive element typically provides angular dispersion along one direction, mapping wavelengths along a single lateral coordinate. Echelle (French for *ladder*) spectrometers use two dispersive elements to map wavelengths along two orthogonal directions [165]. Such spectrometers yield high resolution measurements for a larger bandwidth than is possible given a single dispersive element and detector of a fixed size [166] and are commonly implemented in telescopes [167, 168, 169]. In modern Echelle spectrometers, detector arrays measure spectrographs, images of the intensity of light at each position along a two dimensional scene. In conference proceedings, Ref.[170] suggests that a smashed filter analysis of echelle spectrographs may facilitate spectroscopic measurements from this style of spectrometer. In this work, the detector array is replaced with a DMD which transmits light to a single pixel detector. Though the details of the experiment, analysis, and results are unclear, the function of the smashed filter appears to be to deduce the presence of various gasses directly from the compressive measurements without first reconstructing the spectrograph.

4.2 Applying a compressive sensing framework to dual frequency comb spectroscopy to generate hyperspectral images

Our spatially resolved, single pixel, dual frequency comb spectrometer consists of two modules: a simulation and an experiment. In the sections which follow, we discuss the development of both modules. We begin with a discussion of the computational framework. Then, we detail the experiment. Finally, we present our experimental results.

4.3 Simulating hyperspectral imaging using compressive sensing and dual frequency comb spectroscopy

Applying the smashed filter to dual frequency comb measurements results in a multispectral fitting problem in which the objective is to determine the thermodynamic conditions at each pixel, for each absorbing molecule. A flow chart in Fig. 4.4 illustrates the process. Given a measurement matrix A, a list of measurements corresponding to A, and a reference spectroscopic database, we seek to determine the temperature at each pixel. We accomplish this with a single nonlinear least squares fit written using the minimize function from lmfit [107]. The output is a list of thermodynamic conditions at each pixel.

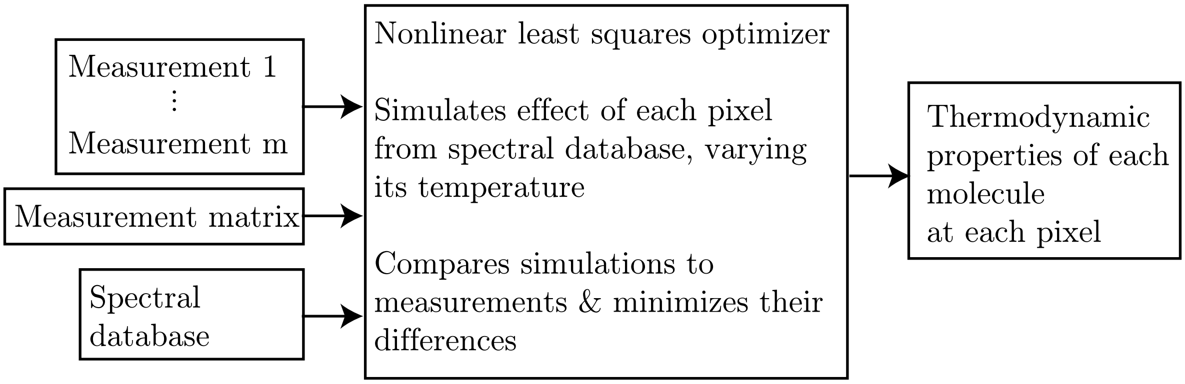

Figure 4.4: An overview of the smashed filter as applied to hyperspectral imaging via dual frequency comb spectroscopy.

Within the smashed filter, measurements are compared to simulated measurements. These simulated measurements are generated according to Algorithm 1, using the measurement matrix to select the relevant pixels for each measurement. Note that step 2 of the algorithm will be experimentally validated in Sec. 4.4.1 The thermodynamic conditions of each pixel are updated at every iteration of the optimizer to minimize the total residual calculated as the sum of the absolute value of the differences between each measurement and its corresponding simulated measurement.

To test our implementation of the smashed filter, we conduct an *in silico* experiment wherein we calculate a 4x5 pixel scene which mimics the experiment we conduct later in Sec. 4.4.2. In this

Algorithm 1: Simulating cepstra from database

```
(1) For each of the $i$ pixels, calculate baseline-free absorption coefficient from a
    spectroscopic database: $k_{\nu,i}(\nu)$
(2) Calculate weighted baseline-free absorbance from the baseline-free
    absorption coefficient and pathlength: $\alpha_{\text{no BL}}(\nu) = \sum_{j=1}^{i} w_j k_{\nu,j}(\nu) L_j$
(3) Calculate transmission from baseline-free absorbance:
    $I_{\text{no BL}}(\nu) = \exp\{-\alpha_{\text{no BL}}(\nu)\}$
(4) Calculate transmission using simulated baseline,
    $I_0(\nu)$: $I(\nu) = I_0(\nu)\exp\{-\alpha_{\text{no BL}}(\nu)\}$
(5) Calculate absorbance from transmission with baseline, adding random noise
    according to standard Normal distribution scaled to specified power $P$:
    $\alpha(\nu) = -\ln(I(\nu)) + P \times \mathcal{N}(\mu = 0, \sigma = 1)$
(6) Calculate noisy, baseline-added m-FID signal from absorbance: $a(t) = \mathcal{F}^{-1}\{\alpha(\nu)\}$
```

scene, the temperature and pressure of every pixel are $T = 298$ K and $P = 1$ atm, and some pixels interrogate $L = 10$ cm of a 5% methane, 95% air mixture. For the purposes of this demonstration, we use a weighting factor of $w_j = 1$ in step 2 of Algorithm 1 for both simulating and fitting the data in this numerical experiment. We use the HITRAN 2016 database [94] to simulate the absorption coefficient k of these pixels from 1625 nm-1660 nm. Since the optical bandwidth is situated in a water window where air and the water vapor within the air absorbs only tiny fractions of the light, the pixels which do not probe the methane are given an absorption coefficient of 0. The test matrix we use measures 10 randomly chosen pixels per measurement. Following Algorithm 1, we calculate the baseline-free absorbance, the transmission, the transmission using a simulated baseline, the absorbance with the simulated baseline and absorbance noise of 0.001, and finally the m-FID signal. We call these simulated m-FID signals our simulated data. Next, we input the simulated data into the smashed filter to solve for the path length of methane while holding the temperature, pressure, and mole fraction constant. Our results are shown in Fig. 4.5. We find excellent agreement between the calculated and recovered methane path lengths. This indicates that the smashed filter architecture functions well, and suggests that the smashed filter will work with experiments.

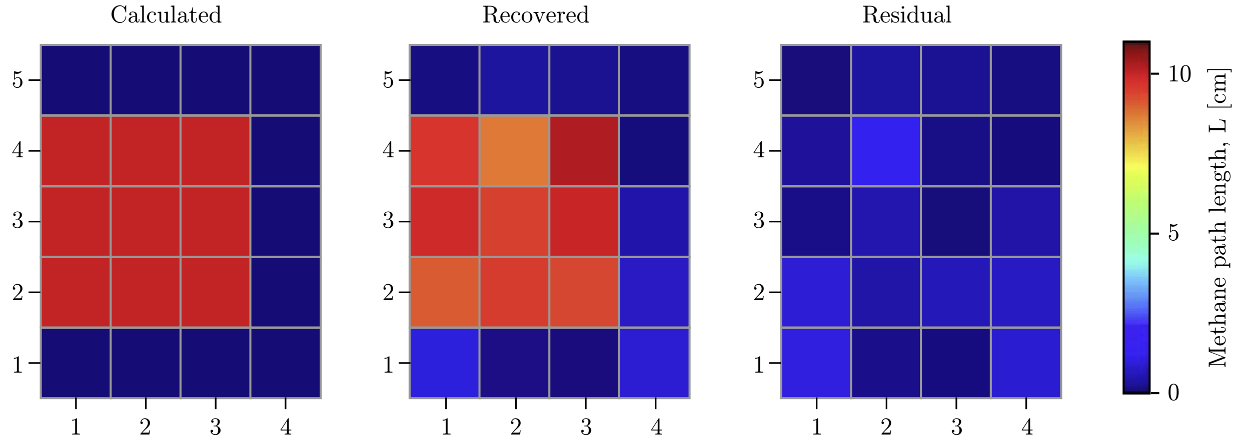

Figure 4.5: Methane path lengths for the *in silico* experiment described in the text that are a) modeled and then b) recovered. c) The difference between the calculated and recovered path lengths.

4.4 Experiments

Our experimental demonstration of hyperspectral imaging using dual frequency comb spectroscopy and compressive sensing uses a digital micromirror device (DMD, Texas Instruments DLP4500NIR) to impart spatial structure on the detection system. In this experiment, the probe beam passes through the test scene, and then it impinges on the DMD. The DMD diffracts light from pixels selected according to a pre-calculated transmission mask towards a photodetector (Thorlabs, PDA 10cf). Interferograms collected at the photodetector are phase corrected and averaged for 5 minutes. In these experiments, the test scene comprises a 10 cm long test cell filled with 5% methane and 95% air at a pressure of 1 atm. This test cell is oriented parallel to the optical axis and is offset from the optical axis such that only a portion of the light incident on the DMD passes through the test cell, and the remaining light incident on the DMD does not pass through the test cell. Fig. 4.6 shows a schematic of the experimental setup.

We tailor the operation of the dual frequency comb system such that light is emitted between 1620-1650 nm. In this spectral region, methane displays strong absorption features, while air (and particularly water vapor in the air) absorbs only trace amounts of light. In effect, the air is transparent to the light, and the only absorption arises due to the methane. This provides a convenient spectral range within which to test our hyperspectral imaging framework, since only one absorbing species need be considered. Nonetheless, we note that our technique can be expanded to work in systems with more than one absorbing species.

The dual frequency comb spectrometer we use is described in detail in Refs. [171, 172, 173, 174]. In broad strokes, this spectrometer consists of two frequency combs, each of which have linear cavities with polarization-maintaining fiber and a semiconductor saturable absorber mirror (SESAM) for mode locking [174]. Pulses emitted from the laser cavities are broadened and amplified in highly nonlinear fiber (HNLF). The f_{ceo} is stabilized using light wavelength doubled by a periodically poled lithium niobate waveguide (PPLN). The frequency combs are further stabilized by controlling a heterodyne beat between a reference laser at 1600 nm and one tooth of each of the

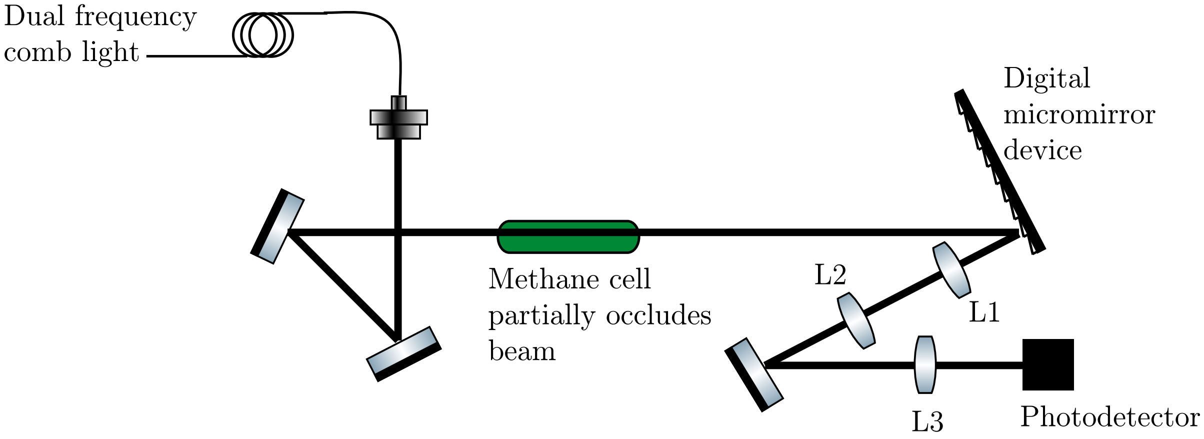

Figure 4.6: Hyperspectral imaging experimental setup. Light from a dual frequency comb spectroscopy (DCS) system is collimated into a large beam. A portion of this beam passes through a methane cell oriented to partially occlude the beam. The light then impinges on a digital micromirror device (DMD). The diffracted order corresponding to the blazed angle of the DMD is magnified using lenses L1 and L2 to decrease its angular dispersion. This light is then focused by lens L3 onto a photodetector.

frequency combs.

The DMD is oriented at approximately 27° relative to the incident optical axis such that the central wavelength, $\lambda_c = 1630$ nm travels along the optical axis upon diffracting from the DMD at the blazed angle [175]. Because the dual frequency comb light is broadband and the DMD behaves as a grating [175], the diffracted light has angular dispersion along the direction of the grating vector, along the lateral coordinate of the DMD [176]. If this angular dispersion resulting from the DMD was left untreated, the broadband light incident on a detector would constitute a classical spectrometer, wherein light of different wavelengths would be spatially separated. When measured on a small photodetector such as the Thorlabs PDA 10cf with a 0.2 mm^2 active area used here, a mapping would exist between the lateral coordinate on the DMD and the optical spectrum. Since we wish to measure a broadband spectrum at each pixel on the DMD, the angular dispersion needs to either be compensated for or mitigated within the spectral bandwidth used in the spectroscopic fits (1625-1660 nm).

A multitude of strategies exist for compensating for angular dispersion. One possible strategy which would be viable in the present experiment would be to use a Martinez-style pulse stretcher [177, 178], implemented with the DMD on one image plane and a grating or potentially a second DMD [179] at the other image plane of a telescope. However, instead of compensating for the angular dispersion in this traditional manner, we opted for an alternative, more efficient angular dispersion mitigation strategy wherein we reduce the angular dispersion by implementing a telescope to magnify the beam. This strategy can be understood from a geometric optics perspective. When a telescope magnifies a beam by a factor of $\mathcal{M}$, the angular divergence of the beam is magnified by a factor of $1/\mathcal{M}$. Here, we use a telescope to expand the beam by a factor of $\mathcal{M} = f_2/f_1 = 2.6$, where $f_1 = 75$ mm and $f_2 = 200$ mm are the focal lengths of two Thorlabs c-coated achromatic lenses. This reduces the angular divergence of the beam to $f_1/f_2 = 38\%$ of that of the diffracted beam. We place the photodetector at the Fourier plane of a third lens (Thorlabs c-coated achromatic lens, focal length $f_3 = 75$ mm). Since lenses map monochromatic plane waves at different angles to different positions at the Fourier plane, this strategy increases the detectable bandwidth on a photodetector of a fixed size by a factor of roughly f_1/f_2.

In this experiment, we wish to demonstrate that we can recover thermodynamic conditions using broadband spectroscopy, without spectral to spatial mapping. Therefore, it is important to verify that the optical bandwidth remains constant across the lateral coordinate of the DMD (the DMD induces no angular dispersion along the vertical coordinate since the grating vector is purely in the lateral plane). To ensure that the light diffracted from either side of the DMD has the same optical bandwidth, we program the DMD to diffract light from a series of vertical slits 30 pixels (0.324 mm) wide. Results from this exercise are shown in Fig. 4.7. Although the transmission spectra have different magnitudes owing to the relative differences in illumination intensity, both span the optical bandwidth used in the spectroscopic fits (1625-1660 nm) with sufficient transmission values for spectroscopic fitting.

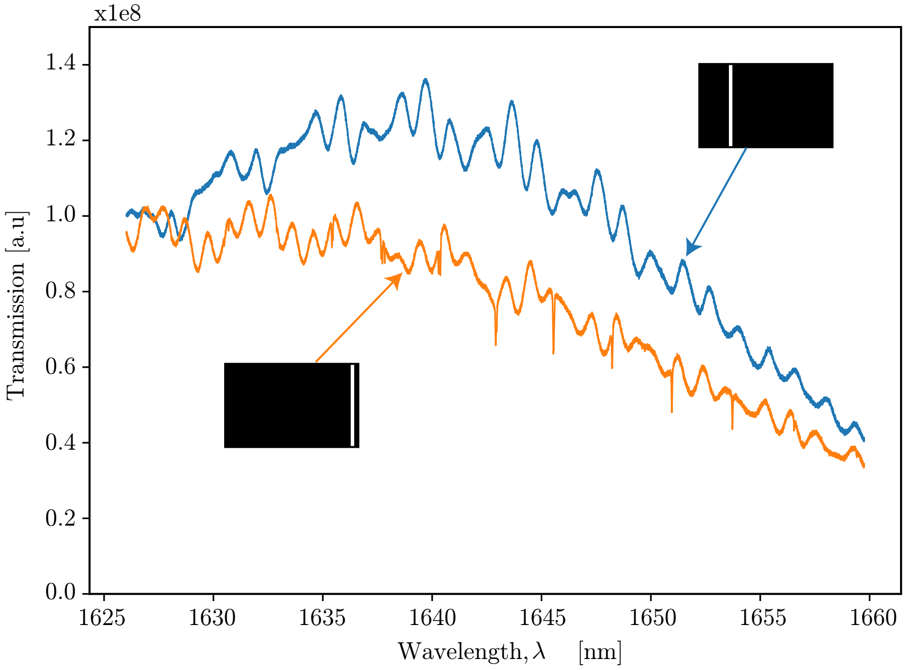

Figure 4.7: Transmission spectra for light diffracted from 0.324 mm wide vertical strips on the DMD towards the photodetector, by way of the telescope and focusing lens. Insets show the DMD schematically; black and white indicate the portion of the DMD that diffracts light away and towards from the photodetector, respectively. The orange transmission spectrum corresponding the strip on the right side of the DMD shows evidence of methane absorption whereas the blue transmission spectrum corresponding to the strip on the left side of the DMD does not, since the methane cell is placed ahead of the DMD only on the right side.

4.4.0.1 Impact of the digital micromirror device on interferograms

The mirrors of the digital micromirror device (DMD) flicker at a timescale given by the exposure frame period of the DMD, T_e. Each such movement generates a burst within the interferogram which is comparable to the centerburst in magnitude. When T_e is not an integer fraction of the duration of the interferogram, $T_I = 1/(\Delta f_{rep})$, these bursts resulting from the DMD flicker appear to translate through the center burst.

Because T_I is on the order of ms and it is customary to average minutes of interferograms to enhance the signal to noise ratio, field programmable gate arrays (FPGAs) embedded in the data acquisition system (DAQ) are programmed to sum sets of 50 (or more) interferograms. This reduces the size of the data stream in a manner which has a minimal impact on the fidelity of the data due to the stability of the laser system.

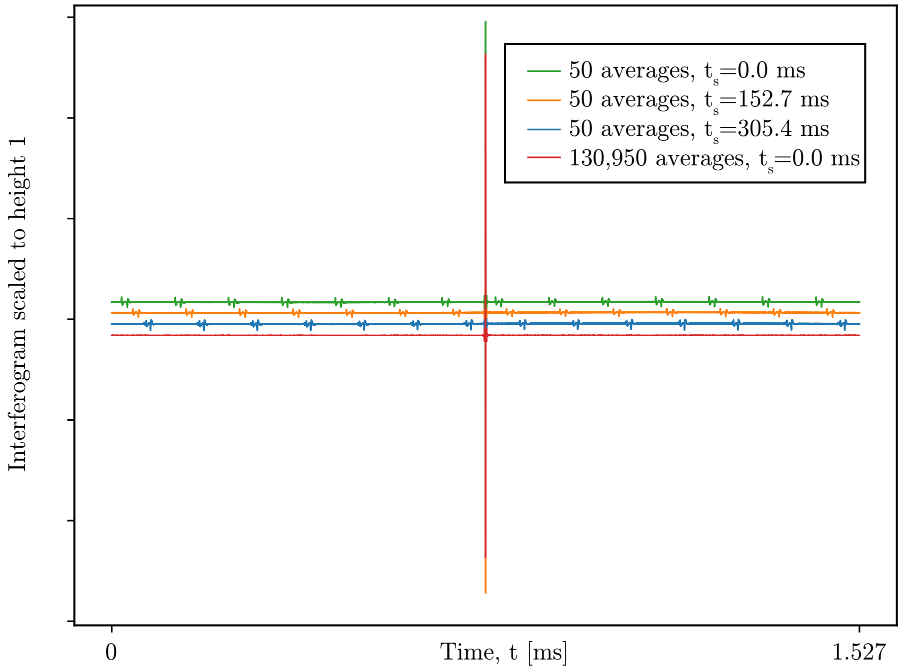

Figure 4.8: Interferograms for different averaging times, with averaging started at t_s. Averaging 50 interferograms takes 76.35 ms. Interferograms are offset vertically for clarity. Digital micromirror device exposure frame period $T_e = 3$ ms.

In Fig. 4.8, we plot four averaged interferograms. Three of these averaged interferograms are the averages of 50 interferograms started at times t_s corresponding to the times of the 0th, 100th, and 200th interferograms. The fourth is the average of 130,950 interferograms. In the interferograms with 50 averages, the movement of the bursts resulting from the DMD flicker relative to the center burst is evident. The apparent size of these bursts is small. This is because the bursts are isolated in time and they translate between subsequent interferograms. The overlap of the bursts with each other as a function of time is small relative to the overlap of the center burst in subsequent interferograms since the position of the center burst does not change. When 130,950 interferograms (approximately 200 seconds of experimental time) are averaged, little evidence from the bursts resulting from the DMD flicker remains, and these averaged interferograms can be treated normally. While we did not characterize how interferogram averaging time affects the noise of the fitted spectrum, we expect that this flickering behavior of the DMD may limit the ultimate noise floor.

4.4.1 Validating smashed filter approach

In this section, we experimentally deduce how the m-FID signal can be constructed for an arbitrary transmission mask. This work experimentally validates the assumption of step 2 of Algorithm 1, that the absorbance of a measurement is given by the sum of the absorbance of each pixels. We conduct two experiments using the same setup, shown schematically in Fig. 4.6. In the text which follows, we will refer to these two regions as the "air only" and "methane and air" regions of the DMD, respectively. The DMD is segmented into an array of 7x7 rectangular superpixels, each measuring 130 pixels by 162 pixels. A schematic of the DMD superpixels and the orientation of the methane cell relative to the DMD are shown in Fig. 4.9a. Note that the superpixel edge with fewer pixels is indeed longer than the edge with more pixels due to the DMD pixel orientation and numbering scheme.

4.4.1.1 Characterizing the experimental system: using the DMD to modulate the beam to measure known methane path lengths

In this set of experiments, we verify that the the dual frequency comb system functions with the DMD by conducting two different measurements. In these experiments, we directing pixels from either the air only region of the DMD or the methane and air region of the DMD to the photodetector. These measurements are averaged for 200 seconds. The results from this experiment are shown in Fig. 4.9b-d. As anticipated, the absorbance trace for the experiment corresponding to the air only region of the DMD shows no evidence of methane (Fig. 4.9b and c), while that for the experiment corresponding to the methane and air region of the DMD shows strong evidence of methane (Fig. 4.9b and d). The fitted path lengths for the air only and the air and methane experiments are $L = 0.028 \pm 0.003$ cm and $L = 9.544 \pm 0.003$ cm, respectively. Though we expected path lengths of $L = 0$ cm and $L = 10$ cm for these two test cases, a closer examination of the absorbance residual indicates that the fits come to within the absorbance noise

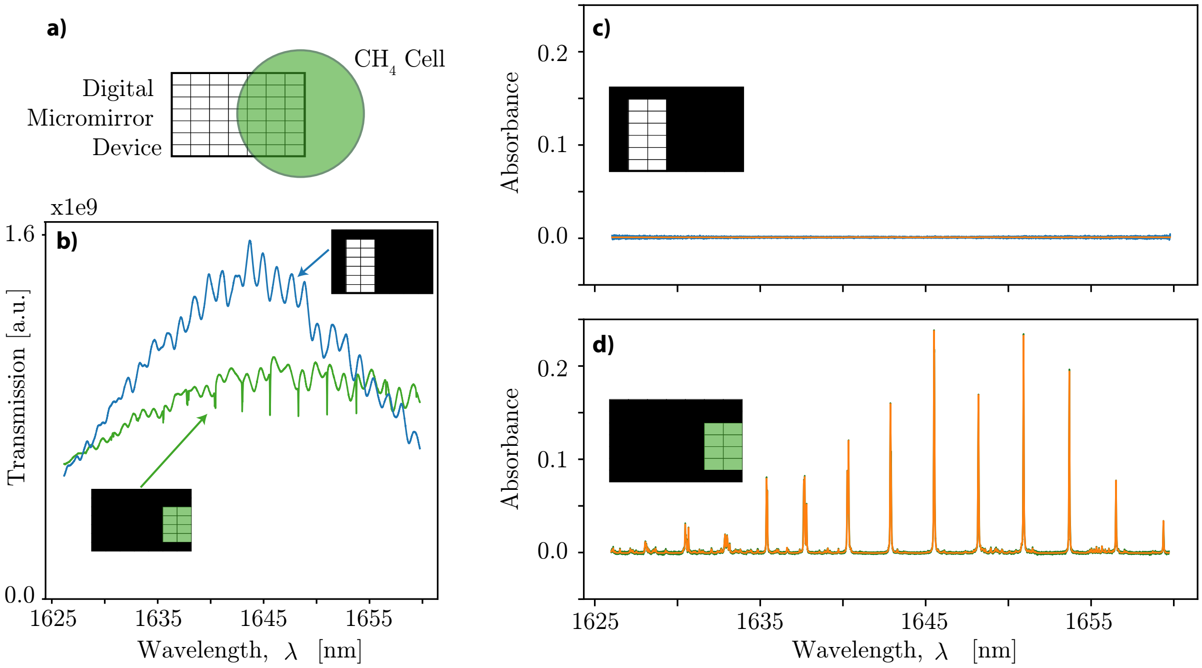

Figure 4.9: a) A methane cell partially occludes a digital micromirror device (DMD) which is segmented to have a 7x7 superpixel grid. b) Transmission spectra for groups of pixels selected such that the light incident on the pixels either passes fully through the methane cell (green) or does not pass at all through the methane cell (blue). Orange lines correspond to spectroscopic fits which find the methane path length to be 0.028 ± 0.003 m and 9.544 ± 0.003 m for c) and d), respectively. Insets illustrate the portions of the DMD sampled to generate the spectra. Absorbance spectra for light which does not traverse (c) and does traverse (d) the methane cell.

level of 0.02. The results of this test indicate that methane path lengths can be well estimated in a simple experimental configuration.

4.4.1.2 Experimentally deducing an absorption spectroscopy model

In this set of experiments, we validate the smashed filter approach. We study the light diffracted from 5 of the superpixels, 2 (3) which diffract light which does (does not) pass through the methane cell. We average 5 minutes of phase corrected interferograms for each pixel and for every combination of two pixels. We perform a spectroscopic fit fixing the methane temperature, pressure, mole fraction while floating the methane path length. The results are shown in Fig. 4.10.

The fitted path lengths for the measurements consisting of the single pixels come to within

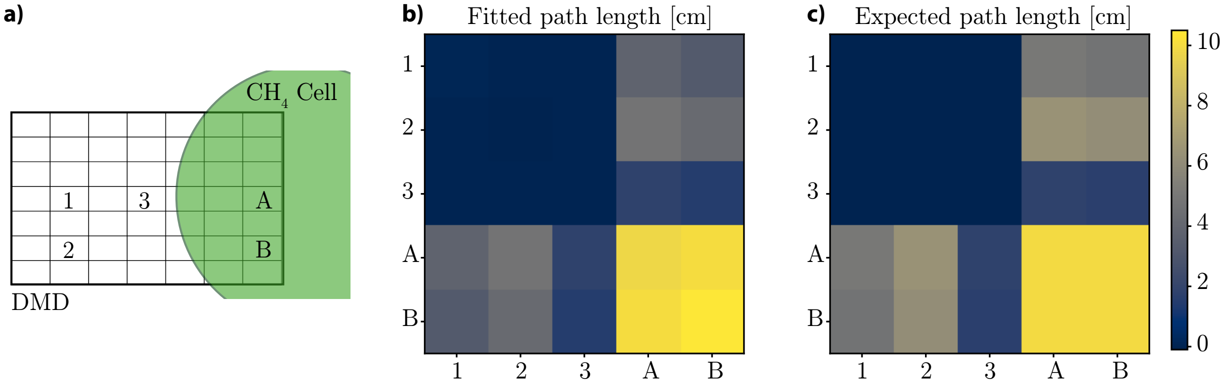

Figure 4.10: a) The DMD is segmented into a 7x7 grid of superpixels, and five are chosen. The pixels numbered 1, 2, and 3 diffract light which does not pass through the methane cell, and the pixels lettered A and B diffract light which does pass through the methane cell. b and c) Fitted and expected path lengths for individual pixels (diagonals) and groups of two pixels. Both b) and c) share the color bar at right.

0.11 cm and 0.46 cm of the known path length of 0 or 10 cm of methane, respectively. The fitted path lengths for the measurements consisting of one pixel which probes the methane cell and one pixel which does not probe the methane cell appear to vary according to an intensity weighted path length given by

$$L_{eff} = \frac{\sum_i I_{0,i} L_i}{\sum_i I_{0,i}}, \tag{4.19}$$

where the effective path length L_{eff} is given by the weighted average of the absorbing path lengths L_i for each of the i contributing pixels, where the weight is given by the diffracted intensity $I_{0,i}$ of each of the pixels. In the present experiment where the absorbing gas exists in a cell of a fixed length in the lab, the fitted path length is the proportion of the light intensity which passes through the cell multiplied by the length of the cell. Here, we estimate the intensity to be related to the power at the focus of lens L1, since the intensity is given by the product of the beam power and the beam area, and we assume the area which scales the power is constant for all measurements.

To deduce a more general understanding of how the path length varies when multiple pixels are transmitted in a single measurement, we return to the Beer-Lambert Law (Eq. 4.1). We solve

Eq. 4.1 for an effective path length L_{eff}, and equate it to Eq. 4.19:

$$-\frac{1}{k}\ln\left(\frac{I'}{I'_0}\right) = \frac{\sum_i I_{0,i}L_i}{\sum_i I_{0,i}}. \tag{4.20}$$

Here, k is the absorption coefficient and I' and I'_0 denote the transmitted and incident light upon a collection of i pixels, each with incident intensities $I_{0,i}$ probing light with an absorbing path length of L_i. Noting that $I'_0 = \sum_i I_{0,i}$, we find

$$I' = \left(\sum_i I_{0,i}\right) \times \exp\left(\frac{-k\sum_i I_{0,i}L_i}{\sum_i I_{0,i}}\right). \tag{4.21}$$

The transmitted intensity, then, can be understood as the sum of the incident intensity attenuated exponentially by the product of the negative absorption coefficient and the intensity weighted sum of the absorbing pathlengths of each of the pixels. The intensity weighting within the exponent corresponds to the weighting factor in step 2 of Algorithm 1: $w_j = I_{0,j}/\sum_{0,j}^{i} I_{0,j}$.

Following Eq. 4.8, the m-FID signal corresponding to Eq. 4.21 is given by

$$a(t) = \mathcal{F}^{-1}\left\{\underbrace{\frac{\sum_i I_{0,i}L_i k}{\sum_i I_{0,i}}}_{\text{intensity-weighted molecular absorption}} - \underbrace{\ln\left(\sum_i I_{0,i}\right)}_{\text{baseline}}\right\} = \mathcal{F}^{-1}\left\{\sum_{j=1}^{i} w_j k_{\nu,j} L_j - \ln\left(I'_0\right)\right\}. \tag{4.22}$$

Within the m-FID signal, w_j calculated as the incident intensity at the j^{th} pixel normalized by the the total incident intensity scales the absorption coefficient. Whereas the component of the m-FID signal associated with the baseline is localized at small times, the component associated with the molecular absorption is present throughout the signal. Therefore, comparing experimentally collected m-FID signals to m-FID signals generated according to Eq. 4.22 serves as a means for identifying the path lengths of the absorbing molecule of each pixel.

4.4.2 Hyperspectral imaging with dual comb spectroscopy and compressive sensing: Experimental results

We test our hyperspectral imaging using dual comb spectroscopy and compressive sensing on the experimental scene illustrated in Fig. 4.9a. As before, we segment the DMD into an array of

7x7 rectangular superpixels, each measuring 130 pixels by 162 pixels. To select a smaller subset of superpixels to study to keep the computation tractable and to locate the position of the methane test cell, we measure the average power diffracted from each of the superpixels at the Fourier plane of lens L1. This map of average power per superpixel is shown in Fig. 4.11a. The glass of the methane cell blocks light to 14 of the superpixels along the center of the DMD. The methane cell is oriented so that the light incident on the superpixels in the 6th and 7th superpixel column of the DMD absorbs methane and air, whereas the light incident on the first three superpixel columns of the DMD only absorbs only air. We arbitrarily select 20 of these pixels to measure, 12 of which are air only pixels, and 8 of which are methane and air pixels. The selected pixels are indicated in Fig. 4.11b.

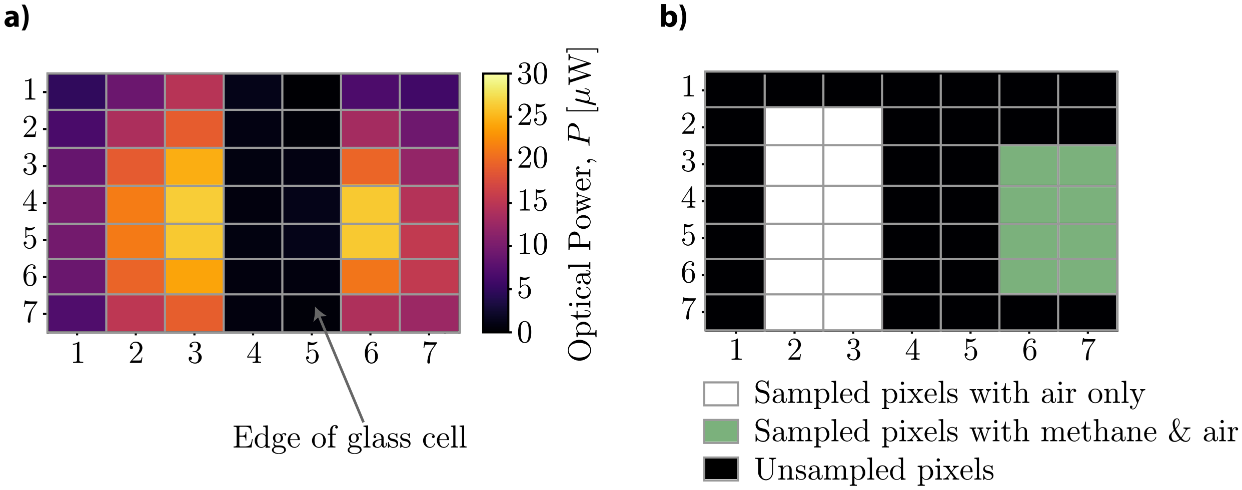

Figure 4.11: a) Optical power diffracted from the digital micromirror device, measured for each of the 49 superpixels. Optical power is nonuniform because DMD is illuminated with a nonuniform, approximately Gaussian, beam. Little light is diffracted from the pixels behind the edge of the glass cell, pixels in columns 4 and 5. The methane cell is oriented in the beam path to cover the pixels in columns 6 and 7. b) Sampled and unsampled pixels. Sampled pixels which interrogate light which passes through air only and air and methane are white and green, respectively. Unsampled pixels are black.

Given a set of pixels to measure, we then generate a measurement matrix which shows 10 of the selected pixels at random for every measurement. The measurement matrix and several representative DMD transmission masks generated from the measurement matrix are shown in

Fig. 4.12.

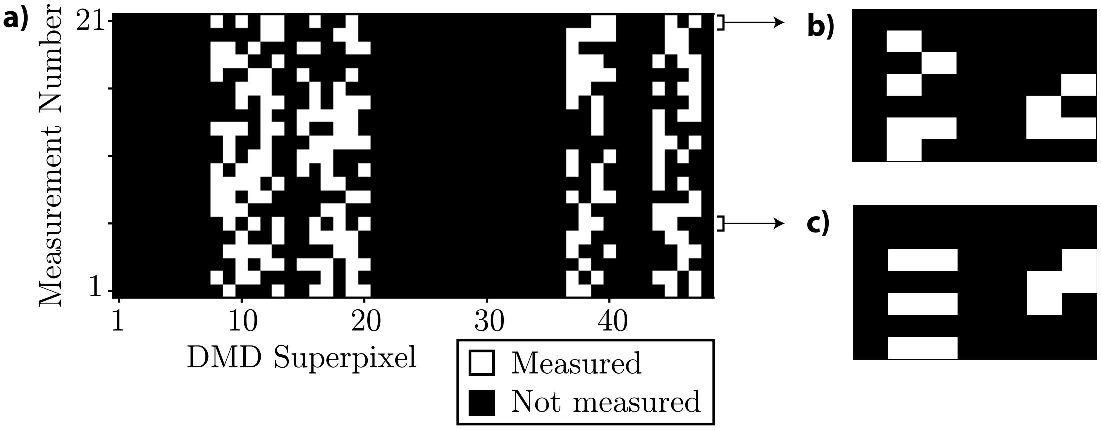

Figure 4.12: a) Measurement matrix for the 49 digital micromirror device (DMD) superpixels used for the smashed filter experiments. Each row constitutes a prescription for a measurement; white and black indicates whether or not a superpixel is measured, respectively. b) and c) Transmission masks displayed on the DMD for measurements 21 and 6, respectively.

We conduct 21 measurements with different transmission masks. Interferograms for each are phase corrected and averaged for 5 minutes. These transmission spectra are converted into m-FID signals and then input to the smashed filter.

Previously, when we applied the smashed filter to simulations, we assumed that each pixel diffracted light with the same intensity. Now in the smashed filter, we must account for varying intensities across different superpixels since the illumination is nonuniform (see Fig. 4.11) according to Eq. 4.22. Yet, at this point, it is unclear how to precisely quantify the scaling intensity within the weighting factor w_j. Previously while developing Eq. 4.22, we examined the path lengths of pairs of 5 different pixels. In that case, we estimated the scaling intensity to be proportional to the average power measured after lens L1 and found good agreement between our experiments and the expectation. A relative intensity map for this strategy is shown in Fig. 4.13a. However, because of the angular dispersion (albeit reduced) and the small active area of the photodetector (0.2 mm^2), it is likely that such a measurement captures more light than is incident on the photodetector. Moreover, the power meter responsivity is biased strongly towards wavelengths smaller than those we use for spectroscopic fits ($\lambda < 1620$ nm). Since we do not filter the light to the spectroscopic bandwidth, an average power measurement conducted in this manner has the potential to be strongly biased by light which is a) not included in the spectroscopic bandwidth, and b) potentially never incident on the photodetector. The intensity weighting factor scales the entire spectrum evenly, even if the spectra from different pixels have different shapes relative to each other (see Figs. 4.7 and 4.9b). We expect that with complete angular dispersion mitigation, these problems would no longer be concerns.

An alternative strategy for calculating the scaling intensity is to use the DC voltage from the photodetector as a proxy for intensity, since this is a direct measure of the intensity incident on the photodetector. A relative intensity map for this strategy is shown in Fig. 4.13b. While this measurement ensures that the scaling intensity depends only on the light incident on the photodetector, it still does not remove the potential that the measurement is still biased by smaller wavelengths than are included in the spectroscopic optical bandwidth. This could be particularly serious if unfiltered light of these wavelengths is differentially incident on the photodetector as a function of lateral position on the DMD. To account for this, we propose a third potential intensity proxy: the DC voltage from the photodetector when the light incident on the photodetector is spectrally filtered with a filter with a central wavelength of 1620 nm and a FWHM=12.0±2.4 nm (Thorlabs, FB1620-12). This filter is selected since the light it transmits absorbs air and methane only weakly, and its spectral range is located close to the absorption features we fit. A relative intensity map for this strategy is shown in Fig. 4.13c.

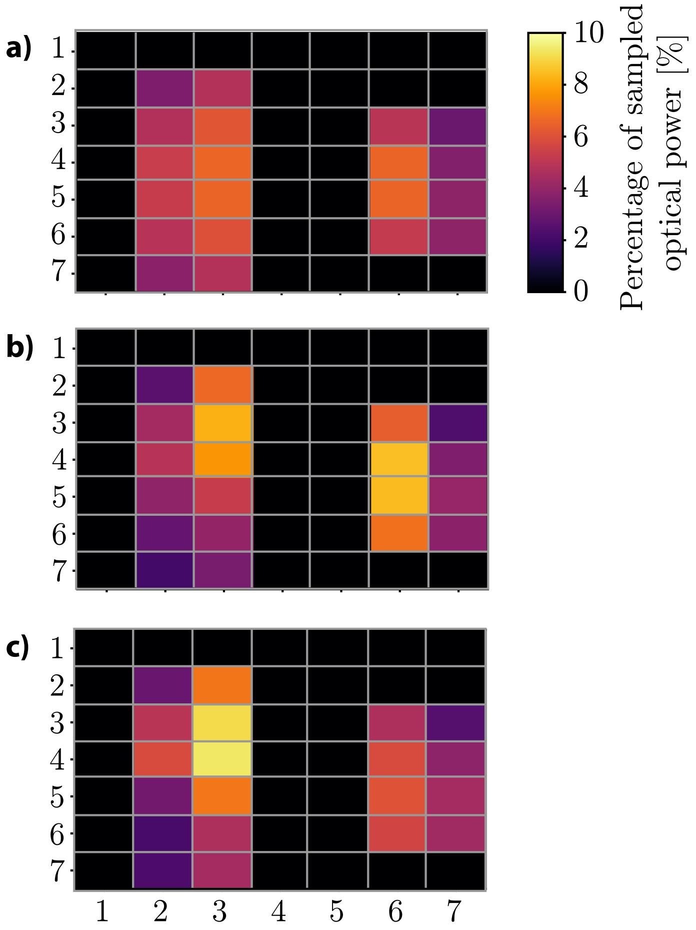

Figure 4.13: Proportion of total sampled optical power at each sampled pixel. a) average optical power measured at the Fourier plane of lens L1. b) DC bias voltage of interferogram detected on photodetector used as a proxy for power. c) DC bias voltage of interferogram detected on photodetector after a spectral filter with a central wavelength of 1620 nm and a FWHM=12.0±2.4 nmused as a proxy for power. All panels use to the same colorbar at right.

Because each of the three proposed intensity proxies holds the potential to serve as the correct scaling, we consider each of them in the analysis which follows. First, we run the smashed filter with 21 measurements using each of the intensity scalings shown in Fig. 4.13. The results are shown in Fig. 4.14. In all cases, we observe good agreement between the recovered and expected path lengths for the superpixels at which no methane exists. When methane is present, path lengths are underestimated; yet, the presence of methane is evident. While the scaling using the power meter to measure average power leads to recovered methane path lengths close to the expectation for half of the methane superpixels, a path length close to 0 is wrongly attributed to a pixel within the methane region. Better agreement exists for both of the strategies using the DC voltage of the interferograms.

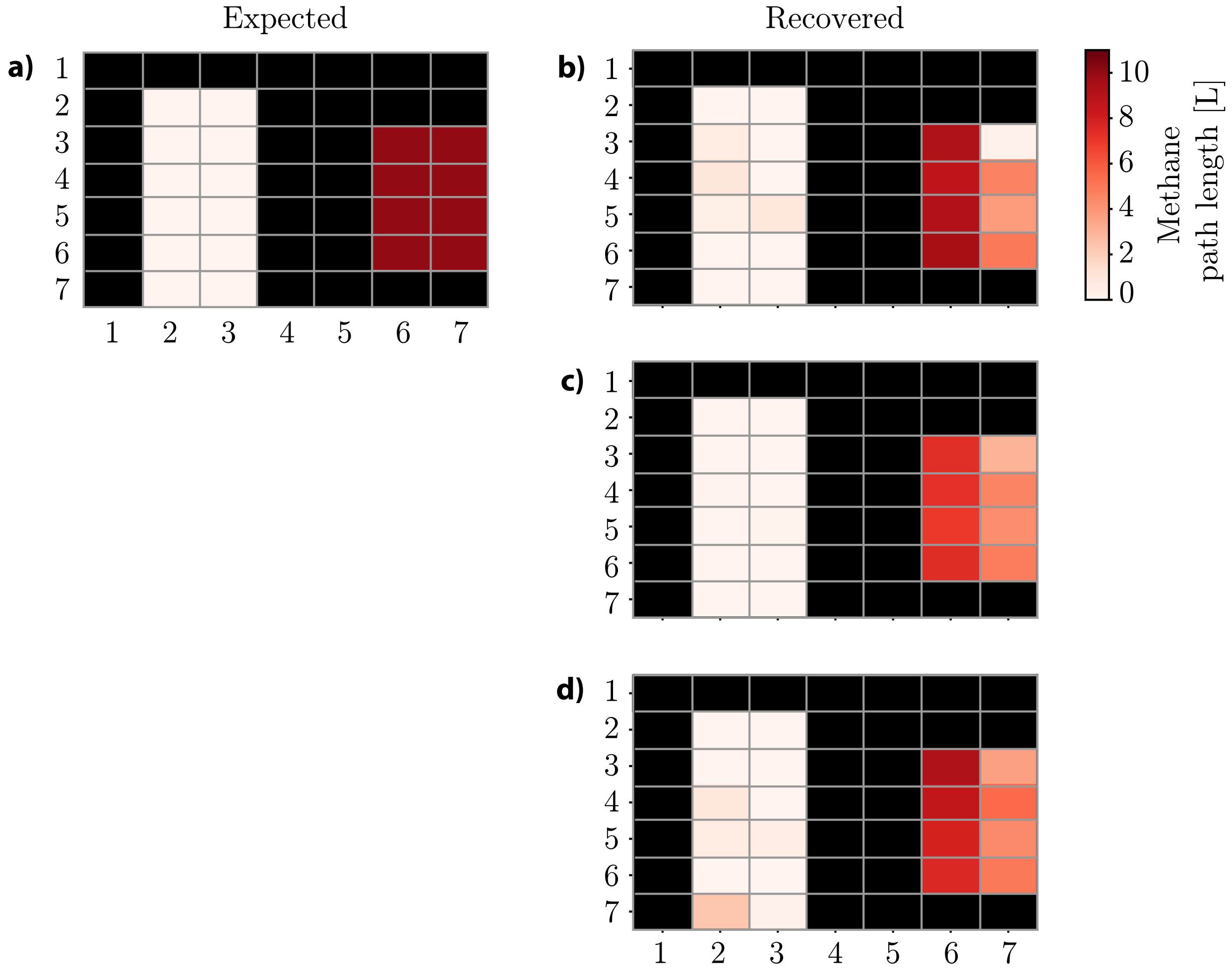

Figure 4.14: Results from the experimental demonstration of hyperspectral imaging using dual frequency comb spectroscopy and compressive sensing. Expected (a) and reconstructed from 21 experiments (b-d) methane path lengths of the sampled scene. The intensity proxy for b) c), and d) is the average optical power measured at the Fourier plane of lens L1, the DC bias voltage of interferograms detected on the photodetector, and the DC bias voltage of interferograms detected on the photodetector after a spectral filter with a central wavelength of 1620 nm and a FWHM=12.0±2.4 nm, respectively.

As discussed in Sec. 4.1.5, one of the appeals of compressive sensing is that the number of measurements required to reconstruct an image may be smaller than the number of pixels. To evaluate if this benefit transfers to our experiment, we run the smashed filter for randomly selected set of N measurements, varying $7 \leq N \leq 20$. For each N, we choose select 8 different sets of measurements. We repeat this exercise three times, once for each potential intensity scaling metric. Representative recovered temperature fields for different N using the power meter-measured intensity scaling metric are shown in Fig. 4.15.

Interestingly, for $N \geq 13$, superpixels (7,3), (7,4), (7,5), and (7,6) have apparently lower recovered methane path lengths. Additionally, the superpixel (7,3) has a substantially lower methane path length than expected. The consistency of these discrepancies throughout these reconstructions suggests that either the measurements or the spectroscopy models misrepresent this column, and that the smashed filter is not to blame for the error.

We quantify the efficacy of the methane path length recoveries for each iteration of the smashed filter using two metrics, the structural similarity index (SSIM) [180] and the mean square error (MSE). We present our results for each of the possible intensity scaling factors in Fig. 4.16. The SSIM is a metric used to evaluate image quality which compares a measured image to a known reference. The SSIM ranges between -1 and +1, where values of -1 and +1 indicate poor and perfect reconstructions, respectively. Compared to the SSIM, the MSE is a less refined strategy for comparing images since it correlates poorly with our visual intuition of a good reconstruction [180], but it provides a rough estimation of the average magnitude of the error. Increasing values of the SSIM and decreasing values of the MSE indicate increasing performance. In Fig. 4.16, we see that both metrics plateau at approximately $N = 13$, indicating that only 13 measurements may be necessary to reconstruct the methane path lengths. This is consistent with the representative examples shown in Fig. 4.15.

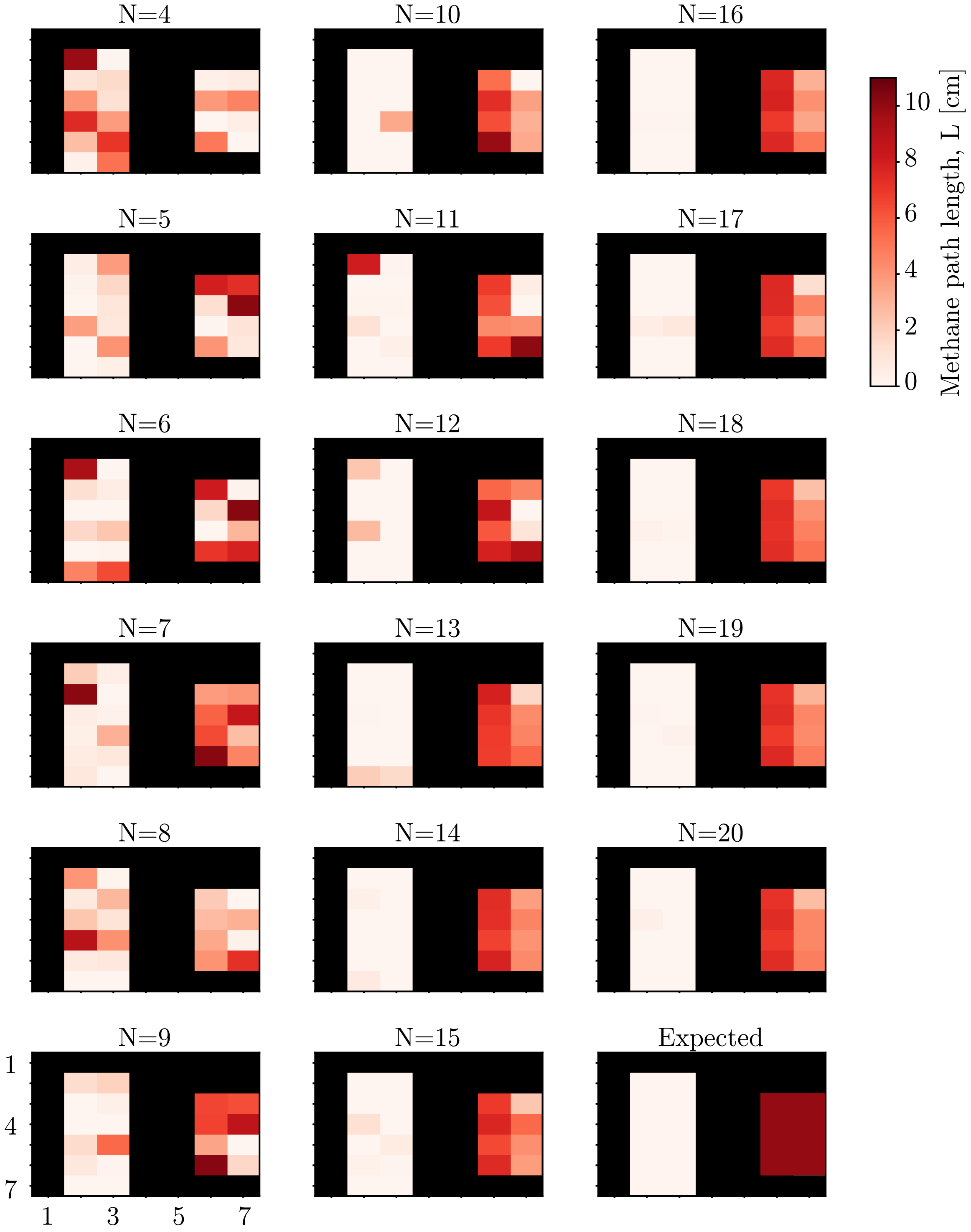

Figure 4.15: Recovered methane path lengths as a function of N, the number of measurements used in the smashed filter. N indicated above each reconstruction. The N measurements are chosen at random. All panels use the same colorbar at right. This data uses the scaling metric measured from the power meter.

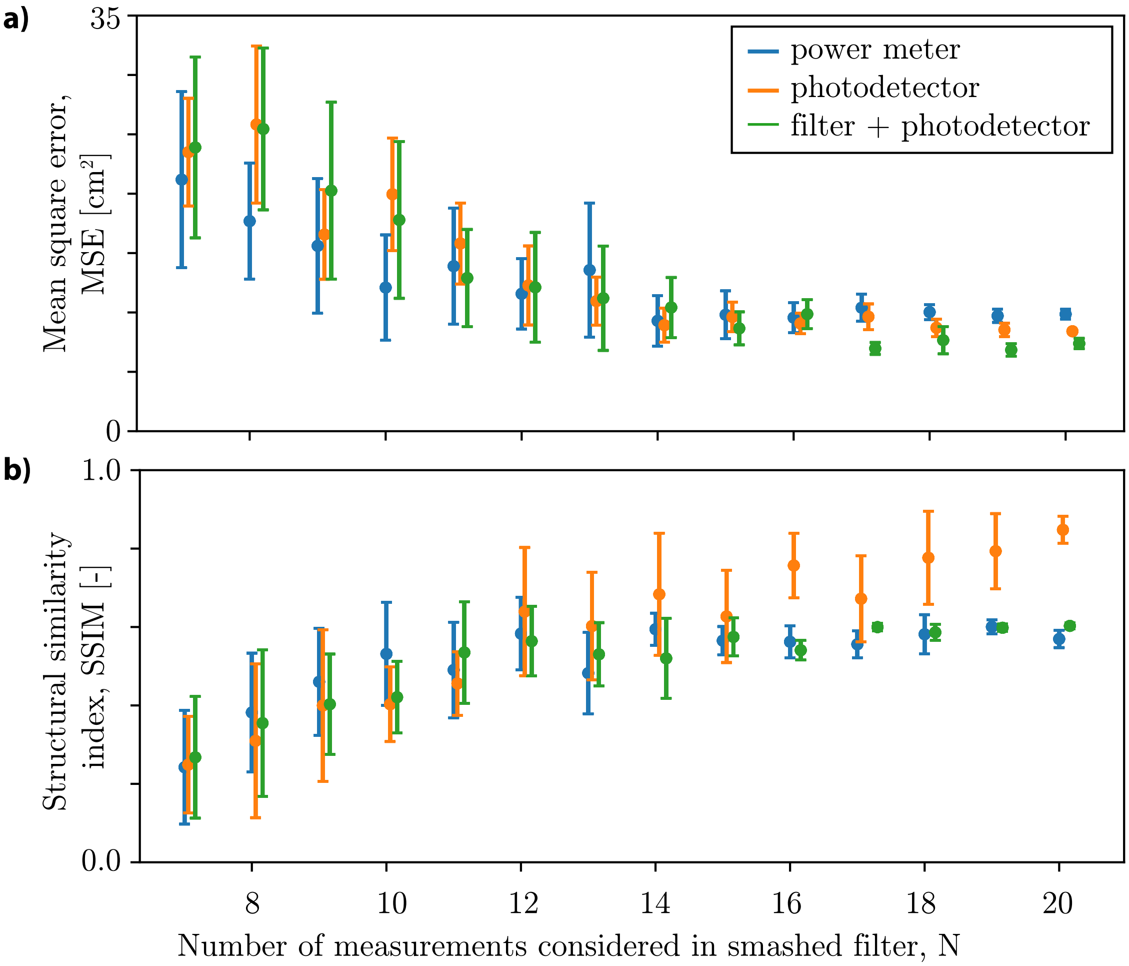

Figure 4.16: Evidence that compressed sensing requires fewer measurements than traditional sensing. a) Mean square error and b) Structural similarity index as functions of the number of measurements considered in the smashed filter.

4.5 Future Work

In this chapter, we have developed an approach for generating spatially resolved broadband hyperspectral images using compressive sensing and dual comb spectroscopy. We have demonstrated this sensor in a controlled experimental setting in which a methane cell partially occludes a portion of the beam. This constitutes, to the best of our knowledge, the first demonstration of hyperspectral imaging using dual frequency comb spectroscopy and compressive sensing. This is particularly interesting because the broadband nature of the spectroscopic measurements is not compromised by the detection strategy.

We are excited about the prospect of future experiments which better harness the broadband capabilities of DCS, namely that it can distinguish multiple chemical species, and that it can measure temperatures, species concentrations, and pressures accurately and precisely. As a first step, we recommend fully compensating for the angular dispersion to eliminate the detection issues discussed above. As a first experiment, we suggest conducting an experiment in which the entire system is enveloped in a carbon dioxide vessel. In this experiment, we anticipate that superpixels would probe either a long path of carbon dioxide, or a shorter path of carbon dioxide with a short path of methane.

While quantifying the presence and amount of methane in a scene has the potential to facilitate methane leak detection [181, 164], other applications exist. In particular, we are excited about sensing gaseous temperatures. We anticipate that the intensity weighting scheme developed in Sec. 4.4.1.2 could be expanded to act on variables within the absorption coefficient k to accommodate temperature variations.

Thermocouples are a standard tool for measuring temperatures, but when used for measuring the temperatures of hot gasses, losses due to radiation must be corrected for [182, 183]. Frequently, such corrections are ad hoc and transfer poorly between different experiments [182]. Even if radiative transfers are accounted for, inserting a thermocouple into a flow is invasive and can impact the flow of the system [184], especially in combustion systems [183]. Moreover, thermocouple surfaces can have catalytic effects if not properly coated, leading to fundamental changes in the chemical kinetics of the system [185, 186]. Critically, thermocouples are point sensors, meaning that they only measure the temperature at one place in space. An alternative modality for gas state temperature measurements is absorption spectroscopy, since absorption spectra have a strong dependence on temperature (see Eqs. 4.4 and 4.3). Absorption spectroscopy measurements have been implemented in a variety of harsh environments, ranging from scram jets [187] to entrained flow gasifiers [91] to rapid compression machines [92].

To test our approach for measuring gas temperatures, we have simulated a 5x3 pixel temperature scene with a temperature distribution according to a bidirectional temperature gradient. We sampled this temperature scene using the bottom 15x15 entries of a 16x16 Hadamard matrix, excluding its first row and first column. This sampling matrix is illustrated in Fig. 4.17a. Measurements of water vapor at pressure $P = 0.85$ atm, mole fraction $\chi = 0.04$, and path length $L = 1$ m spanning 6387-9582 cm^{-1} were then simulated from the HITRAN 2016 database according to the sampled temperatures, following the procedure detailed in Algorithm 1.

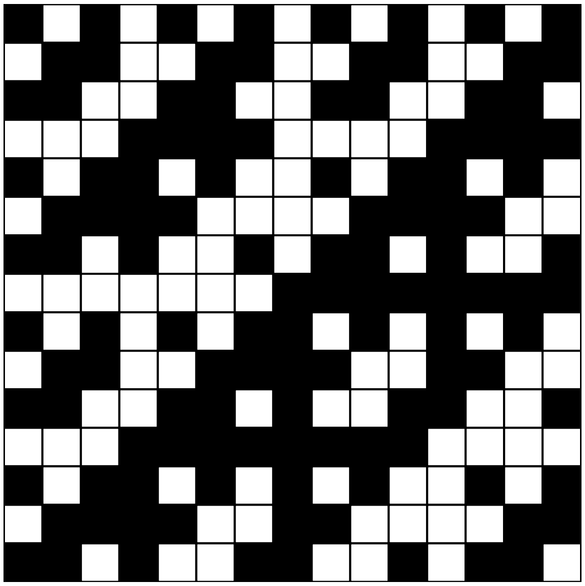

Figure 4.17: Measurement matrix. Measurements are acquired according to the inner product of the measurement matrix, where the black and white squares indicate the pixels which are and are not sampled, respectively. Each row of this matrix corresponds to a measurement.

Next, we input these measurements, the measurement matrix, and the reference database into the smashed filter. The results are shown in Fig. 4.18. The maximum difference in temperature between the measured and the reconstructed values is 0.0045 K (0.0011%). The statistical uncertainties associated with each fit are less than 0.01 K. We note that these statistical uncertainties are much smaller than when the spectra according to a single pixel is fitted in isolation. We assume that this is a consequence of how the temperature information from any given pixel appears in multiple measurements (see Fig. 4.3).

These simulations indicate that temperature measurements in the framework proposed in

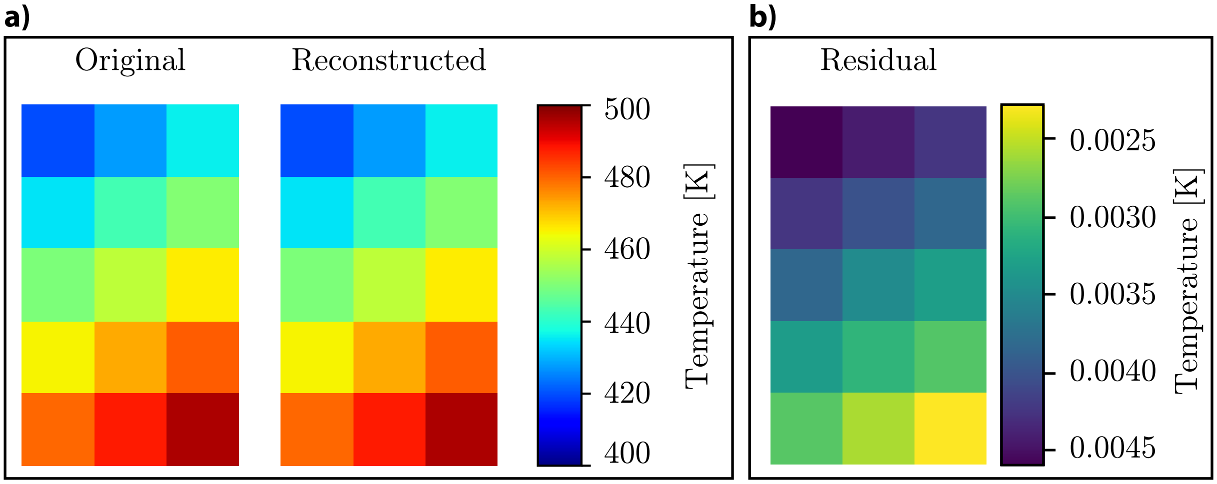

Figure 4.18: Temperature fields. a) original (left) and reconstructed (right). b) residual, calculated as the difference between the original and reconstructed temperature fields.

this chapter are viable. To confirm this finding, we suggest conducting the experiment indicated schematically in Fig. 4.19. In this experiment, we suggest creating a temperature gradient using a hot plate oriented vertically along the beam path, and measuring the temperature of ambient water near the surface of the hot plate. Then, we suggest comparing the measured temperatures to the analytical solution for the temperature of a gas undergoing natural convection next to a hot wall [188, 189]. Computationally, this problem requires slightly more resources since the absorption coefficient k_ν depends on temperature, so it must be recalculated at every iteration within the smashed filter. To expedite the computation, we recommend calculating $k_\nu(T)$ using a GPU accelerated absorption simulation [190] or creating a lookup table for $k_\nu(T)$ from HAPI rather than querying HAPI directly.

More work is required to understand how to best scale the quantity of interest within the smashed filter according to the transverse beam profile incident on the DMD. We note that this could potentially be bypassed by structuring the illumination beam with a top hat intensity profile, potentially using a rectangular core multimode fiber or in a specialized fiber connector [191].

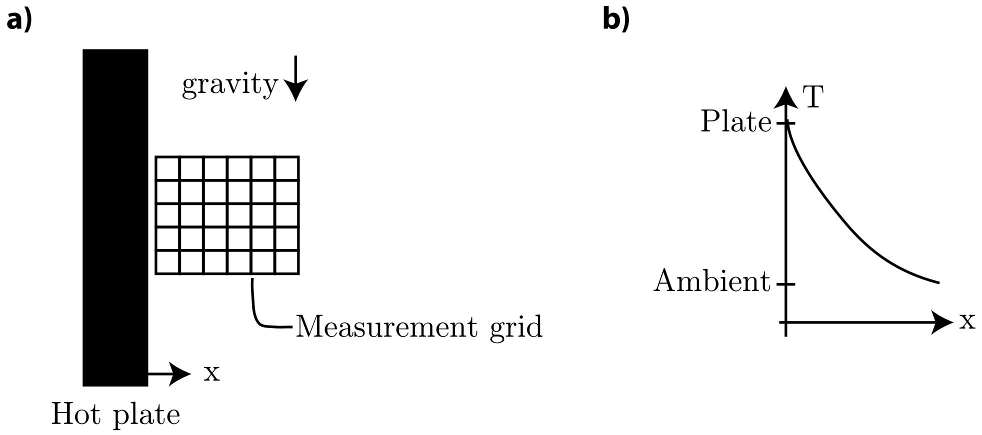

Figure 4.19: Future experiment concept. a) Schematic of potential future experiment. A vertical hot plate heats H_2O vapor near it. The temperature gradient which develops at steady state is imaged, and transverse resolution is given to the experiment according to the grid. b) Expected temperature gradient as a function of distance from the hot plate.

Chapter 5

Thesis summary

In this thesis, we have examined and demonstrated how spatial patterns can be leveraged at each of the three stages of a simplified optical sensor: the illumination, the system under study, and the detection.

In the context of structured illumination, we developed a new velocimetry technique which correlates the fluid velocity with the signals arising from light scattered by small particles embedded in a fluid flow as they travel through a beam of structured light. Previous instruments in this class of velocimetry relied on the scattered light signals having a single modulation frequency which, along with a parameter describing the structured illumination, would yield the flow velocity. By generalizing the structure of the illuminating light and allowing for nonlinear particle trajectories, we generated a complex set of possible signals, and no single metric could be used to characterize the pathline of the particle through the illumination. These signals were not readily interpretable using signal processing techniques belonging to the other velocimeters. Therefore, we designed a machine learning-based signal processing approach to support this broad class of velocimeters. While we demonstrated this technique as an angular velocimeter, we expect that it could also be used to measure other kinematic quantities such as flow rates and velocity gradients.

Addressing the patterning the system under study, we present a strategy for aligning a beam of light to the axis of rotation of a spinning surface. Whereas previous strategies required affixing bulky or heavy optical components to the rotor and potentially complicated detection schemes, the concept we develop and test is simple and can be implemented in real-time by monitoring the signal from a photodiode on an oscilloscope.

Patterned detection is used in the final chapter, where we develop a new hyperspectral imaging modality. This technique is inspired by the architecture of a single pixel camera and uses a programmable transmission mask to selectively permit various patterns of light which have traveled through a gaseous species to transmit to a single photodiode. In this project, we endow dual frequency comb spectroscopy with spatial resolution. Our work constitutes, to the best of our knowledge, the first demonstration of spatially resolved dual frequency comb spectroscopy. We anticipate that such measurements will enable research and development in settings where sharp temperature gradients traditionally hinder spectroscopic measurements of temperature, as at the edges of flames and near hot surfaces.

The work collected in this thesis is presented in the following peer reviewed papers:

(1) E. F. Strong, A. Q. Anderson, M. P. Brenner, B. M. Heffernan, N. Hoghooghi, J. T. Gopinath, and G. B. Rieker, "Angular velocimetry for fluid flows: an optical sensor using structured light and machine learning," Opt. Express, vol. 29, pp. 9960-9980, 2021.

(2) E. F. Strong, A. Q. Anderson, J. T. Gopinath, and G. B. Rieker, "Centering a beam of light to the axis of rotation of a planar object," Review of Scientific Instruments, vol. 91, no. 10, p. 105101, 2020.

(3) E.F. Strong, S. C. Coburn, A. Q. Anderson, R. K. Cole, J. T. Gopinath, S. Becker, and G. B. Rieker, "Hyperspectral imaging using dual frequency comb spectroscopy and compressive imaging" (in progress).

The following coauthored publications conducted during my time at the University of Colorado, Boulder are thematically related but are not described in detail in this thesis:

(1) A. Q. Anderson, E.F. Strong, S. C. Coburn, G. B. Rieker, and J. T. Gopinath, "Orbital Angular Momentum-Based Dual Comb Interferometer for Ranging and Rotation Sensing" (in press).

(2) A. Q. Anderson, E. F. Strong, B. M. Heffernan, M. E. Siemens, G. B. Rieker, and J. T. Gopinath, “Observation of the rotational doppler shift with spatially incoherent light,” Optics Express, vol. 29, no. 3, pp. 4058-4066, 2021.

(3) A. Q. Anderson, E. F. Strong, B. M. Heffernan, M. E. Siemens, G. B. Rieker, and J. T. Gopinath, “Detection technique effect on rotational doppler measurements,” Optics letters, vol. 45, no. 9, pp. 2636-2639, 2020.

(4) A. S. Makowiecki, D. I. Hermain, N. Hoghooghi, E. F. Strong, R. K. Cole, G. Ycas, F. R. Giorgetta, C. B. Lapointe, J. F. Glussman, J. W. Daily, P. E. Hamlington, N. R. Newbury, I. R. Coddington, and G. B. Rieker, “Mid-infrared dual frequency comb spectroscopy for combustion analysis from 2.8 to 5 μm,” Proceedings of the Combustion Institute, vol. 38, no 1, pp. 1627-1635.

The following provisional patents have been issued covering our work:

(1) U. S. Provisional Patent 63/022,540: Structured-Light Velocimetry for Sensing Angular Velocity. Filed on May 11, 2020.

(2) U. S. Provisional Patent 63/161,368: Angular Velocimetry for Fluid Flows. Filed on March 19, 2021.

The structured light velocimetry simulation and analysis code developed and used throughout Chap. 2 is publicly available in the following GitHub repository:

(1) E. F. Strong, “slvel,” `www.github.com/Liz-Strong/slvel` 2021.

Bibliography

[1] A. Ryabtsev, S. Pouya, A. Safaripour, M. Koochesfahani, and M. Dantus, “Fluid flow vorticity measurement using laser beams with orbital angular momentum,” Optics Express, vol. 24, pp. 11762–11767, May 2016.

[2] A. Belmonte, C. Rosales-Guzmán, and J. P. Torres, “Measurement of flow vorticity with helical beams of light,” Optica, vol. 2, pp. 1002–1005, Nov. 2015.

[3] A. N. Kolmogorov, “The local structure of turbulence in incompressible viscous fluid for very large reynolds numbers,” Cr Acad. Sci. URSS, vol. 30, pp. 301–305, 1941.

[4] R. McKeown, R. Ostilla-Mónico, A. Pumir, M. P. Brenner, and S. M. Rubinstein, “Cascade leading to the emergence of small structures in vortex ring collisions,” Physical Review Fluids, vol. 3, no. 12, p. 124702, 2018.

[5] A. Q. Anderson, E. F. Strong, B. M. Heffernan, M. E. Siemens, G. B. Rieker, and J. T. Gopinath, “Detection technique effect on rotational doppler measurements,” Optics letters, vol. 45, no. 9, pp. 2636–2639, 2020.

[6] A. Q. Anderson, E. F. Strong, B. M. Heffernan, M. E. Siemens, G. B. Rieker, and J. T. Gopinath, “Observation of the rotational doppler shift with spatially incoherent light,” Optics Express, vol. 29, no. 3, pp. 4058–4066, 2021.

[7] E. F. Strong, A. Q. Anderson, M. P. Brenner, B. M. Heffernan, N. Hoghooghi, J. T. Gopinath, and G. B. Rieker, “Angular velocimetry for fluid flows: an optical sensor using structured light and machine learning,” Opt. Express, vol. 29, pp. 9960–9980, Mar 2021.

[8] B. McKeon, G. Comte-Bellot, J. Foss, J. Westerweel, F. Scarano, C. Tropea, J. Meyers, J. Lee, A. Cavone, R. Schodl, M. Koochesfahani, Y. Andreopoulos, W. Dahm, J. Mullin, J. Wallace, P. Vukoslavčević, S. Morris, E. Pardyjak, and A. Cuerva, “Velocity, vorticity, and mach number,” in Springer Handbooks, pp. 215–471, Springer, 2007.

[9] Y. Aizu and T. Asakura, Spatial filtering velocimetry: Fundamentals and applications, vol. 116. Springer Science & Business Media, 2006.

[10] M. Gaster, “A new technique for the measurement of low fluid velocities,” Journal of Fluid Mechanics, vol. 20, pp. 183–192, Oct. 1964.

[11] A. Hayashi and Y. Kitagawa, “Image velocity sensing using an optical fiber array,” Applied optics, vol. 21, no. 8, pp. 1394–1399, 1982. ISBN: 2155-3165 Publisher: Optical Society of America.

[12] M. A. R. Koehl and T. Cooper, "Swimming in an unsteady world," Integrative and Comparative Biology, vol. 55, no. 4, pp. 683–697, 2015. ISBN: 1557-7023 Publisher: Oxford University Press.

[13] S. Asher and U. Shavit, "The effect of water depth and internal geometry on the turbulent flow inside a coral reef," Journal of Geophysical Research: Oceans, vol. 124, no. 6, pp. 3508–3522, 2019. ISBN: 2169-9275 Publisher: Wiley Online Library.

[14] E. Bou, A. Ly, J. Roul, O. Llopis, C. Vieu, and A. Cerf, "Compact system for in situ laser Doppler velocimetry of blood flow," Biomedical Optics Express, vol. 10, pp. 5862–5876, Oct. 2019.

[15] E. P. Hassel and S. Linow, "Laser diagnostics for studies of turbulent combustion," Measurement Science and Technology, vol. 11, no. 2, p. R37, 2000.

[16] C. Fang and L. I. U. Hong, "Particle image velocimetry for combustion measurements: Applications and developments," Chinese Journal of Aeronautics, vol. 31, no. 7, pp. 1407–1427, 2018. ISBN: 1000-9361 Publisher: Elsevier.

[17] C. Rosales-Guzmán, N. Hermosa, A. Belmonte, and J. P. Torres, "Experimental detection of transverse particle movement with structured light," Scientific Reports, vol. 3, p. 2815, Oct. 2013. Number: 1 Publisher: Nature Publishing Group.

[18] F. Durst, J. H. Whitelaw, and A. Melling, Principles and practice of laser-Doppler anemometry. No. Book, Whole, London;New York;: Academic Press, 2nd ed., 1981.

[19] A. A. Naqwi and W. C. Reynolds, "Measurement of turbulent wall velocity gradients using cylindrical waves of laser light," Experiments in fluids, vol. 10, no. 5, pp. 257–266, 1991. ISBN: 0723-4864 Publisher: Springer.

[20] A. A. Naqwi and S. Petrik, "Fiber-optic dual-cylindrical wave sensor for measurement of wall velocity gradient in a fluid flow," Applied optics, vol. 32, no. 30, pp. 6128–6131, 1993. ISBN: 2155-3165 Publisher: Optical Society of America.

[21] D. W. Wilson, J. A. Scaif, S. Forouhar, R. E. Muller, F. Taugwalder, M. Gharib, D. Fourguette, and D. Modarress, "Diffractive optic fluid shear stress sensor," in Diffractive Optics and Micro-Optics, p. DThB5, Optical Society of America, 2000.

[22] M. P. J. Lavery, F. C. Speirits, S. M. Barnett, and M. J. Padgett, "Detection of a Spinning Object Using Light Orbital Angular Momentum," Science, vol. 341, pp. 537–540, Aug. 2013.

[23] D. Phillips, M. Lee, F. Speirits, S. Barnett, S. Simpson, M. Lavery, M. Padgett, and G. Gibson, "Rotational doppler velocimetry to probe the angular velocity of spinning microparticles," Physical Review A, vol. 90, no. 1, p. 011801, 2014.

[24] M. B. Frish and W. W. Webb, "Direct measurement of vorticity by optical probe," Journal of Fluid Mechanics, vol. 107, pp. 173–200, 1981.

[25] A. J. Majda, A. L. Bertozzi, and A. Ogawa, "Vorticity and incompressible flow. cambridge texts in applied mathematics," Appl. Mech. Rev., vol. 55, no. 4, pp. B77–B78, 2002.

[26] L. Allen, M. W. Beijersbergen, R. Spreeuw, and J. Woerdman, “Orbital angular momentum of light and the transformation of laguerre-gaussian laser modes,” Physical review A, vol. 45, no. 11, p. 8185, 1992.

[27] C. G. Darwin, “Notes on the theory of radiation,” Proceedings of the Royal Society of London. Series A, Containing Papers of a Mathematical and Physical Character, vol. 136, no. 829, pp. 36–52, 1932.

[28] M. J. Padgett, “Orbital angular momentum 25 years on,” Optics express, vol. 25, no. 10, pp. 11265–11274, 2017.

[29] B. E. Saleh and M. C. Teich, Fundamentals of photonics. john Wiley & sons, 2019.

[30] D. L. Andrews, Structured light and its applications: An introduction to phase-structured beams and nanoscale optical forces. Academic press, 2011.

[31] M. Padgett and L. Allen, “The poynting vector in laguerre-gaussian laser modes,” Optics communications, vol. 121, no. 1-3, pp. 36–40, 1995.

[32] J. Leach, S. Keen, M. J. Padgett, C. Saunter, and G. D. Love, “Direct measurement of the skew angle of the poynting vector in a helically phased beam,” Optics express, vol. 14, no. 25, pp. 11919–11924, 2006.

[33] R. Adler, “Interaction between light and sound,” IEEE spectrum, vol. 4, no. 5, pp. 42–54, 1967.

[34] L. Fang, M. J. Padgett, and J. Wang, “Sharing a common origin between the rotational and linear doppler effects,” Laser & Photonics Reviews, vol. 11, no. 6, p. 1700183, 2017.

[35] L. Allen, M. Babiker, and W. Power, “Azimuthal doppler shift in light beams with orbital angular momentum,” Optics Communications, vol. 112, no. 3-4, pp. 141–144, 1994.

[36] M. J. Padgett, “The mechanism for energy transfer in the rotational frequency shift of a light beam,” Journal of Optics A: Pure and Applied Optics, vol. 6, no. 5, p. S263, 2004.

[37] H. Zhou, D. Fu, J. Dong, P. Zhang, and X. Zhang, “Theoretical analysis and experimental verification on optical rotational doppler effect,” Optics express, vol. 24, no. 9, pp. 10050–10056, 2016.

[38] M. P. J. Lavery, S. M. Barnett, F. C. Speirits, and M. J. Padgett, “Observation of the rotational Doppler shift of a white-light, orbital-angular-momentum-carrying beam backscattered from a rotating body,” Optica, vol. 1, pp. 1–4, July 2014.

[39] S. Qiu, T. Liu, Y. Ren, Z. Li, C. Wang, and Q. Shao, “Detection of spinning objects at oblique light incidence using the optical rotational doppler effect,” Optics express, vol. 27, no. 17, pp. 24781–24792, 2019.

[40] C. Rosales-Guzmán, N. Hermosa, A. Belmonte, and J. P. Torres, “Measuring the translational and rotational velocities of particles in helical motion using structured light,” Optics Express, vol. 22, pp. 16504–16509, June 2014. Publisher: Optical Society of America.

[41] Y. Zhai, S. Fu, C. Yin, H. Zhou, and C. Gao, “Detection of angular acceleration based on optical rotational doppler effect,” Optics express, vol. 27, no. 11, pp. 15518–15527, 2019.

[42] W. Zhang, J. Gao, D. Zhang, Y. He, T. Xu, R. Fickler, and L. Chen, "Free-space remote sensing of rotation at the photon-counting level," Physical Review Applied, vol. 10, no. 4, p. 044014, 2018.

[43] S. Barreiro, J. Tabosa, H. Failache, and A. Lezama, "Spectroscopic observation of the rotational doppler effect," Physical review letters, vol. 97, no. 11, p. 113601, 2006.

[44] G. Nienhuis, "Doppler effect induced by rotating lenses," Optics communications, vol. 132, no. 1-2, pp. 8–14, 1996.

[45] J. Courtial, K. Dholakia, D. Robertson, L. Allen, and M. Padgett, "Measurement of the rotational frequency shift imparted to a rotating light beam possessing orbital angular momentum," Physical review letters, vol. 80, no. 15, p. 3217, 1998.

[46] M. V. Vasnetsov, V. A. Pas' Ko, and M. S. Soskin, "Analysis of orbital angular momentum of a misaligned optical beam," New Journal of Physics, vol. 7, no. 1, p. 46, 2005.

[47] G. Molina-Terriza, J. P. Torres, and L. Torner, "Management of the angular momentum of light: preparation of photons in multidimensional vector states of angular momentum," Physical review letters, vol. 88, no. 1, p. 013601, 2001.

[48] A. O'neil, I. MacVicar, L. Allen, and M. Padgett, "Intrinsic and extrinsic nature of the orbital angular momentum of a light beam," Physical review letters, vol. 88, no. 5, p. 053601, 2002.

[49] A. E. Willner, H. Huang, Y. Yan, Y. Ren, N. Ahmed, G. Xie, C. Bao, L. Li, Y. Cao, Z. Zhao, et al., "Optical communications using orbital angular momentum beams," Advances in Optics and Photonics, vol. 7, no. 1, pp. 66–106, 2015.

[50] G. Gibson, J. Courtial, M. J. Padgett, M. Vasnetsov, V. Pasko, S. M. Barnett, and S. Franke-Arnold, "Free-space information transfer using light beams carrying orbital angular momentum," Optics express, vol. 12, no. 22, pp. 5448–5456, 2004.

[51] J. Wang, J.-Y. Yang, I. M. Fazal, N. Ahmed, Y. Yan, H. Huang, Y. Ren, Y. Yue, S. Dolinar, M. Tur, et al., "Terabit free-space data transmission employing orbital angular momentum multiplexing," Nature photonics, vol. 6, no. 7, pp. 488–496, 2012.

[52] N. Bozinovic, Y. Yue, Y. Ren, M. Tur, P. Kristensen, H. Huang, A. E. Willner, and S. Ramachandran, "Terabit-scale orbital angular momentum mode division multiplexing in fibers," science, vol. 340, no. 6140, pp. 1545–1548, 2013.

[53] C. Paterson, "Atmospheric turbulence and orbital angular momentum of single photons for optical communication," Physical review letters, vol. 94, no. 15, p. 153901, 2005.

[54] G. A. Tyler and R. W. Boyd, "Influence of atmospheric turbulence on the propagation of quantum states of light carrying orbital angular momentum," Optics letters, vol. 34, no. 2, pp. 142–144, 2009.

[55] J. Vaughan and D. Willetts, "Temporal and interference fringe analysis of tem 01* laser modes," JOSA, vol. 73, no. 8, pp. 1018–1021, 1983.

[56] A. J. Lee, C. Zhang, T. Omatsu, and H. M. Pask, "An intracavity, frequency-doubled self-raman vortex laser," Optics express, vol. 22, no. 5, pp. 5400–5409, 2014.

[57] L. Marrucci, E. Karimi, S. Slussarenko, B. Piccirillo, E. Santamato, E. Nagali, and F. Sciarrino, "Spin-to-orbital conversion of the angular momentum of light and its classical and quantum applications," Journal of Optics, vol. 13, no. 6, p. 064001, 2011.

[58] V. Y. Bazhenov, M. Vasnetsov, and M. Soskin, "Laser beams with screw dislocations in their wavefronts," Jetp Lett, vol. 52, no. 8, pp. 429–431, 1990.

[59] N. Heckenberg, R. McDuff, C. Smith, and A. White, "Generation of optical phase singularities by computer-generated holograms," Optics letters, vol. 17, no. 3, pp. 221–223, 1992.

[60] Y.-X. Ren, R.-D. Lu, and L. Gong, "Tailoring light with a digital micromirror device," Annalen der physik, vol. 527, no. 7-8, pp. 447–470, 2015.

[61] V. Arrizón, U. Ruiz, R. Carrada, and L. A. González, "Pixelated phase computer holograms for the accurate encoding of scalar complex fields," JOSA A, vol. 24, no. 11, pp. 3500–3507, 2007.

[62] S. Oemrawsingh, J. Van Houwelingen, E. Eliel, J. Woerdman, E. Verstegen, J. Kloosterboer, et al., "Production and characterization of spiral phase plates for optical wavelengths," Applied optics, vol. 43, no. 3, pp. 688–694, 2004.

[63] L. E. Drain, "The laser doppler techniques," Chichester, 1980.

[64] A. Belmonte and J. P. Torres, "Optical Doppler shift with structured light," Optics Letters, vol. 36, p. 4437, Nov. 2011.

[65] M. J. Padgett, F. M. Miatto, M. P. J. Lavery, A. Zeilinger, and R. W. Boyd, "Divergence of an orbital-angular-momentum-carrying beam upon propagation," New Journal of Physics, vol. 17, p. 023011, Feb. 2015.

[66] Y. Yeh and H. Cummins, "Localized fluid flow measurements with an he–ne laser spectrometer," Applied Physics Letters, vol. 4, no. 10, pp. 176–178, 1964.

[67] L. Drain, "Coherent and noncoherent methods in doppler optical beat velocity measurement," Journal of Physics D: Applied Physics, vol. 5, no. 3, p. 481, 1972.

[68] E. F. Strong, "slvel." `https://github.com/Liz-Strong/slvel/`, 2021.

[69] "TI DLP LightCrafter 4500 Evaluation Module User's Guide," July 2017.

[70] F. Chollet et al., "keras," 2015.

[71] Martin Abadi and et al., "TensorFlowL Large-Scale Machine Learning on Heterogeneous Systems," 2015.

[72] L. Fang, Z. Wan, A. Forbes, and J. Wang, "A vectorial doppler effect with spatially variant polarized light fields," 2019.

[73] M. Krenn, N. Tischler, and A. Zeilinger, "On small beams with large topological charge," New Journal of Physics, vol. 18, p. 033012, Mar. 2016. Publisher: IOP Publishing.

[74] E. J. Candès and M. B. Wakin, "An introduction to compressive sampling," IEEE signal processing magazine, vol. 25, no. 2, pp. 21–30, 2008.

[75] E. F. Strong, A. Q. Anderson, J. T. Gopinath, and G. B. Rieker, "Centering a beam of light to the axis of rotation of a planar object," Review of Scientific Instruments, vol. 91, no. 10, p. 105101, 2020.

[76] Y. Xie, Z. Lu, F. Li, J. Zhao, and Z. Weng, "Lithographic fabrication of large diffractive optical elements on a concave lens surface," Optics Express, vol. 10, no. 20, pp. 1043–1047, 2002.

[77] L. Fengyou, L. Zhenwu, X. Yongjun, and Z. Dianwen, "Laser direct writing system with cartesian and polar coordinate," Acta Photonica Sinica, vol. 31, no. 5, p. 616, 2002.

[78] T. Wang, W. Yu, D. Zhang, C. Li, H. Zhang, W. Xu, Z. Xu, H. Liu, Q. Sun, and Z. Lu, "Lithographic fabrication of diffractive optical elements in hybrid sol-gel glass on 3-D curved surfaces," Optics Express, vol. 18, no. 24, pp. 25102–25107, 2010.

[79] A. G. Poleshchuk, V. P. Korolkov, V. V. Cherkashin, S. Reichelt, and J. H. Burge, "Polar-coordinate laser writing systems: error analysis of fabricated DOEs," in Lithographic and Micromachining Techniques for Optical Component Fabrication, vol. 4440, pp. 161–172, International Society for Optics and Photonics, 2001.

[80] T. D. Milster and C. L. Vernold, "Technique for aligning optical and mechanical axes based on a rotating linear grating," Optical Engineering, vol. 34, no. 10, pp. 2840–2846, 1995.

[81] S.-J. Jeong, S.-K. Lee, and S.-H. Jeong, "Beam alignment with the axis of a rotation stage for laser fabrication of microcircular structures," Optics & Laser Technology, vol. 36, pp. 401–408, July 2004.

[82] D. B. Phillips, M. P. Lee, F. C. Speirits, S. M. Barnett, S. H. Simpson, M. P. J. Lavery, M. J. Padgett, and G. M. Gibson, "Rotational Doppler velocimetry to probe the angular velocity of spinning microparticles," Physical Review A, vol. 90, no. 1, p. 011801, 2014.

[83] S. Qiu, T. Liu, Z. Li, C. Wang, Y. Ren, Q. Shao, and C. Xing, "Influence of lateral misalignment on the optical rotational Doppler effect," Applied optics, vol. 58, no. 10, pp. 2650–2655, 2019.

[84] S. Qiu, T. Liu, Y. Ren, Z. Li, C. Wang, and Q. Shao, "Detection of spinning objects at oblique light incidence using the optical rotational Doppler effect," Optics express, vol. 27, no. 17, pp. 24781–24792, 2019.

[85] I. V. Basistiy, V. V. Slyusar, M. S. Soskin, M. V. Vasnetsov, and A. Y. Bekshaev, "Manifestation of the rotational Doppler effect by use of an off-axis optical vortex beam," Optics letters, vol. 28, no. 14, pp. 1185–1187, 2003.

[86] J. M. Khosrofian and B. A. Garetz, "Measurement of a Gaussian laser beam diameter through the direct inversion of knife-edge data," Applied optics, vol. 22, no. 21, pp. 3406–3410, 1983.

[87] J. A. Arnaud, W. M. Hubbard, G. D. Mandeville, B. De la Claviere, E. A. Franke, and J. M. Franke, "Technique for fast measurement of Gaussian laser beam parameters," Applied optics, vol. 10, no. 12, pp. 2775–2776, 1971. ISBN: 2155-3165 Publisher: Optical Society of America.

[88] D. R. Skinner and R. E. Whitcher, "Measurement of the radius of a high-power laser beam near the focus of a lens," Journal of Physics E: Scientific Instruments, vol. 5, no. 3, p. 237, 1972. ISBN: 0022-3735 Publisher: IOP Publishing.

[89] A. H. Firester, M. E. Heller, and P. Sheng, "Knife-edge scanning measurements of subwavelength focused light beams," Applied Optics, vol. 16, pp. 1971–1974, July 1977. Publisher: Optical Society of America.

[90] D. Bannon, "Cubes and slices," Nature photonics, vol. 3, no. 11, pp. 627–629, 2009.

[91] P. J. Schroeder, A. S. Makowiecki, M. A. Kelley, R. K. Cole, N. A. Malarich, R. J. Wright, J. M. Porter, and G. B. Rieker, "Temperature and concentration measurements in a high-pressure gasifier enabled by cepstral analysis of dual frequency comb spectroscopy," Proceedings of the Combustion Institute, vol. 38, no. 1, pp. 1561–1569, 2021.

[92] A. D. Draper, R. K. Cole, A. S. Makowiecki, J. Mohr, A. Zdanowicz, A. Marchese, N. Hoghooghi, and G. B. Rieker, "Broadband dual-frequency comb spectroscopy in a rapid compression machine," Optics express, vol. 27, no. 8, pp. 10814–10825, 2019.

[93] Y. Ozaki, C. W. Huck, and K. B. Be, "Chapter 2 - near-ir spectroscopy and its applications," in Molecular and Laser Spectroscopy (V. Gupta, ed.), pp. 11–38, Elsevier, 2018.

[94] I. E. Gordon, L. S. Rothman, C. Hill, R. V. Kochanov, Y. Tan, P. F. Bernath, M. Birk, V. Boudon, A. Campargue, K. Chance, et al., "The hitran2016 molecular spectroscopic database," Journal of Quantitative Spectroscopy and Radiative Transfer, vol. 203, pp. 3–69, 2017.

[95] G. P. Agrawal, "Optical Communication: Its History and Recent Progress," in Optics in Our Time (M. D. Al-Amri, M. El-Gomati, and M. S. Zubairy, eds.), pp. 177–199, Cham: Springer International Publishing, 2016.

[96] I. E. Gordon, L. S. Rothman, R. Hargreaves, R. Hashemi, E. Karlovets, F. Skinner, E. Conway, C. Hill, R. Kochanov, Y. Tan, et al., "The hitran2020 molecular spectroscopic database," Journal of quantitative spectroscopy and radiative transfer, p. 107949, 2021.

[97] K. C. Cossel, E. M. Waxman, I. A. Finneran, G. A. Blake, J. Ye, and N. R. Newbury, "Gas-phase broadband spectroscopy using active sources: progress, status, and applications," JOSA B, vol. 34, no. 1, pp. 104–129, 2017.

[98] S. A. Diddams, K. Vahala, and T. Udem, "Optical frequency combs: Coherently uniting the electromagnetic spectrum," Science, vol. 369, no. 6501, 2020.

[99] T. Fortier and E. Baumann, "20 years of developments in optical frequency comb technology and applications," Communications Physics, vol. 2, no. 1, pp. 1–16, 2019.

[100] N. Picqué and T. W. Hänsch, "Frequency comb spectroscopy," Nature Photonics, vol. 13, no. 3, pp. 146–157, 2019.

[101] I. Coddington, N. Newbury, and W. Swann, "Dual-comb spectroscopy," Optica, vol. 3, no. 4, pp. 414–426, 2016.

[102] S. Schiller, "Spectrometry with frequency combs," Optics letters, vol. 27, no. 9, pp. 766–768, 2002.

[103] A. Schliesser, M. Brehm, F. Keilmann, and D. W. van der Weide, "Frequency-comb infrared spectrometer for rapid, remote chemical sensing," Optics Express, vol. 13, no. 22, pp. 9029–9038, 2005.

[104] F. Keilmann, C. Gohle, and R. Holzwarth, "Time-domain mid-infrared frequency-comb spectrometer," Optics letters, vol. 29, no. 13, pp. 1542–1544, 2004.

[105] L. S. Rothman, I. E. Gordon, A. Barbe, D. C. Benner, P. F. Bernath, M. Birk, V. Boudon, L. R. Brown, A. Campargue, J.-P. Champion, et al., "The hitran 2008 molecular spectroscopic database," Journal of Quantitative Spectroscopy and Radiative Transfer, vol. 110, no. 9-10, pp. 533–572, 2009.

[106] G. B. Rieker, F. R. Giorgetta, W. C. Swann, J. Kofler, A. M. Zolot, L. C. Sinclair, E. Baumann, C. Cromer, G. Petron, C. Sweeney, et al., "Frequency-comb-based remote sensing of greenhouse gases over kilometer air paths," Optica, vol. 1, no. 5, pp. 290–298, 2014.

[107] M. Newville, T. Stensitzki, D. B. Allen, and A. Ingargiola, "LMFIT: Non-Linear Least-Square Minimization and Curve-Fitting for Python," Sept. 2014.

[108] R. V. Kochanov, I. Gordon, L. Rothman, P. Wcisło, C. Hill, and J. Wilzewski, "Hitran application programming interface (hapi): A comprehensive approach to working with spectroscopic data," Journal of Quantitative Spectroscopy and Radiative Transfer, vol. 177, pp. 15–30, 2016.

[109] R. K. Cole, A. S. Makowiecki, N. Hoghooghi, and G. B. Rieker, "Baseline-free quantitative absorption spectroscopy based on cepstral analysis," Optics express, vol. 27, no. 26, pp. 37920–37939, 2019.

[110] D. C. Benner, C. P. Rinsland, V. M. Devi, M. A. H. Smith, and D. Atkins, "A multispectrum nonlinear least squares fitting technique," Journal of Quantitative Spectroscopy and Radiative Transfer, vol. 53, no. 6, pp. 705–721, 1995.

[111] B. P. Bogert, "The quefrency alanysis of time series for echoes; cepstrum, pseudo-autocovariance, cross-cepstrum and saphe cracking," Time series analysis, pp. 209–243, 1963.

[112] A. V. Oppenheim and R. W. Schafer, "From frequency to quefrency: A history of the cepstrum," IEEE signal processing Magazine, vol. 21, no. 5, pp. 95–106, 2004.

[113] J. W. Goodman, Introduction to Fourier optics. Roberts and Company Publishers, 2005.

[114] K. Academy, "Khan academy: Intro to logarithm properties." `https://www.khanacademy.org/math/algebra2/x2ec2f6f830c9fb89:logs/x2ec2f6f830c9fb89:log-prop/a/properties-of-logarithms`, 2021.

[115] N. A. Malarich and G. B. Rieker, "Resolving nonuniform temperature distributions with single-beam absorption spectroscopy. part i: Theoretical capabilities and limitations," Journal of Quantitative Spectroscopy and Radiative Transfer, vol. 260, p. 107455, 2021.

[116] N. Malarich and G. Rieker, "Resolving nonuniform temperature distributions with single-beam absorption spectroscopy. part ii: Implementation from broadband spectra," arXiv preprint arXiv:2011.06638, 2020.

[117] P. Martín-Mateos, F. U. Khan, and O. E. Bonilla-Manrique, "Direct hyperspectral dual-comb imaging," Optica, vol. 7, no. 3, pp. 199–202, 2020.

[118] F. U. Khan, G. Guarnizo, and P. Martín-Mateos, "Direct hyperspectral dual-comb gas imaging in the mid-infrared," Optics Letters, vol. 45, no. 19, pp. 5335–5338, 2020.

[119] E. Vicentini, Z. Chen, J. H. Huh, G. Galzerano, T. W. Hänsch, and N. Picqué, "High-spectral-resolution imaging spectroscopy with a dual-comb interferometer," in Laser Science, pp. LTu2F–3, Optical Society of America, 2020.

[120] T. Voumard, T. Wildi, V. Brasch, R. G. Álvarez, G. V. Ogando, and T. Herr, "Ai-enabled real-time dual-comb molecular fingerprint imaging," Optics Letters, vol. 45, no. 24, pp. 6583–6586, 2020.

[121] L. A. Sterczewski, J. Westberg, Y. Yang, D. Burghoff, J. Reno, Q. Hu, and G. Wysocki, "Terahertz hyperspectral imaging with dual chip-scale combs," Optica, vol. 6, no. 6, pp. 766–771, 2019.

[122] T. Ideguchi, S. Holzner, B. Bernhardt, G. Guelachvili, N. Picqué, and T. W. Hänsch, "Coherent raman spectro-imaging with laser frequency combs," Nature, vol. 502, no. 7471, pp. 355–358, 2013.

[123] T. Mizuno, T. Tsuda, E. Hase, Y. Tokizane, R. Oe, H. Koresawa, H. Yamamoto, T. Minamikawa, and T. Yasui, "Optical image amplification in dual-comb microscopy," Scientific Reports, vol. 10, no. 1, pp. 1–10, 2020.

[124] M. Shirasaki, "Large angular dispersion by a virtually imaged phased array and its application to a wavelength demultiplexer," Optics letters, vol. 21, no. 5, pp. 366–368, 1996.

[125] T. Mizuno, Y. Nakajima, Y. Hata, T. Tsuda, A. Asahara, T. Kato, T. Minamikawa, T. Yasui, and K. Minoshima, "Computationally image-corrected dual-comb microscopy with a free-running single-cavity dual-comb fiber laser," Optics Express, vol. 29, no. 4, pp. 5018–5032, 2021.

[126] T. Mizuno, E. Hase, T. Minamikawa, Y. Tokizane, R. Oe, H. Koresawa, H. Yamamoto, and T. Yasui, "Full-field fluorescence lifetime dual-comb microscopy using spectral mapping and frequency multiplexing of dual-comb optical beats," Science Advances, vol. 7, no. 1, p. eabd2102, 2021.

[127] K. Shibuya, T. Minamikawa, Y. Mizutani, H. Yamamoto, K. Minoshima, T. Yasui, and T. Iwata, "Scan-less hyperspectral dual-comb single-pixel-imaging in both amplitude and phase," Optics express, vol. 25, no. 18, pp. 21947–21957, 2017.

[128] E. J. Candès, J. Romberg, and T. Tao, "Robust uncertainty principles: Exact signal reconstruction from highly incomplete frequency information," IEEE Transactions on information theory, vol. 52, no. 2, pp. 489–509, 2006.

[129] D. L. Donoho, “Compressed sensing,” IEEE Transactions on information theory, vol. 52, no. 4, pp. 1289–1306, 2006.

[130] E. J. Candes and T. Tao, “Near-optimal signal recovery from random projections: Universal encoding strategies?,” IEEE transactions on information theory, vol. 52, no. 12, pp. 5406–5425, 2006.

[131] I. Orović, V. Papić, C. Ioana, X. Li, and S. Stanković, “Compressive sensing in signal processing: algorithms and transform domain formulations,” Mathematical Problems in Engineering, vol. 2016, 2016.

[132] S. S. Chen, D. L. Donoho, and M. A. Saunders, “Atomic decomposition by basis pursuit,” SIAM review, vol. 43, no. 1, pp. 129–159, 2001.

[133] R. G. Baraniuk, V. Cevher, and M. B. Wakin, “Low-dimensional models for dimensionality reduction and signal recovery: A geometric perspective,” Proceedings of the IEEE, vol. 98, no. 6, pp. 959–971, 2010.

[134] R. Baraniuk, M. Davenport, R. DeVore, and M. Wakin, “A simple proof of the restricted isometry property for random matrices,” Constructive Approximation, vol. 28, no. 3, pp. 253–263, 2008.

[135] S. J. Wright, Primal-dual interior-point methods. SIAM, 1997.

[136] R. G. Baraniuk, “Compressive sensing [lecture notes],” IEEE signal processing magazine, vol. 24, no. 4, pp. 118–121, 2007.

[137] B. Adcock and A. C. Hansen, Compressive Imaging: Structure, Sampling, Learning. Cambridge University Press, 2021.

[138] S. Foucart and H. Rauhut, A mathematical introduction to compressive sensing. Birkhäuser, 2013.

[139] M. A. Davenport, P. T. Boufounos, M. B. Wakin, and R. G. Baraniuk, “Signal processing with compressive measurements,” IEEE Journal of Selected topics in Signal processing, vol. 4, no. 2, pp. 445–460, 2010.

[140] C. E. Shannon, “Communication in the presence of noise,” Proceedings of the IRE, vol. 37, no. 1, pp. 10–21, 1949.

[141] H. Nyquist, “Certain topics in telegraph transmission theory,” Transactions of the American Institute of Electrical Engineers, vol. 47, no. 2, pp. 617–644, 1928.

[142] M. P. Edgar, G. M. Gibson, and M. J. Padgett, “Principles and prospects for single-pixel imaging,” Nature Photonics, vol. 13, pp. 13–20, Jan. 2019. Number: 1 Publisher: Nature Publishing Group.

[143] M. F. Duarte, M. A. Davenport, D. Takhar, J. N. Laska, T. Sun, K. F. Kelly, and R. G. Baraniuk, “Single-pixel imaging via compressive sampling,” IEEE signal processing magazine, vol. 25, no. 2, pp. 83–91, 2008.

[144] G. M. Gibson, S. D. Johnson, and M. J. Padgett, “Single-pixel imaging 12 years on: a review,” Optics Express, vol. 28, no. 19, pp. 28190–28208, 2020.

[145] M.-J. Sun and J.-M. Zhang, "Single-pixel imaging and its application in three-dimensional reconstruction: a brief review," Sensors, vol. 19, no. 3, p. 732, 2019.

[146] G. K. Wallace, "The jpeg still picture compression standard," IEEE transactions on consumer electronics, vol. 38, no. 1, pp. xviii–xxxiv, 1992.

[147] W. L. Chan, K. Charan, D. Takhar, K. F. Kelly, R. G. Baraniuk, and D. M. Mittleman, "A single-pixel terahertz imaging system based on compressed sensing," Applied Physics Letters, vol. 93, no. 12, p. 121105, 2008.

[148] Y.-H. He, Y.-Y. Huang, Z.-R. Zeng, Y.-F. Li, J.-H. Tan, L.-M. Chen, L.-A. Wu, M.-F. Li, B.-G. Quan, S.-L. Wang, et al., "Single-pixel imaging with neutrons," Science Bulletin, vol. 66, no. 2, pp. 133–138, 2021.

[149] N. Radwell, K. J. Mitchell, G. M. Gibson, M. P. Edgar, R. Bowman, and M. J. Padgett, "Single-pixel infrared and visible microscope," Optica, vol. 1, pp. 285–289, Nov 2014.

[150] M.-J. Sun, M. P. Edgar, G. M. Gibson, B. Sun, N. Radwell, R. Lamb, and M. J. Padgett, "Single-pixel three-dimensional imaging with time-based depth resolution," Nature communications, vol. 7, no. 1, pp. 1–6, 2016.

[151] M. A. Davenport, M. F. Duarte, M. B. Wakin, J. N. Laska, D. Takhar, K. F. Kelly, and R. G. Baraniuk, "The smashed filter for compressive classification and target recognition," in Computational Imaging V, vol. 6498, p. 64980H, International Society for Optics and Photonics, 2007.

[152] G. Turin, "An introduction to matched filters," IRE Transactions on Information Theory, vol. 6, no. 3, pp. 311–329, 1960.

[153] R. Calderbank, S. Jafarpour, and R. Schapire, "Compressed learning: Universal sparse dimensionality reduction and learning in the measurement domain," preprint, 2009.

[154] K. Kulkarni and P. Turaga, "Reconstruction-free action inference from compressive imagers," IEEE transactions on pattern analysis and machine intelligence, vol. 38, no. 4, pp. 772–784, 2015.

[155] H. Braun, P. Turaga, and A. Spanias, "Direct tracking from compressive imagers: A proof of concept," in 2014 IEEE International Conference on Acoustics, Speech and Signal Processing (ICASSP), pp. 8139–8142, IEEE, 2014.

[156] Z. W. Wang, V. Vineet, F. Pittaluga, S. N. Sinha, O. Cossairt, and S. Bing Kang, "Privacy-preserving action recognition using coded aperture videos," in Proceedings of the IEEE/CVF Conference on Computer Vision and Pattern Recognition Workshops, pp. 0–0, 2019.

[157] D. Mascareñas, A. Cattaneo, J. Theiler, and C. Farrar, "Compressed sensing techniques for detecting damage in structures," Structural Health Monitoring, vol. 12, no. 4, pp. 325–338, 2013.

[158] J. J. Fortney, T. D. Robinson, S. Domagal-Goldman, D. S. Amundsen, M. Brogi, M. Claire, D. Crisp, E. Hebrard, H. Imanaka, R. de Kok, et al., "The need for laboratory work to aid in the understanding of exoplanetary atmospheres," arXiv preprint arXiv:1602.06305, 2016.

[159] J. J. Fortney, T. D. Robinson, S. Domagal-Goldman, A. D. Del Genio, I. E. Gordon, E. Gharib-Nezhad, N. Lewis, C. Sousa-Silva, V. Airapetian, B. Drouin, *et al.*, "The need for laboratory measurements and ab initio studies to aid understanding of exoplanetary atmospheres," *arXiv preprint arXiv:1905.07064*, 2019.

[160] C. S. Goldenstein, R. M. Spearrin, J. B. Jeffries, and R. K. Hanson, "Infrared laser-absorption sensing for combustion gases," *Progress in Energy and Combustion Science*, vol. 60, pp. 132–176, 2017.

[161] A. Lévy, N. Lacome, and C. Chackerian Jr, "Collisional line mixing in spectroscopy of the earth's atmosphere and interstellar medium, edited by kn rao, a. weber," 1992.

[162] J.-M. Hartmann, C. Boulet, and D. Robert, *Collisional effects on molecular spectra: laboratory experiments and models, consequences for applications*. Elsevier, 2021.

[163] C. Amiot, P. Ryczkowski, A. T. Friberg, J. M. Dudley, and G. Genty, "Supercontinuum spectral-domain ghost imaging," *Optics letters*, vol. 43, no. 20, pp. 5025–5028, 2018.

[164] G. Gibson, B. Sun, M. Edgar, D. Phillips, N. Hempler, G. Maker, G. Malcolm, and M. Padgett, "Real-time imaging of methane gas leaks using a single-pixel camera," *Optics Express*, vol. 25, p. 2998, Feb. 2017.

[165] A. A. Michelson, "The echelon spectroscope," *The Astrophysical Journal*, vol. 8, p. 37, 1898.

[166] F. H. Chaffee and D. J. Schroeder, "Astronomical applications of echelle spectroscopy," *Annual Review of Astronomy and Astrophysics*, vol. 14, no. 1, pp. 23–42, 1976.

[167] E. Lhospice, C. Buisset, H. R. Jones, W. E. Martin, R. Errmann, S. Sithajan, C. Boonsri, P. Choochalerm, G. Anglada-Escudé, D. Campbell, *et al.*, "Exohspec folded design optimization and performance estimation," in *Techniques and Instrumentation for Detection of Exoplanets IX*, vol. 11117, p. 111170Z, International Society for Optics and Photonics, 2019.

[168] S. S. Vogt, S. L. Allen, B. C. Bigelow, L. Bresee, W. E. Brown, T. Cantrall, A. Conrad, M. Couture, C. Delaney, H. W. Epps, *et al.*, "Hires: the high-resolution echelle spectrometer on the keck 10-m telescope," in *Instrumentation in Astronomy VIII*, vol. 2198, pp. 362–375, International Society for Optics and Photonics, 1994.

[169] J. Hearnshaw, S. Barnes, G. Kershaw, N. Frost, G. Graham, R. Ritchie, and G. Nankivell, "The hercules echelle spectrograph at mt. john," *Experimental Astronomy*, vol. 13, no. 2, pp. 59–76, 2002.

[170] L. Xu, M. A. Davenport, M. A. Turner, T. Sun, and K. F. Kelly, "Compressive echelle spectroscopy," in *Unconventional Imaging, Wavefront Sensing, and Adaptive Coded Aperture Imaging and Non-Imaging Sensor Systems*, vol. 8165, p. 81650E, International Society for Optics and Photonics, 2011.

[171] G.-W. Truong, E. M. Waxman, K. C. Cossel, E. Baumann, A. Klose, F. R. Giorgetta, W. C. Swann, N. R. Newbury, and I. Coddington, "Accurate frequency referencing for fieldable dual-comb spectroscopy," *Optics express*, vol. 24, no. 26, pp. 30495–30504, 2016.

[172] S. Coburn, C. B. Alden, R. Wright, K. Cossel, E. Baumann, G.-W. Truong, F. Giorgetta, C. Sweeney, N. R. Newbury, K. Prasad, et al., "Regional trace-gas source attribution using a field-deployed dual frequency comb spectrometer," Optica, vol. 5, no. 4, pp. 320–327, 2018.

[173] P. J. Schroeder, R. J. Wright, S. Coburn, B. Sodergren, K. C. Cossel, S. Droste, G. W. Truong, E. Baumann, F. R. Giorgetta, I. Coddington, et al., "Dual frequency comb laser absorption spectroscopy in a 16 mw gas turbine exhaust," Proceedings of the Combustion Institute, vol. 36, no. 3, pp. 4565–4573, 2017.

[174] L. C. Sinclair, J.-D. Deschênes, L. Sonderhouse, W. C. Swann, I. H. Khader, E. Baumann, N. R. Newbury, and I. Coddington, "Invited article: A compact optically coherent fiber frequency comb," Review of scientific instruments, vol. 86, no. 8, p. 081301, 2015.

[175] C. Gu, D. Zhang, Y. Chang, and S.-C. Chen, "Digital micromirror device-based ultrafast pulse shaping for femtosecond laser," Optics letters, vol. 40, no. 12, pp. 2870–2873, 2015.

[176] L. McMackin, M. A. Herman, and T. Weston, "Design of a multi-spectral imager built using the compressive sensing single-pixel camera architecture," in Emerging Digital Micromirror Device Based Systems and Applications VIII, vol. 9761, p. 97610G, International Society for Optics and Photonics, 2016.

[177] O. Martinez, "Design of high-power ultrashort pulse amplifiers by expansion and recompression," IEEE Journal of Quantum Electronics, vol. 23, no. 8, pp. 1385–1387, 1987.

[178] O. Martinez, "3000 times grating compressor with positive group velocity dispersion: Application to fiber compensation in 1.3-1.6 μm region," IEEE Journal of Quantum Electronics, vol. 23, no. 1, pp. 59–64, 1987.

[179] Q. D. Pham and Y. Hayasaki, "Optical frequency comb profilometry using a single-pixel camera composed of digital micromirror devices," Applied optics, vol. 54, no. 1, pp. A39–A44, 2015.

[180] Z. Wang, A. C. Bovik, H. R. Sheikh, and E. P. Simoncelli, "Image quality assessment: from error visibility to structural similarity," IEEE transactions on image processing, vol. 13, no. 4, pp. 600–612, 2004.

[181] S. Coburn, C. B. Alden, R. Wright, K. Cossel, E. Baumann, G.-W. Truong, F. Giorgetta, C. Sweeney, N. R. Newbury, K. Prasad, I. Coddington, and G. B. Rieker, "Regional trace-gas source attribution using a field-deployed dual frequency comb spectrometer," Optica, vol. 5, pp. 320–327, Apr 2018.

[182] C. R. Shaddix, "Correcting thermocouple measurements for radiation loss: a critical review," 1999.

[183] M. Heitor and A. Moreira, "Thermocouples and sample probes for combustion studies," Progress in energy and combustion science, vol. 19, no. 3, pp. 259–278, 1993.

[184] P. A. Skovorodko, A. G. Tereshchenko, D. A. Knyazkov, A. A. Paletsky, and O. P. Korobeinichev, "Experimental and numerical study of thermocouple-induced perturbations of the methane flame structure," Combustion and flame, vol. 159, no. 3, pp. 1009–1015, 2012.

[185] N. Bahlawane, U. Struckmeier, T. S. Kasper, and P. Oßwald, "Noncatalytic thermocouple coatings produced with chemical vapor deposition for flame temperature measurements," Review of scientific instruments, vol. 78, no. 1, p. 013905, 2007.

[186] A. Hayhurst and D. B. Kittelson, "Heat and mass transfer considerations in the use of electrically heated thermocouples of iridium versus an iridiumrhodium alloy in atmospheric pressure flames," Combustion and Flame, vol. 28, pp. 301–317, 1977.

[187] G. B. Rieker, J. B. Jeffries, and R. K. Hanson, "Calibration-free wavelength-modulation spectroscopy for measurements of gas temperature and concentration in harsh environments," Applied optics, vol. 48, no. 29, pp. 5546–5560, 2009.

[188] B. Gebhart, "Natural convection flows and stability," in Advances in Heat Transfer, vol. 9, pp. 273–348, Elsevier, 1973.

[189] O. Martynenko, A. Berezovsky, and Y. A. Sokovishin, "Laminar free convection from a vertical plate," International Journal of Heat and Mass Transfer, vol. 27, no. 6, pp. 869–881, 1984.

[190] C. S. Callahan, "Gaas." `https://github.com/CharlieCallahan/GPU_Accelerated_Absorption_Sim`, 2021.

[191] O. Willstrand, "Intensity distribution conversion from gaussian to top-hat in a single-mode fiber connector," Lund Reports on Atomic Physics, 2013.

[192] D. Dudley, W. M. Duncan, and J. Slaughter, "Emerging digital micromirror device (dmd) applications," in MOEMS display and imaging systems, vol. 4985, pp. 14–25, International Society for Optics and Photonics, 2003.

[193] D. Vettese, "Liquid crystal on silicon," Nature Photonics, vol. 4, no. 11, pp. 752–754, 2010.

[194] Z. Zhang, Z. You, and D. Chu, "Fundamentals of phase-only liquid crystal on silicon (lcos) devices," Light: Science & Applications, vol. 3, no. 10, pp. e213–e213, 2014.

[195] J. B. Sampsell, "Digital micromirror device and its application to projection displays," Journal of Vacuum Science & Technology B: Microelectronics and Nanometer Structures Processing, Measurement, and Phenomena, vol. 12, no. 6, pp. 3242–3246, 1994.

[196] M. A. Cox, "Structuring light with digital micro-mirror devices," in Complex Light and Optical Forces XV (E. J. Galvez, H. Rubinsztein-Dunlop, and D. L. Andrews, eds.), vol. 11701, pp. 1 – 8, International Society for Optics and Photonics, SPIE, 2021.

[197] S. Turtaev, I. T. Leite, K. J. Mitchell, M. J. Padgett, D. B. Phillips, and T. Čižmár, "Comparison of nematic liquid-crystal and dmd based spatial light modulation in complex photonics," Optics express, vol. 25, no. 24, pp. 29874–29884, 2017.

[198] M. Cafaro, "Stage-vss/matlab-lcr." `https://github.com/Stage-VSS/matlab-lcr`, 2017.

[199] DLPU010G, DLPC350 Programmer's Guide, 2018.

[200] DLPU011F, TI DLP LightCrafter 4500 Evaluation Module User's Guide, 2016.

[201] P. K. Kundu, I. M. Cohen, and D. R. Dowling, Fluid Mechanics, 5th edition. Academic Press, 2011.

[202] N. A. Riza and M. J. Mughal, “Optical power independent optical beam profiler,” Optical Engineering, vol. 43, pp. 793–797, Apr. 2004. Publisher: International Society for Optics and Photonics.

Appendix A

Spatial Light Modulators

Spatial light modulators (SLMs) are the technologies which enable measurements with sub-beam resolution. These devices modulate the intensity, phase, or polarization of an incident beam of light, and behave as programmable transmission masks. SLMs were first developed in the 1970s, and since then, have matured as technologies largely due to their applications in the projection display market [192, 193]. In this thesis, we use two classes of SLMs, liquid crystal on silica SLMs (LCOS-SLMs), and digital micromirror devices (DMDs). LCOS-SLMs operate by modulating the refractive index at each pixel by electrically rotating birefringent liquid crystals [194]. These devices can be used to change the phase or polarization of the light at each pixel [113]. Used in conjunction with a polarizer placed after the SLM, these devices can be used to modulate the intensity of the light at each pixel [194, 113]. In contrast, the mirrors of DMDs offer only binary amplitude modulation, since each mirror can be actuated to be in one of two states, "on" or "off" [195]. DMDs are favored over LCOS-SLMs in applications which require polarization independent beam modulation or broad spectrum invariance, qualities they inherit from their aluminum mirrors [196], as well as in applications which require full attenuation like the spectroscopy project we present in Chapter 4. These features may also confer an efficiency advantage of DMDs over SLMs [197]. Additionally, DMDs can have faster modulation (refresh) rates than other SLMs [197].

Appendix B

Digital Micromirror Device

The digital micromirror device (DMD, TI DLP4500) that we use in this thesis has an array of 1140x912 square mirrors (side length $L = 7.637\ \mu$m) that are individually controllable and can be programmed to point in one of two directions, $+12°$ or $-12°$. When the DMD is not powered or in power save mode, each mirror is "parked" at approximately $0°$. The DMD interfaces with a computer via a USB cable and is recognized as an HID device.

The DMD was extracted from an evaluation module (EVM, DLPLCR4500EVM) designed for developers to test the capabilities of the chip as a projector. This evaluation module integrates the DMD, the digital controller for the DMD (TI DLPC350), an LED-based projector system called the "light engine", and the circuitry to support the system. With the graphical user interface (GUI) provided by TI, the EVM can be configured to project a series of 912x1140 pixel 8-bit grayscale images at rates up to 120 Hz, or 912x1140 pixel binary images at images up to 4225 Hz. For our work, we wished to use the DMD to display binary images, but we needed to isolate the chip from the light engine and mount it within our experiments. While we could have purchased just the DMD and the digital controller, the circuitry which we would have had to develop to connect the two chipsets to each other and to a computer would have required extensive development, so we opted to purchase the EVM and then to extract the DMD from within the light engine.

B.1 Extracting the digital micromirror device from the evaluation module

The DMD is located within the optical engine under the printed circuit board (PCB) of the EVM. To remove the DMD, first unplug all the LED driver cables and the fan driver cable, and gently separate the orange flex cable from the PBC. Unscrew the screws securing the PCB to the vertical support rods. The only components from the bottom board that we need to keep are the DMD and the flex cable which attaches it to the PCB, the small, finned heat sink on the back of the DMD, and the plastic casing to which the DMD and heat sink are mounted. This frame will be used to secure the DMD in our experiments.

To access the DMD, the L-shaped plate on the top of the light engine needs to be removed. Unfortunately, every possible opening to the optical engine is sealed with a black glue which is hard to remove. I used an exacto knife and a dremmel to grind this glue off. Once the glue is removed, unscrew the tiny screws which fasten the top to the sides and pry off the top of the light engine. This was physically demanding. Take care to orient the board to protect the DMD secured inside from any falling debris.

Once the lid of the light engine is off, leave the DMD, heat sink, and flex cable assembly intact and use a saw to cut the frame which supports it out from the light engine.

B.2 Mounting the digital micromirror device in experiments

To mount the DMD in experiments, I laser cut an acrylic piece with holes to secure it to a standard optical mount and with slats to which the heat fins on the rear of the DMD could be press fit. The optical mount supports the DMD above the PCB. The mounted DMD is shown in Fig. B.1.

B.3 Controlling the digital micromirror device

TI provides a GUI which is a C++ wrapper around the I2C and USB interfaces. While this GUI can be used to control the DMD, we found this to be quite inefficient, so we developed a

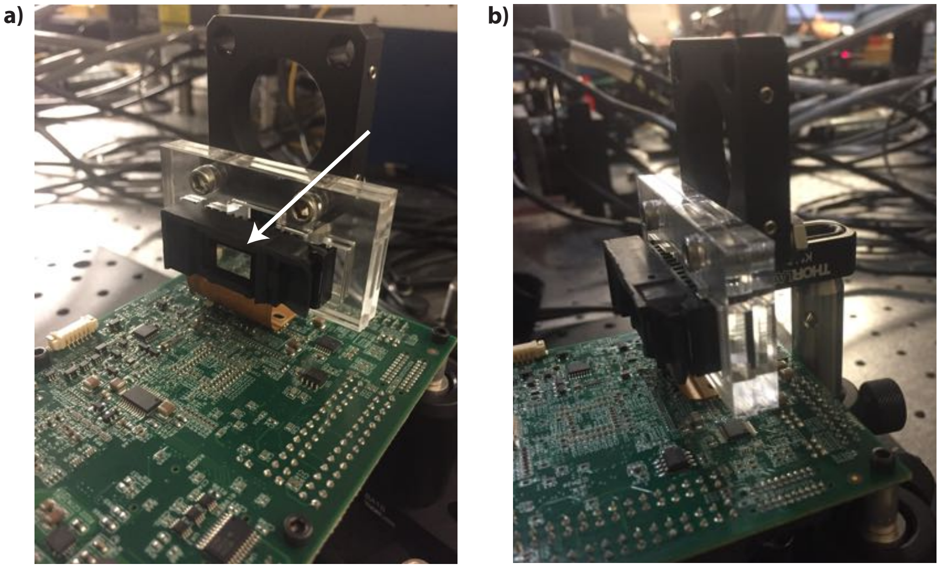

Figure B.1: Digital micromirror device (DMD), isolated from the light engine and mounted in experiments. a) the arrow indicates the DMD chip. b) the side view shows how the heat sink fins located on the rear of the DMD are pressed into the acrylic mount (clear) which is screwed to a standard optical mount. This mount supports the DMD above its associated circuitry without stressing the orange flex cable.

control strategy based on a GitHub repository called Stage-VSS/matlab-lcr [198] which uses the source code for the GUI. This source code can be unzipped from a folder embedded within the GUI download files, and much of its functionality is detailed in Re. [199]. The GUI source code is written in C++ and has two relevant files, LCR4500_api.cpp and LCR4500_api.h, which contain the code and a list of most of the source code functions, respectively.

Our MATLAB library consists of MATLAB executable (.mex) files which call the GUI source code using C++ syntax but which behave like MATLAB functions. Each function from the GUI source code has its own .mex file. Any function called from the .cpp file must be listed in the .h file. If a function is added to the .h file, remake the C++ library following the directions in matlab-lcr-master/api/make.txt. This must be done using Microsoft Visual Studio and hidapi.cpp. To add .mex files to the library, compile them with the make.m file by (type make.m into the MATLAB command line).

This code is available upon reasonable request.

B.3.1 Control sequence

In MATLAB, create an instance of the LightCrafter4500 object and open it using lcrOpen(). Turn the DMD on using lcrSetPowerMode(0). Set the mode to pattern mode, and tell the controller to get images stored within the flash memory using lcrSetPatternDisplayMode(false) and lcrPatternDisplay(0), respectively. Before programming the controller, stop the pattern display with lcrPatternDisplay(0). Next, set the trigger mode with lcrSetPatternTriggerMode(1), and set the pattern configuration according to (lcrSetPatternConfig(number_of_patterns, 1, number_of_patterns, number_of_images), where number_of_patterns is the number of LUT entries to be sent to the controller and is the number of patterns within the sequence, even if some are displayed multiple times as in the pattern A-B-A-C-A-D, for which number_of_patterns=6. Next, set the exposure and frame periods with lcrSetExposureFramePeriod(exposure_period, frame_period). We set these to be the same value. These are in units of microseconds. These times are limited by the bit depth of the images and the speed of the DMD as shown in Table 4-1 in the EVM user's guide [200].

Before writing to the pattern and exposure LUTs, we clear them using the commands lcrClearPatLut() and lcrClearExpLut(). Now we can add patterns to the pattern LUT. To do this, call lcrAddToPatLut. This takes the following arguments: the trigger type, the pattern number, the bit depth, the LED color, a boolean which if true inverts the pattern, a boolean which if true inserts a black frame after each pattern, an argument which tells the controller to perform a buffer swap, and an argument which controls Trigger Out 1. These arguments are described in the dlpc350_api.cpp source code provided by TI. To run the patterns smoothly, ensure that the buffer swap argument is true for the first pattern and false for the remaining patterns. Once the LUT has an entry for each pattern, send the pattern LUT to the DLPC350 controller by calling lcrSendPatLut().

Create the image LUT calling a .mex files titled lcrSendImageLut_Ximages(), where X corresponds to the number of images to be called from the flash. This command also sends the image LUT to the DLPC350 controller. Ensure this was completed successfully by calling lcrValidatePatLutData().

Once the pattern LUT and the image LUT have been sent to the controller, we can start displaying patterns on the DMD by calling lcrPatternDisplay().

B.4 Generating patterns for display on the micromirror device

The DMD controller stores up to 64 images saved as 24 bit .bmp files in its flash. When the DMD is being used as a projector with 3 LEDs, each byte informs one of the LEDs (note that the controller reads bits 0-7, 8-15, and 16-23 as green, red, and blue, respectively. This is in contrast to the standard red, green, blue convention). However, in our applications, we only need one bit plane of information per frame. Therefore, each of the 24 bit planes of a .bmp image can be used to encode a pattern. Care must be taken to store images according to the green, red, blue convention.

The script generate_images_main.m creates such .bmp images. For each group of 8 bit planes (one byte), this script creates an 8-bit 1140x912 matrix where each entry is a binary number corresponding to the planes in which the mirror points in the nonzero direction. Specifically, for each bit plane, the script makes a matrix of zeros with values of $2^{(i-1)}$ for the pixels within the pattern, where i is the plane counter and ranges from 1 to 8. 8 of these matrices with nonzero components corresponding to $2^0,\ 2^1, ..., 2^7$ are added to each other and stored as a uint8 object. Three of these uint8 objects are written to a .bmp file using MATLAB's imwrite function.

Note that patterns are distorted when they are displayed on the DMD. The short and long sides of the DMD correspond to the 1140 and 912 pixel matrix directions in the MATLAB code. To account for this distortion, images can be generated with an apparent scaling factor of 1/2 in the 1140 direction.

B.5 Writing firmware for the digital micromirror device

Images are downloaded to the flash of the DLPC350 via a binary firmware file. This firmware file can be generated using the GUI, or using an executable generated from a C++ script which calls the GUI's source code. This script was adapted from code from the GUI by Jonathan Meade. This script is available upon reasonable request.

Appendix C

Considerations for measuring angular velocity and vorticity

Particles orbiting a point move according to two modes: solid body rotation flow and free vortex flow. In the former case, the orientation of the particle (the direction the particle points) remains fixed about the center of rotation throughout the trajectory of the particle. In the latter case, the orientation of the particle remains unchanged relative to a stationary point as the particle moves. In these cases, the steady state angular velocities of the particle about the axis of rotation can be expressed as $\vec{\Omega} = [0, 0, \Omega]^T$ and $\vec{\Omega} = [0, 0, \alpha r^{-2}]^T$, respectively, where Ω is the angular velocity, α is a constant, and r is the orbit radius. The vorticity is calculated as the curl of the velocity, $\vec{\omega} = \vec{\nabla} \times \vec{U}$, where the velocity is given by $\vec{U} = \vec{\Omega} \times \vec{r}$ given the particle position $\vec{r}$. Consequently, whereas the vorticity of the solid body rotation mode is $\vec{\omega} = 2\vec{\Omega}$, the vorticity of the free vortex mode is identically $\vec{\omega} = \vec{0}$.

The sensor we present in Chap. 2 correlates the scattered-light burst generated from the pathline of a scattering particle traveling through the probe beam. If this pathline is curved, the sensor cannot distinguish if the curvature is due to solid body rotation or free vortex flow.

Just as curved pathlines do not necessarily imply nonzero vorticity, nonzero vorticity does not necessarily imply that the pathlines are necessarily curved. For example, shear flows like one with a velocity profile given by $\vec{U} = [\beta x_2, 0, 0]$ where the velocity in the $\hat{x}_1$ direction depends linearly on the $\hat{x}_2$ position scaled with a constant β have straight pathlines in the $\hat{x}_1$ direction but nonzero vorticity: $\vec{\omega} = [0, 0, -\beta]$.

In fluid mechanics, vorticity is commonly interpreted as twice the local angular velocity [201].

We caution the reader that, in general, the angular velocities measured by the sensor we present here **cannot** be interpreted as local angular velocities from which vorticity fields can be deduced but are rather the angular velocities of the tracer particles about their orbit centers. Therefore, these measurements of angular velocity should not be used to calculate vorticity. However, we note that there does exist a special case in which vorticity **can** be deduced from these measurements: when the system is known to be rotating exclusively according to the solid body rotation mode (as in the experiments of Ref. [1]).

Appendix D

Locating beams on the spatial light modulators

When using a spatial light modulator to modify the phase or amplitude of a beam, it is important to ensure that the positioning of the mask agrees with the positioning of the beam. While this can be accomplished by analyzing the diffracted orders (*e.g.* maximizing the power in the diffracted order of choice or imaging it and tuning the alignment to optimize the symmetry of the beam), we found that first locating the beam centroid on the device then generating the mask to be displayed on the device according to the centroid positioning was more fruitful. Our approach follows those detailed in Refs. [86, 87, 88, 202].

To locate the center of the beam on the DMD using a simulated knife edge test, we segmented DMD pixels into 48 segments spaced evenly along the direction of the knife edge, spanning the entire DMD in the direction orthogonal to the knife edge. We programmed the DMD to characterize the incident beam. Initially, the mirrors in every segment pointed away from the detector, corresponding to the condition in the knife edge test when the knife occludes the entire beam. Then, to simulate translating the knife edge through the beam, we programmed the DMD to turn the mirrors from the segments towards the detector, stepping subsequent sections in for every measurement. We averaged the photodetector signal according to each frame for approximately 1 second to reduce the effect of the noise.

The measured signals were normalized by the final measurement corresponding to the intensity of the beam sampled at every pixel on the DMD. This normalized signal was fitted to an error function according to

$$y = \frac{1}{2}\left[1 + erf\left(\sqrt{2}\,\frac{x - x_0}{w_0}\right)\right], \tag{D.1}$$

where x is the coordinate across which the simulated knife edge traverses, x_0 is the location of the interface of the mirrors pointing towards and away from the detector, and w_0 is the beam waist. w_0 was left as a free parameter. We calculated the coordinate of the centroid of the beam by setting the fitted equation to 1/2.

To locate the center of the beam on the LCOS-SLM using a simulated knife edge test, we followed the same procedure as above, but we programmed the pixels of the LCOS-SLM meant to sample the beam with a diffraction grating to send the sampled light towards a photodetector.

Appendix E

Experimentally determining the size of Laguerre Gauss beams using a radial knife edge test

To match our simulations to our experiments for our work in Ch. 2, we had to determine the size of the beam of light light incident on the DMD. This was accomplished in two steps. First, we projected a grating on the LCOS-SLM which had the same period as those used to create the petal beams, but this grating simply diffracted the Gaussian beam in the direction of the DMD. We used the DMD to perform a knife edge test in two orthogonal directions following Ref. [202]. From the results of these two simulated knife edge tests, we located the position of the centroid of the beam in both directions in the coordinate system of the DMD. While this knife edge test could have also revealed the beam waist of the Gaussian beam, we wanted to confirm that this was also the beam waist of the petal shaped beams.

The radius of the maximum ring of intensity of LG beams scales as [65]

$$w_{\mathrm{I}} \propto w_0\sqrt{|l|/2}, \tag{E.1}$$

where w_0 is the beam waist. Therefore, by measuring the intensity as a function of the azimuthal mode number $\pm l$, we can determine w_0. Because it would be technically challenging to determine only w_{I}, for each beam with a different value of $\pm l$, we program the DMD to sample multiple concentric circles of radius r.

To measure the beam waists of the petal shaped beams, we sampled beams incident on the DMD radially by directing only the light incident on mirrors within a circle radius r located at the center of the beam as determined with the knife edge test to the photodetector. We studied 7 beams with $\pm l = \{0, 1, 2, 3, 4, 5, 6\}$. The diffraction efficiency of our gratings decreases with increasing $\pm l$ as $(|l| + 1)^{-1/2}$ since the overlap between the grating and the incident Gaussian beam diminishes as $|l|$ grows large [65]. Therefore, we normalized the intensity for each beam by that with the intensity of the same beam measured using a circle with $r = 300$ pixels. Simulations of this experiment are illustrated in Fig. E.1.

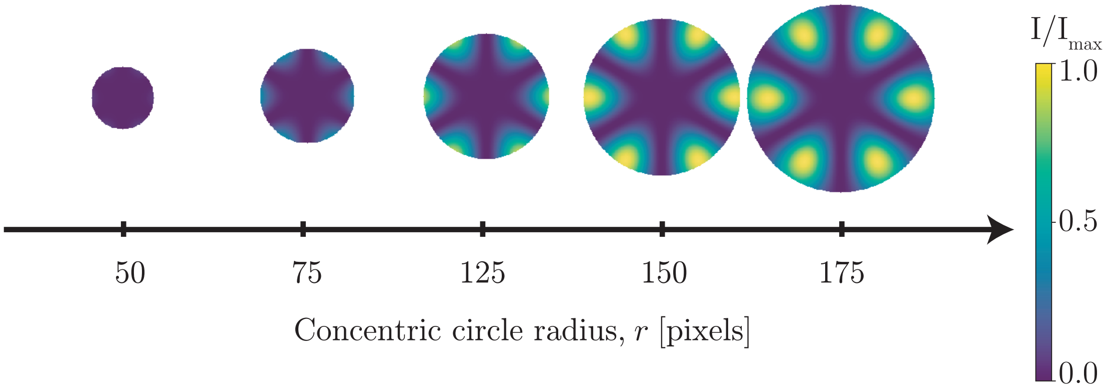

Figure E.1: Illustration of the simulated radial knife edge test indicating the portions of the beam that are sampled as a function of concentric circle radius r. A Laguerre Gauss beam with $l = \pm 3$ is sampled as a function of radius r. The intensity of each sample uses the color scaling according to the color bar at right.

Designing the hologram displayed on the LCOS-SLM to leave w_0 unchanged in the diffracted beam, we determined w_0 by simultaneously comparing the results of all experiments to equivalent simulations in which we sampled the intensities of simulated beams within concentric circles of varying radii. We optimized the beam waist of the simulated beams while fixing $\pm l$ corresponding to the experimental conditions to best match those of the experimental beams. We found that $w_0 = 93.84$ pixels. Our results, superimposed with the corresponding simulated results, are shown in Fig. E.2.

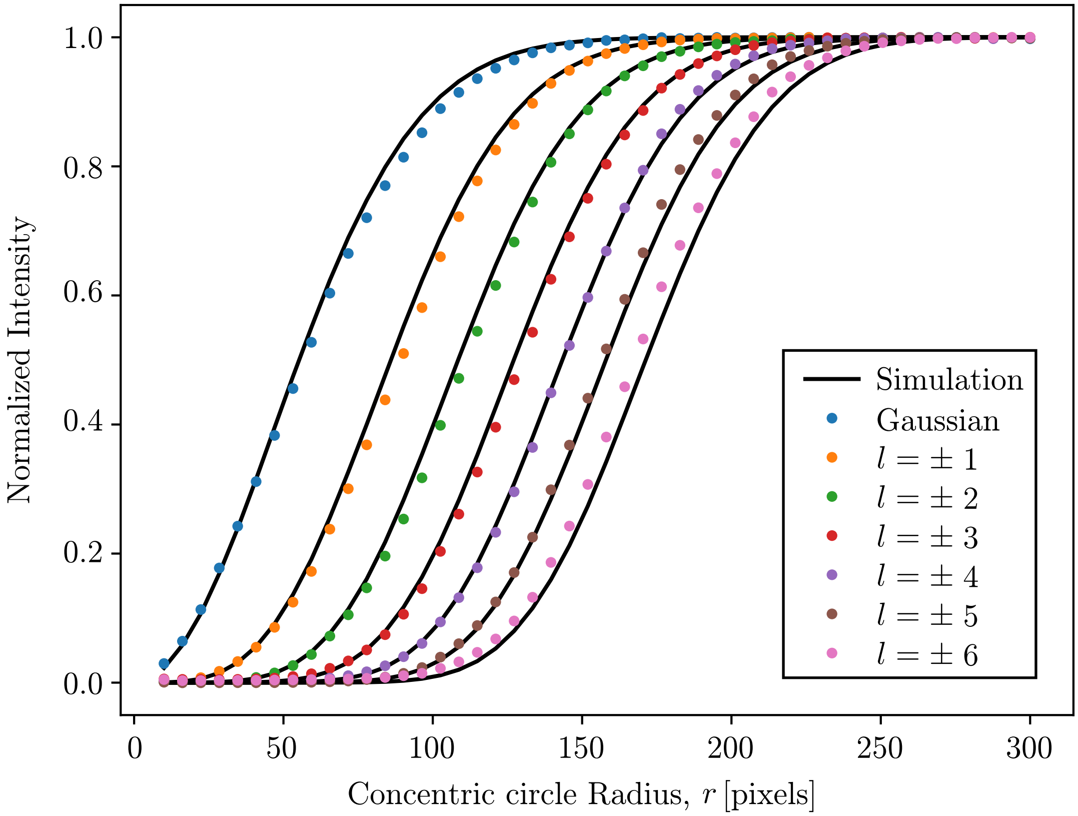

Figure E.2: Results from radial knife edge test shown in points. These were simultaneously fit according to the scaling in Eq. E.1 to find the simulated beam waist that best matches that of the experiments in order to select a beam waist for the simulations.

In experiments, we observed that some misalignment between our light and the center of the concentric circles existed: Watching the image of the light reflected from the DMD, we could see that the circle was slightly offset from the beam. Such a misalignment could have resulted from the initial simulated knife edge test which identifies the centroid of the beam. For example, the centroid of the beam may have differed slightly from the geometric center of the beam. To study the sensitivity of our beam waist measurements to a translational offset between the center of the concentric circles as measured on the DMD, we simulated the effect of such misalignments as a function of concentric circle radius. This is illustrated in Fig. E.3, where we show the portions of the beam summed as a function of δx given $r = 100$.

The results from this sensitivity analysis are shown in Fig. E.4. We found that small per-

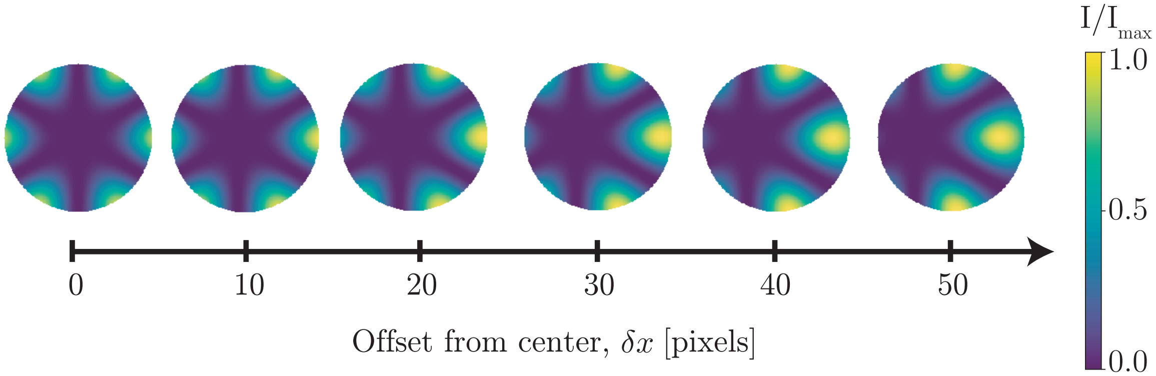

Figure E.3: To evaluate the sensitivity of the radial knife edge test to the relative offset between the beam and the sampling circle, δx, we vary this position while fixing r. Here, $r = 100$. The intensity of each sample uses the color scaling according to the color bar at right.

turbations in the centers of the concentric circles relative to the center of the beam, δx, has small effects in the summed intensity of the beam, particularly when the perturbation is small. Consequently, even if the concentric circles are slightly misaligned relative to the beam, the beam size can be well approximated using this radial knife edge approach.

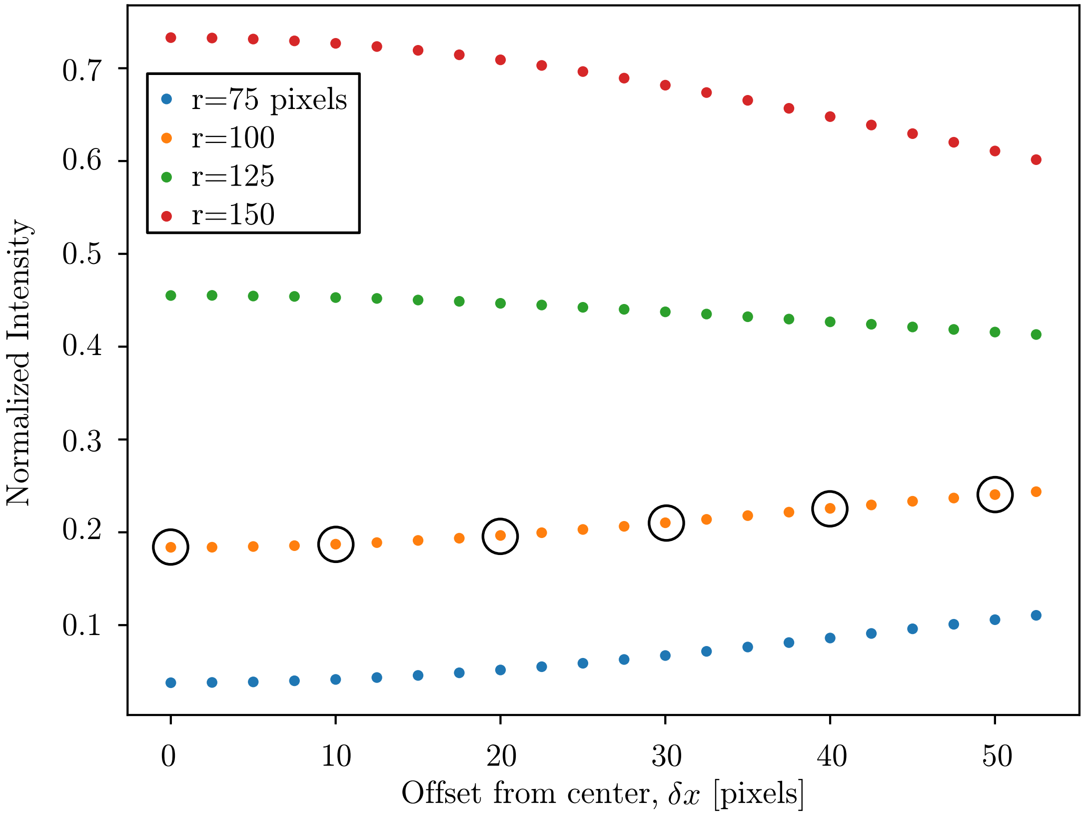

Figure E.4: Sensitivity analysis of radial knife edge test to beam positioning. The intensity within circles of varying r (see legend) are normalized by the intensity of the beam summed over the entire simulated domain, size 986x616 pixels. Circled orange points correspond to simulations illustrated in Fig. E.3.